LBL--26303

DE89 006832

An Experimental Investigation of Double Beta Decay of ^{100}Mo

Brian L. Dougherty

Ph.D. Thesis

November 1988

Physics Division
Lawrence Berkeley Laboratory
1 Cyclotron Road
Berkeley, California 94720

This work was supported by the Director, Office of Energy Research, Office of High Energy and Nuclear Physics, Division of High Energy Physics of the U. S. Department of Energy under contract #DE-AC03-76SF00098.

An Experimental Investigation of Double Beta Decay of ^{100}Mo

Brian L. Dougherty

17 November 1988

Abstract

New limits on half-lives for several double beta decay modes of ^{100}Mo were obtained with a novel experimental system which included thin source films interleaved with a coaxial array of windowless silicon detectors. Segmentation and timing information allowed backgrounds originating in the films to be studied in some detail. Dummy films containing ^{96}Mo were used to assess remaining backgrounds. With 0.1 mole years of ^{100}Mo data collected, the lower half-life limits at 90% confidence were 2.7×10^{18} years for decay via the two-neutrino mode, 5.2×10^{19} years for decay with the emission of a Majoron, and 1.6×10^{20} years and 2.2×10^{21} years for neutrinoless $0^+ \rightarrow 2^+$ and $0^+ \rightarrow 0^+$ transitions, respectively.

Contents

Acknowledgements

I thank the Physics Department of the University of California for suffering me this opportunity to pursue a Ph.D. degree. I especially thank Dr. Richard Muller, without whose guidance I might have abandoned physics.

As in all modern particle physics endeavors, this experiment was conceived, designed, built and operated collaboratively. Among the people whose efforts were most influential I must mention Margaret Alston-Garnjost, Bob Kenney, Joe Krivicich, Howard Nicholson and Bob Tripp. It was my privilege to work with this diverse group since very near the inception of the project over six years ago, and the perspective I've gained has been invaluable. The experiment justly reflects their considerable investments of time and labor, and their unique contributions of imagination, experience and skills.

I would like to thank the technicians, craftsmen and tradesmen, who rarely get the recognition they deserve, but who actually build much of the equipment and/or contribute to its smooth operation. In particular, Mike Long not only helped insure the feasibility of my designs, but machined and constructed the apparatus with great skill. Heinrich Sommer's success at detector fabrication and rehabilitation bordered on the magical. Chilton Gregory made all the source films, a fastidious labor full of tedium. Vernon Benz and Jim van Kuiken conscientiously attended bumbling physicists underground.

This experiment benefited from the patience and support of many others. Al Smith made available not only his vast knowledge of radioactivity, but also space in his low-background enclosure at LBL. Jack Walton let me break his glassware while learning how not to make high-purity detectors. The management of Consolidated Silver Inc. not only let us invade their mine but provided first-class working conditions.

Above all, the ongoing debt of gratitude I owe Julie, my wife, for her endurance is

without estimate.

This work was performed under the auspices of the U.S. Department of Energy (Contracts DE-AC03-76SF00098, DE-AC02-78ER04831 and DE-AS04-76ER03347).

Chapter 1

Introduction

Due to pairing forces acting between like nucleons, the binding energies of even-even nuclei are increased relative to those of their odd-odd isobars.[1] Consequently, in many instances ordinary beta decay is energetically forbidden or highly suppressed. If nuclear ground-state mass-energies are sufficiently different, double beta decay may then be observed. In the two-neutrino mode, $(A, Z) \rightarrow (A, Z+2) + 2e^- + 2\bar{\nu}_e$ a nucleus with A nucleons and Z protons decays to another with two additional protons and with the emission of two electrons and two antineutrinos.[2]

Particle physicists became interested in this process when it was realized that, due to its neutrality and apparent lack of magnetic moment, the electron neutrino could be its own antiparticle. A virtual neutrino emission and reabsorption may then occur and the decay, $(A, Z) \rightarrow (A, Z+2) + 2e^-$ with no neutrinos in the final state would result, violating lepton number conservation. With fewer particles in the final state, this decay would be heavily phase-space favored over the otherwise expected two-neutrino mode.[3,4] (The virtual character of the intermediate neutrino distinguishes this process from that sought in the Davis experiment of 1955, and results in an enhanced sensitivity to lepton number violation.[5])

Theoretical interest gradually fell following the discovery of maximal (or nearly maximal) parity violation in low-energy weak interactions.[6,7] Since emitted antineutrinos are right-handed, reabsorption as neutrinos is forbidden without also reversing helicity. In the absence of right-handed currents, such reversals can occur only if neutrinos are massive, and no strong argument existed for nonzero neutrino masses. Therefore, regard-

less of whether neutrinos are Majorana (particle = antiparticle[8]) or Dirac (particle $\neq$ antiparticle) in character, the amplitude for neutrinoless double beta decay was thought to vanish.

Perceptions changed again with the advent of Grand Unified Theories (GUTs). In these theories quarks and leptons of each generation are placed in common multiplets and the electro-weak and strong forces are joined into a larger group of interactions, including ones which take quarks to leptons and vice-versa. Therefore, baryon number and lepton number conservation are presumed to be violated at some level. Along with the other fundamental fermions, neutrinos are expected to be massive; but in their particular case, these are likely to be Majorana masses. Furthermore, many particular GUTs involve the explicit restoration of parity symmetry at higher energies; so low-energy right-handed weak current effects cannot be ruled out.

More recently, and independently of Grand Unification, many other lepton number violating mechanisms have been suggested which would allow neutrinoless double beta decay to occur. Such new physics beyond the minimal Standard Model posits the existence of exotic Higgs scalars, supersymmetric partners of quarks or gauge bosons and/or lepton number violating point interactions. In addition, the unique sensitivity of this decay to other physics issues has been elaborated. Experimental lifetime limits constrain the existence of heavy or right-handed partners of neutrinos, on mixing among neutrino generations and on their CP properties. Restrictions are also obtained on the existence of a novel Goldstone boson, the Majoron, indicative of certain models of how neutrinos acquire mass.

Furthermore, the scales of particle physics parameters probed in the phenomenon of neutrinoless double beta decay have been found to be of large interest in many active research programs. Neutrino masses of order 1 eV are accessible. If such were measured, there would occur obvious astrophysical/cosmological ramifications; especially with regard to the physics of galaxy formation and the closure of our universe. Tritium beta decay experiments would be expected to record a departure from linearity at the Kurie plot end-point. From many GUTs the "see saw" mechanism for neutrino mass generation, which posits the existence of right-handed neutral leptons of mass $M \approx m_{light}^2/m_\nu$ (where m_{light} is on the order of a corresponding charged lepton or quark mass) would foretell of new physics at accelerator energies of the near future.[9]

As evidenced by the many mechanisms which may engender neutrinoless double beta decay and the possible consequences for the neutrino sector, the interpretation of experimental results is complex. This situation is further complicated by the difficulty of making accurate nuclear matrix element calculations. A number of such calculations have been attempted by various groups employing different techniques, approximations and models and the results vary by as much as an order of magnitude. As a consequence, it has become observationally important not only to search for neutrinoless decay, but also to seek the expected, Standard Model allowed decay via the two-neutrino mode; which observation would provide a benchmark by which to judge the accuracy of the calculations.

There is at present no confirmed empirical evidence for any proposed augmentation of the Standard Model. Efforts to detect new-physics effects include experiments on neutrino oscillation, lepton-number violating π and K decays, polarized emissions in nuclear decay, proton decay, etc.. These experiments span a broad range of particle-physics endeavors: work at accelerators and underground, investigation of phenomena as disparate as supernovae and muon precession, and at extremes in energy.

That the possible Majorana character of neutrinos has not been seen in other elementary particle processes is due, again, to parity violation in the weak interactions; experimentally available neutrinos are always left-handed, while antineutrinos are always right-handed. Differences in interactions do not therefore distinguish between CP characteristics and helicity. Furthermore, many properties, such as the size of a Dirac neutrino's magnetic moment, vary linearly with mass. It is clear that neutrino masses are very small compared with typical energies encountered at accelerators. As the limit $\frac{m_\nu}{E_\nu} \to 0$ is approached, it becomes increasingly difficult to reverse neutrino helicity, and when $m_\nu = 0$ the distinction between Majorana and Dirac character disappears (unless there are right-handed currents) since then helicity flipping becomes impossible.

An advantage neutrinoless double beta decay has over these processes is that the energy of the exchanged neutrino is much smaller, on the order of 10 MeV. Furthermore, differences in the energy and angular distributions of the final state electrons could be used to discriminate among the operative decay mechanisms. If backgrounds are sufficiently suppressed, double beta decay becomes a most sensitive probe of new physics and is the only known feasible way of trying to determine whether neutrinos are their

own antiparticles.

Despite a nearly continuous forty year history of experimental effort, however, and notwithstanding the existence of 35 candidate isotopes to investigate, the empirical evidence for double beta decay is very limited. Most of the proof that it does occur comes from geochronological measurements on only three isotopes; ^{128}Te, ^{130}Te and ^{82}Se. In these experiments one determines the excess of daughter decay products that have accumulated over geologic time in an ore sample rich in the parent. (That noble gas daughters are involved is no accident. See references [10,11] for details.) Such experiments, however, cannot distinguish between decay modes. What is more, the measurements conflict; two of the most modern values for the lifetimes of each of the tellurium isotopes disagree with respect to their uncertainties.

One of the most frequently exploited direct counting techniques involves the use of sources which form a part of the detector. Thus, since naturally occurring germanium contains 7.8% ^{76}Ge, a double beta decay candidate, one makes a solid state detector out of Ge and does simple calorimetry. The different decay modes can be distinguished by differing electronic spectra: especially easy to search for is the neutrinoless mode indicated by a peak at the full decay energy. Such detectors have excellent energy resolution and, when operated underground with heavy passive or active local shielding to reduce cosmogenic and radioactive backgrounds, can provide good sensitivity to double beta decay. The source cannot be changed, however, and little other information is gained in this technique which can be used to reject background.[13]

There is as yet only one direct laboratory measurement of double beta decay, that of the two-neutrino decay mode in ^{82}Se. This was got by observing a sheet source of enriched ^{82}Se in a gas-filled time projection chamber. Topological information was used to reject backgrounds. Alpha decays were distinguished by short, dense ionization tracks. Single beta decays and Compton-scattered electrons away from the source were as easily identified. The results agree with geochronological measurements.[12]

Nuclear matrix element calculations suggest that the ^{100}Mo half-life could be much shorter than that of ^{82}Se. Prospects for confirming this prediction and the resultant increase in sensitivity to new physics makes ^{100}Mo an excellent candidate with which to study double beta decay.

This thesis describes an experiment which utilizes a novel, segmented array of lithium-

drifted silicon detectors to make possible the study of all modes of double beta decay of ^{100}Mo. In Chapter 2 an attempt is made to review at least those aspects of the theory germane to the interpretation of empirical results. Chapter 3 presents the experimental design (which has also been described elsewhere[15]). The data and analysis follow in Chapter 4, with a summary finishing the work.

Chapter 2

Theoretical Review and Summary of the Evidence

Even-even nuclei have ground states of spin and parity 0^+ and thus transitions $0^+ \rightarrow 0^+$ are sought in all double beta decays. Occasionally, decay to the daughter's first excited state is also energetically allowed, giving rise to $0^+ \rightarrow 2^+$ transitions. Due to the scarcity of low-lying states of any other spin and parity, only these two cases will be treated.

Naturally occurring, even-even parents exist in which double positron emission, positron emission with electron capture and double electron capture are possible decay modes. However, lifetimes and decay signatures are unfavorable for these processes. Among these, double K capture is the most probable, but such decays yield only neutrinos (and x-rays) in the final state; or, in the neutrinoless mode, are resonant reactions requiring improbable accidental degeneracies of initial and final state energies. The amplitude for positron emission with K capture is reduced because Coulomb repulsion between nucleus and positron decreases wave-function overlaps. In order for double positron emission to dominate over the preceeding reactions, the parent ground-state energy must be $2m_ec^2$ lower, and the resulting unfavorable energy release together with Coulomb suppression produces even longer lifetimes. Consequently we do not consider these processes.

The two-neutrino decay mode will be discussed first, together with a general review of nuclear matrix element calculations. A survey of the various mechanisms of neutrinoless decay follows. (Much of the discussion that follows can be found in the general reviews of

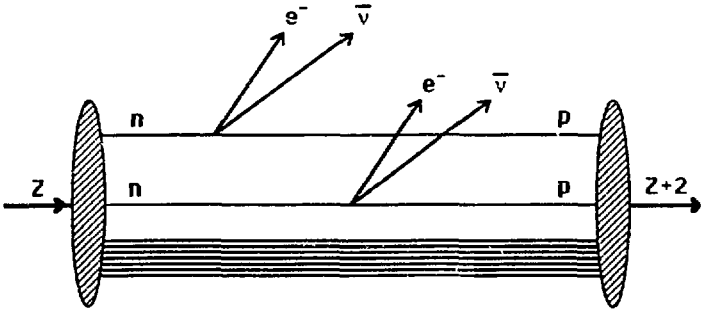

Figure 2.1: **Two-neutrino double beta decay.**

references [16] and [17].) After theoretical expectations for ^{100}Mo have been presented, a summary of the most stringent evidence to date will complete the chapter.

2.1 The Two-Neutrino Mode

Since two-neutrino double beta decay is allowed by the minimal Standard Model, small, new-physics augmentations can be neglected. This mode is understood as a second-order process (see Fig. 2.1) engendered by the effective Hamiltonian density governing low-momentum, semileptonic beta decay

$$H = \frac{G_F cos\theta}{\sqrt{2}} j_L \cdot J_L^\dagger + hermitian\ conjugate,$$

where G_F is the Fermi coupling coefficient, θ is the Cabbibo angle, and j_L and J_L are the left-handed leptonic and hadronic (i.e. nucleon) currents, respectively.

Nuclear and leptonic parts of the reaction can be treated separately. The hadronic amplitude is calculated using non-relativistic perturbation theory, giving sums of matrix elements over virtual intermediate states of the form

$$\sum_{jk} \sum_{n} \frac{\langle f|J_L^\dagger|n\rangle\langle n|J_L^\dagger|i\rangle}{(E_n - E_i)_{jk}},$$

where $(E_n - E_i)_{jk} = W_{ni} + E_{ej} + E_{\nu k}$. Here, W_{ni} is the energy difference between the initial and intermediate nuclear states and E_{ej} and $E_{\nu k}$ are energies of the j^{th} emitted

electron and the k^{th} emitted neutrino (with $j = 1,2$ and $k = 1,2$, corresponding to a particular association of electrons and neutrinos in the final state, and the "crossing diagram" with that association reversed).

The second sum is completed through closure ($\sum_n |n\rangle\langle n| = 1$) after the W_{ni} are replaced by an average value $\langle W_{ni}\rangle$. Estimates of $\langle W_{ni}\rangle$ are gained by doing statistical analyses based on, say, Fermi gas models of the nuclei. Alternatively, a weighted average for W_{ni} can be related to the empirically determined cross sections of charge exchange reactions, (p,n) and (n,p) in certain kinematic regions. The results are similar ($\langle W_{ni}\rangle \approx$ 10 MeV for most double beta decay parents) and may be treated as given.

This closure approximation, though routinely taken, is a most worrisome aspect of the theory. If the signs of the terms $\langle f|J_L^\dagger|n\rangle\langle n|J_L^\dagger|i\rangle$ were predominantly of one value for $(E_n - E_i)_{jk} < 0$ and the opposite value for $(E_n - E_i)_{jk} > 0$ then cancellations could result, reducing the amplitude. This possibility is especially troublesome for the two-neutrino decay mode calculation since leptonic emission energies are comparable with nuclear energy level differences. Only a few decay candidates have been tested for sign changes by actually calculating the $1/E$-weighted sum over many intermediate states; with little differences found compared to the closure result for those parents studied.

To a good approximation, the various $(E_n - E_i)_{jk}$ denominators can be simplified by setting $E_{ej}+E_{\nu k} = Q/2+m_ec^2$ in every case, where Q is the total energy release (typically 2-4 MeV in isotopes of experimental interest). The differential electronic contribution can then be evaluated and, if both electrons are assumed to be in relative S-wave states, is found for $0^+ \rightarrow 0^+$ transitions to be proportional to $(1 - \beta_1\beta_2 cos\phi)$, where $\beta_{1(2)}$ is the velocity of the first (second) emitted electron and ϕ is the angle between their velocity vectors. For $0^+ \rightarrow 2^+$ transitions, the angular correlation is given by $(1 + \frac{1}{3}\beta_1\beta_2 cos\phi)$. Physically, these results stem from parity violation in weak interactions: with fixed leptonic helicities, no other final states are allowed which conserve angular momentum. (It is possible for the electrons to be in P waves, resulting in different angular correlations, but overall decay rates wind up being highly suppressed.)

Energy is shared more or less equally among the final state leptons, regardless of which transition takes place. The sum-electronic energy spectrum depends on Q and the nuclear charge, and is shown for ^{100}Mo in Figure 2.2.

After integrating over phase space, and accounting for Coulombic effects, the total

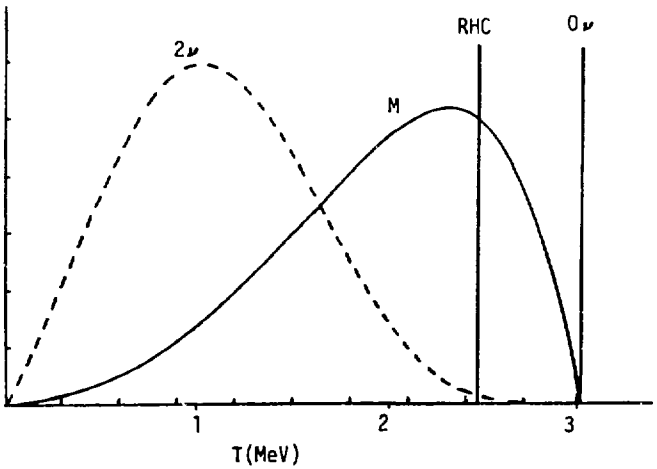

Figure 2.2: **Sum-electronic energy spectrum.**

The vertical scale is arbitrary. 2ν (dashed): two-neutrino decay, M: neutrinoless decay with the emission a Majoron, RHC: $0^+ \rightarrow 2^+$ neutrinoless decay (via right-handed currents). 0ν: $0^+ \rightarrow 0^+$ neutrinoless decay.

two-neutrino double beta decay rate (expressed as an inverse half-life) becomes

$$\frac{1}{\tau^{2\nu}_{1/2}} = \frac{G^{2\nu}(Q,Z)}{(\mu/m_e c^2)^2}|M^{2\nu}_{GT} - \frac{g_V^2}{g_A^2}M^{2\nu}_F|^2,$$

where $\mu = \langle W_{ni}\rangle + Q/2 + m_e c^2$ (for ^{100}Mo, $\mu \approx 11.4$ MeV). The hadronic currents have been treated in the impulse approximation leading to the Fermi and Gamow-Teller nuclear matrix elements

$$\begin{aligned} M^{2\nu}_{GT} &= \langle f|\sum_{j>k}(\sigma_j\sigma_k\tau_j\tau_k)|i\rangle \\ M^{2\nu}_{F} &= \langle f|\sum_{j>k}(\tau_j\tau_k)|i\rangle, \end{aligned}$$

where $\sigma_{j(k)}$ and $\tau_{j(k)}$ are the spin and isospin raising operators acting on neutron $j(k)$ of the initial nucleus. The factor $\frac{g_V}{g_A}$ accounts for strong-interaction disruption of pure $V-A$ hadronic currents. The coefficient $G^{2\nu}(Q,Z)$ contains all the numerical factors and in-

cludes integrated kinematical effects (phase space and Coulomb corrections). $G^{2\nu}(Q,Z)$ is a strong function of the nuclear charge Z and, as expected when there are four particles in the final state, is a polynomial in Q of leading order Q^{11}. (Table 2.1 lists the Q's and $G^{2\nu}(Q,Z)$'s for double beta decay candidates which involve large decay energies or which are accessible to geochronological techniques.)

A more accurate treatment would require the evaluation of separate kinematic factors and energy denominators multiplying the Fermi and Gamow-Teller matrix elements. However, estimates give $\langle W_{ni}\rangle_F \simeq \langle W_{ni}\rangle_{GT}$ for many cases. Also, the Gamow-Teller matrix elements are expected to dominate, so one can neglect $M_F^{2\nu}$. This happens because the double Fermi operator only connects states in the same isospin multiplet, and since the parent and daughter 0^+ states are in different multiplets with total isospin differing by two units the matrix element drops to zero. Due to Coulomb interactions, some mixing does occur but $|M_F^{2\nu}|$ remains the minority contribution.

A further word on the $0^+ \rightarrow 2^+$ transition is appropriate. Such decays can proceed only via double Gamow-Teller matrix elements, which bring with them factors of

$$\frac{j_L(e_1\nu_1)j_L(e_2\nu_2)}{(E_n-E_i)_{11}} + \frac{j_L(e_2\nu_2)j_L(e_1\nu_1)}{(E_n-E_i)_{22}} - \frac{j_L(e_1\nu_2)j_L(e_2\nu_1)}{(E_n-E_i)_{12}} - \frac{j_L(e_2\nu_1)j_L(e_1\nu_2)}{(E_n-E_i)_{21}}.$$

Given the approximations employed above, the rate for $0^+ \rightarrow 2^+$ transitions would vanish. Treated more carefully, decay rates are suppressed relative to $0^+ \rightarrow 0^+$ decays not only by the 11^{th} power of the ratio of energy releases but also by a factor of $(Q/\mu)^4$.

2.1.1 Nuclear Matrix Elements

In spite of the numerous approximations already made, most (except closure) are commonly accepted as reasonable in the calculation of decay rates. It is in the evaluation of nuclear matrix elements that paths among theorists diverge. This can be understood by noting the complexity of the endeavor. Ideally, one should solve the nuclear many-body problem with realistic nucleon-nucleon potentials to obtain a self-consistent set of wave functions. Nucleons would be allowed to form any configuration of states consistent with all conserved quantum numbers. The evaluation of matrix elements would then be straightforward. Unfortunately, for all but the lightest nuclei such a procedure is unfeasible. Severe reductions of the number of configurations accepted and of the complexity of the nuclear Hamiltonian are required. It is therefore important to test the calcula-

TRANSITION	$Q_{0^+-0^+}$	$Q_{0^+-2^+}$	NAT. ABUN.	$0^+ \rightarrow 0^+$ KINEMATICS $(G^{2\nu})^{-1}$	$(G^{0\nu}_{m_\nu \neq 0})^{-1}$	$(G^{0\nu}_{M})^{-1}$
	(keV)	(keV)	(%)	(yr)	(yr)	(yr)
$^{48}Ca \rightarrow {}^{48}Ti$	4272	3288	00.187	2.52E16	4.10E24	2.52E14
$^{76}Ge \rightarrow {}^{76}Se$	2045	1486	07.8	7.66E18	4.09E25	8.25E15
$^{82}Se \rightarrow {}^{92}Kr$	3005	2229	09.2	2.30E17	9.27E24	1.00E15
$^{96}Zr \rightarrow {}^{96}Mo$	3350	2572	0.28	5.19E16	4.46E24	
$^{100}Mo \rightarrow {}^{100}Ru$	3033	2493	09.6	1.06E17	5.70E24	5.76E14
$^{116}Cd \rightarrow {}^{116}Sn$	2808	1514	07.5	1.25E17	5.28E24	
$^{124}Sn \rightarrow {}^{124}Te$	2278	1675	05.64	5.93E17	9.48E24	
$^{128}Te \rightarrow {}^{128}Xe$	869	426	31.7	1.18E21	1.43E26	1.01E17
$^{130}Te \rightarrow {}^{130}Xe$	2433	1897	34.5	2.08E17	5.89E24	7.65E14
$^{136}Xe \rightarrow {}^{136}Ba$	2481	1662	08.9	2.07E17	5.52E24	7.37E14
$^{148}Nd \rightarrow {}^{148}Sm$	1928	1378	05.7	9.35E17	7.84E24	
$^{150}Nd \rightarrow {}^{150}Sm$	3367	3033	05.6	8.41E15	1.25E24	9.69E13
$^{238}U \rightarrow {}^{238}Pu$	1146	1102	99.3	1.47E18	1.68E24	

Table 2.1: **A Few Interesting Double Beta Decay Candidates.**
Only for ^{82}Se and ^{130}Te have definite measurements been made, whereas limits (or unconfirmed measurements) exist for the others. Read '1.2E14' as 1.2×10^{14}. 'NAT. ABUN.' indicates the natural abundance of the candidate isotope.

tions by (1) using identical procedures to calculate rates for related phenomena and (2) performing calculations for more than one parent and comparing results, especially in those cases in which double beta decay has been observed.

Shell-model calculations are closest in spirit to the ideal approach. Such efforts involving realistic internucleon potentials, modified only to account for allowed states in the intermediate nucleus, work well for lighter double beta emitters. For heavy nuclei, however, collective effects important in double beta decay can be included only partially. Closure and the weak coupling approximation are resorted to, to simplify the analysis.[18]

The most important collective effect in double beta decay comes from pairing correlations between like nucleons, leading to coherent contributions of many shells. This effect is included in calculations using Bardeen-Cooper-Schrieffer (BCS) or Hartree-Fock-Bogoliubov wave functions. The next step is to include neutron-proton forces, the dominant one being a spin-isospin polarization influence responsible for giant Gamow-Teller resonances. All these effects can be included in a Quasi-particle Random Phase Approximation (QRPA) approach based on BCS wave functions. Such a procedure permits an explicit, energy-weighted summation over intermediate states, avoiding the closure approximation. Its weakness, however, is that it utilizes phenomenological nucleon-nucleon interactions with a few adjustable parameters fitted to experimental pairing energies and the energies of Gamow-Teller resonances. The final interaction potentials are probably incomplete with regard to effects important in different phenomena, making it difficult to test the procedure.[19]

Of recent calculations, the ones agreeing best with experimental results make use of this QRPA approach. Empirically determined pairing, particle-particle (g_{pp}) and particle-hole coupling strengths are needed. In principle, shell-model calculations include such couplings, but have yielded decay rates that are too high when compared with measurements, often by as much as an order of magnitude. That three independent groups find lower decay rates using the QRPA approach lends credence to the implication that some new collective mechanism suppresses nuclear matrix elements.

This suppression is very sensitive to the particle-particle coupling strength, however, and there is no consensus as to its value. In fact, in the context of the approximations made g_{pp} may not act like a universal parameter, but may vary for isotopes of different atomic weights. It may even happen that matrix elements (and therefore decay rates)

vanish within the allowed range for g_{pp}. For these reasons, the predictive capabilities of this approach are severely compromised.

Nevertheless, there are QRPA indications that the nuclear matrix elements for ^{100}Mo are larger than those for many other isotopes. This is echoed, albeit qualitatively, by the naive shell-model argument that ^{100}Mo is unusual among double beta decay candidates in that the 1^+ ground state of the intermediate nucleus (^{100}Tc) is in the same shell as both the initial and final 0^+ ground states of the transition. With its additional kinematic advantages (due to a relatively high energy release and nuclear charge) ^{100}Mo should decay much faster, and a two-neutrino mode lifetime near 10^{19} years is not unexpected. The experimental accessibility of this lifetime makes ^{100}Mo a very promising candidate with which to test this understanding of nuclear physics.[20]

2.1.2 Loose Ends

Up to now the quarks taking part in double beta decay have been assumed to be in separate nucleons. Alternatively, due to π exchange among nucleons, a small equilibrium concentration of resonances (deltas) is thought to be maintained within nuclei, any one of which could double beta decay by itself. Possible two-neutrino mode transitions are depicted in Figure 2.3. In $0^+ \rightarrow 0^+$ decays, however, the $\Delta j = 1, 2$ transition of Figure 2.3a is incompatible with the nuclear selection rule $\Delta J = 0$ and so is forbidden. For the transitions of Figures 2.3b and 2.3c, angular momentum selection rules are circumvented, but decay rates are diminished by an additional factor (of order 0.01) indicative of $\Delta \stackrel{\pi}{\longleftrightarrow} n, p$ conversion probabilities. In $0^+ \rightarrow 2^+$ decays, the kinematic suppression discussed for the two nucleon mechanism operates in the same manner for all these transitions, considerably reducing decay rates.

Other heretofore neglected aspects of nuclear structure (such as ellipsoidal deformations) can affect decay rate calculations. For ^{48}Ca, if pairing forces were ignored, Lawson-Nilsson K-value differences between parent and daughter nuclei would prohibit double beta decay from occurring.[21] This suppression is largely preserved after pairing forces are re-introduced, offsetting any kinematic advantages gained by the high energy release.

For QRPA-based calculations, quadrupole-quadrupole interactions and short-range nucleon-nucleon repulsions cannot be neglected. These need not be explicitly incor-

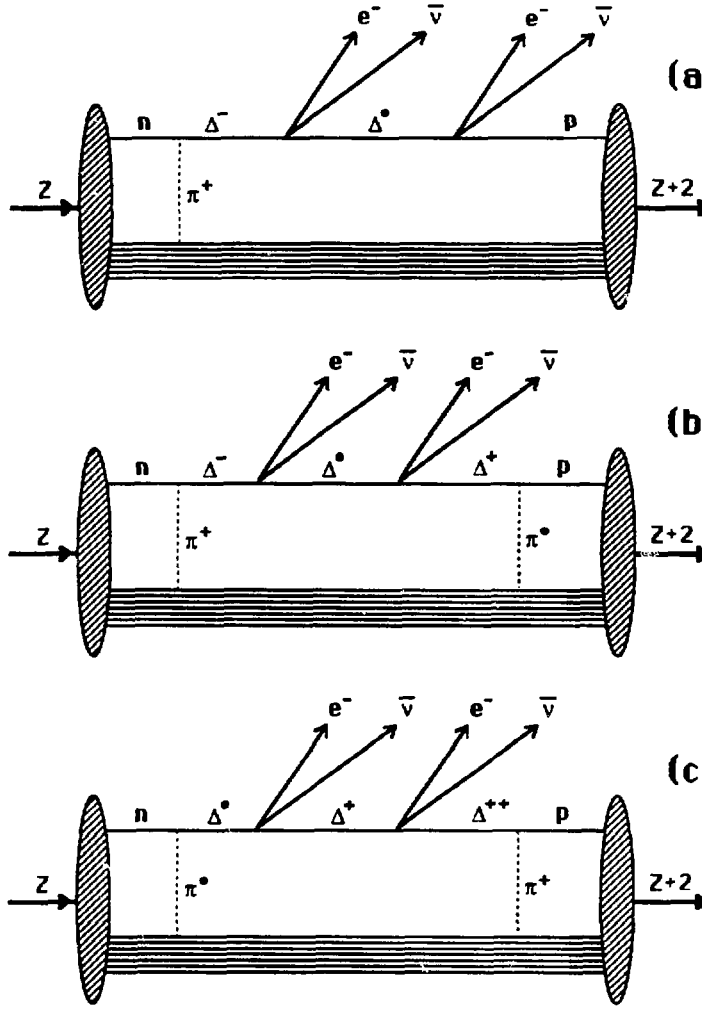

Figure 2.3: **Two-neutrino decay via the delta mechanism.**

porated, however, if g_{pp} is fixed by the strengths of certain positron-emitting decays (another process sensitive to these same effects).

The general suppression of double beta decay matrix elements relative to shell model expectations has recently been explained in a way which avoids the uncertainties of QRPA approaches.[22] If the Gamov-Teller matrix elements are expanded in a series of multiple commutators, the leading order terms can be shown to vanish. This result follows from the inability of double beta decay to take place within one nucleon, and is independent of any use of the closure approximation. Calculations based on this approach return reduced decay rates by factors of 6 or more compared with shell model results.

2.2 Neutrinoless Modes

Most of the above-mentioned two-neutrino mode suppression arguments apply equally well in neutrinoless double beta decay calculations. In fact, so many aspects remain unchanged (Gamow-Teller amplitudes are still dominant, non-relativistic impulse approximations are appropriate, etc.) a simple scaling relationship may be thought to exist between two-neutrino and neutrinoless matrix elements. There is some disagreement among theorists, however, about whether QRPA effects carry over. An essential computational difference between two-neutrino and neutrinoless decay is the presence of extra propagator terms. These terms vary according to what new type of virtual particle is exchanged (neutrinos, Higgs scalars, super-symmetric partners, etc.) and what mass it has. As a consequence, differing degrees of short-range nuclear correlations must be taken into account. In the QRPA approach, these correlations are not modelled uniquely. If the virtual, exchanged particle is a neutrino, however, then its momentum can be estimated as $p_\nu \approx \hbar/R$ where R is the nuclear radius ($p_\nu \approx 40$ MeV for ^{100}Mo). Since this is well above typical nuclear level-spacing energies, the closure approximation would seem to be better justified, and shell model calculations may become more reliable. In general, however, shell model results remain in disagreement, and the tenuous consistency among two-neutrino calculations is eroded when neutrinoless decays are considered.

When there are no other final state particles, the energy release is shared entirely by the electrons, and a delta-function in the sum-electronic energy spectrum is obtained (see

Fig. 2.2). (Nuclear recoil energies can be neglected.) This distinguishing feature of most neutrinoless decay modes constitutes the major empirical signature sought in direct-counting experiments. The separate energies and angular correlations of the electrons are also of importance. In the following, these aspects of the physical problem will be reviewed, together (briefly) with the theoretical bases for the various decay modes that have been proposed.

2.2.1 Massive Majorana Neutrinos

One reason why neutrinos are expected to be massive and Majorana in character in GUTs is simply that Majorana mass terms for all fermions are not otherwise forbidden, except by electric charge conservation in the cases of the charged leptons and quarks. Another reason is that baryon and lepton numbers are no longer conserved, so it would seem odd if this latter nonconservation did not infiltrate the neutrino sector and neutrinos were entirely Dirac in character. Still another reason is economy: Majorana neutrinos have only two states, the ones already known to occur, instead of the four associated with Dirac particles. Finally, there is the elegant and simple "see-saw" mechanism to account for the lightness of the left-handed neutrinos by introducing heavy right-handed partners. (This last result is a natural consequence of allowing any mass term consistent with conserved quantum numbers.[9])

Neutrinoless double beta decay is engendered by the virtual exchange between nucleons of a massive neutrino as pictured in Figure 2.4a. The combined effects of its Majorana character and a Lorentz boost allows this exchanged particle to be both emitted as a right-handed anti-neutrino and reabsorbed as a left-handed neutrino. In a calculation, if the neutrino mass is small compared to its virtual momentum, then this mass factors out of the indicated propagator as a multiplicative term, yielding

$$\frac{1}{\tau^{0\nu,m_\nu\neq 0}_{1/2}} = G^{0\nu}_{m_\nu\neq 0}(Q,Z)\left|M^{0\nu}_{GT} - \frac{g_V^2}{g_A^2}M^{0\nu}_F\right|^2\frac{\langle m_\nu\rangle^2}{(eV)^2},$$

where kinematic effects are incorporated in $G^{0\nu}_{m_\nu\neq 0}(Q,Z)$, which in this case is of leading order Q^5 (see Table 2.1). (Since a neutrino exchange gives rise to a neutrino potential, the intermediate state is not as simply described by its average energy, and the μ term encountered before in two-neutrino decay is subsumed into the matrix elements.) The effective exchange mass is given by $\langle m_\nu\rangle = \sum_i \phi_i|U_{ei}|^2 m_i$, where U_{ei} is an equivalent of the

Kobayashi-Maskowa matrix for neutrinos) is introduced to account for possible mixing among neutrino generations. Here, m_i is the mass of mass-eigenstate neutrino ν_i and ϕ_i is a phase factor which is essentially U_{ei}/U_{ei}^*. Now, if CP is a good symmetry, these phase factors become simply χ_i/i, where χ_i is the CP-parity of ν_i which, in turn, can be shown to be either $+i$ or $-i$.[23] If CP is violated, complex phase factors can appear. In either case, cancellations may occur in the sum for $\langle m_\nu \rangle$. For this reason, $\langle m_\nu \rangle$ represents the lower bound on the mass of at least one neutrino if neutrinoless double beta decay is observed. On the other hand, the absence of neutrinoless double beta decay at a given level would not imply an upper bound on the masses of any neutrinos.

Because of these cancellations, it is possible for the contributions of light neutrinos to be negligible compared to those of their heavier partners (if any exist). In this case a separation between particle and nuclear aspects of the problem is not so clean. The nuclear matrix element involves a Yukawa-like potential instead of a Coulombic one: short range nuclear correlations become very important. It is nevertheless possible to set a lower bound on the mass. Instead of $\langle m_\nu \rangle$, the decay rate is proportional to $R^2\langle 1/m_\nu \rangle^2$, where $\langle 1/m_\nu \rangle = \sum_i \phi_i |U_{ei}|^2/m_i$ is the effective, inverse mass and R is the nuclear radius.

In this decay mode (involving the exchange of massive neutrinos) the energy release is shared symmetrically between the two, final state electrons. Since there are no final state neutrinos, and since the electrons are most likely emitted in a relative S wave, $0^+ \rightarrow 2^+$ transitions are essentially forbidden. To conserve angular momentum, these electrons tend to be emitted in opposite directions in the allowed $0^+ \rightarrow 0^+$ transitions, and in fact the angular correlation is found to be given as $(1 - \beta_1\beta_2 cos\theta)$.

Special Case: Majoron Mode

Fermions acquire masses in the Standard Model by coupling to the Higgs boson. A variant of this mechanism has been suggested for the generation of neutrino masses. A new, massless Higgs scalar (the Majoron) is invoked which possesses two units of lepton number and which couples a neutrino to its opposite-helicity antineutrino.[24] In double beta decay, the emission of a real Majoron, M is enough to allow virtual neutrino emission and reabsorption to take place (see Fig. 2.4b), giving rise to $(A, Z) \rightarrow (A, Z+2)+2e^-+M$ transitions. The final state in such a decay consists of three emitted particles, only two

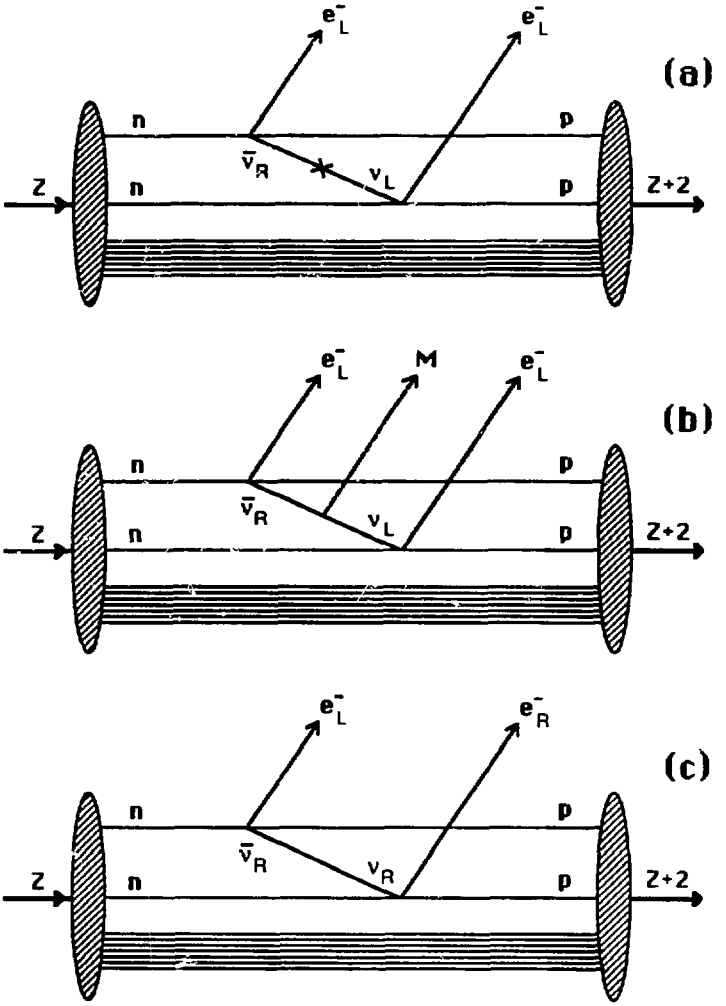

Figure 2.4: **Neutrinoless double beta decay modes** involving the exchange of Majorana neutrinos. a: decay via massive neutrinos, b: decay via the emission of a Majoron, c: decay via right-handed currents.

of which are leptons per se, but with a vanishing total lepton number.

Matrix elements are no different from those for the "purely" massive neutrino case discussed above, giving

$$\frac{1}{\tau_{1/2}^{0\nu,M}} = G_M^{0\nu}(Q,Z)|M_{GT}^{0\nu} - \frac{g_V^2}{g_A^2}M_F^{0\nu}|^2\langle g_M\rangle^2.$$

Decay rates now vary as Q^8 (a three-body phase-space effect, see Table 2.1) and the generation-averaged, Majoron-neutrino coupling constant $\langle g_M\rangle = \sum_{ij} g_{ij}U_{ei}U_{ej}$ must be incorporated. Majorons are spinless, so the angular correlation of the electrons is again proportional to $(1-\beta_1\beta_2 cos\theta)$ and $0^+ \rightarrow 2^+$ transitions are forbidden. Since the Majoron carries away some energy, the sum-electronic energy spectrum is smeared downward (see Fig. 2.2).

2.2.2 Right-Handed Currents

If parity is restored at some higher energy, then one expects right-handed currents to exist. In the presence of these currents, neutrinoless double beta decay could occur without the need for neutrinos to flip helicity. An emitted, right-handed antineutrino could be directly reabsorbed, if it were Majorana in character, as a right-handed neutrino (see Fig. 2.4c).

The low-momentum, effective Hamiltonian density is augmented by the existence of right-handed currents as follows...

$$H = \frac{G_F cos\theta}{\sqrt{2}}[j_L\cdot(J_L^\dagger + \kappa J_R^\dagger) + j_R\cdot(\eta J_L^\dagger + \lambda J_R^\dagger)] + hermitian\ conjugate$$

where $j_{L(R)}$ and $J_{L(R)}$ are the left-handed (right-handed) leptonic and hadronic currents, respectively. The leptonic currents are given as

$$j_L = \bar{e}\gamma(1-\gamma^5)\nu_{eL} \quad j_R = \bar{e}\gamma(1+\gamma^5)\nu_{eR}$$

with the generalizations $\nu_{eL} = \sum_i U_{ei}\nu_i$ and $\nu_{eR} = \sum_i V_{ei}\nu_i$, where the sums extend over the number of neutrino generations and the unitary transformation matrices are those which diagonalize the neutrino mass matrix. The parameters κ, η and λ are related to the masses and couplings of a given, high-energy theory (or GUT) and are to be determined by experiment. Thus, in the $SU(2)_L \times SU(2)_R \times U(1)$ gauge model $\lambda \approx (M_{WL}/M_{WR})^2$

and $\kappa \approx \eta \approx -\tan\zeta$, where $M_{WL(R)}$ is the mass of the left (right) gauge boson and ζ is the mixing angle between their mass eigenstates.

It was thought until recently that neutrinoless double beta decay could occur either because of nonzero Majorana neutrino masses or (if the Majorana neutrinos were massless) due to right-handed currents. That these two mechanisms are not independent can be understood as follows. In the context of the general gauge models herein considered (i.e. more "exotic" processes like Higgs or supersymmetric particle exchanges are ignored – to be taken up in the following section) one avoids violating unitarity if the left-handed and right-handed neutrino states are independent, or $\langle \nu_L | \nu_R \rangle = 0$; i.e. $\sum_i U_{ei} V_{ei}$ must vanish at high energies. But if all neutrino masses are degenerate (including the case in which they are zero) then the neutrinoless double beta decay amplitude is proportional to just this last sum. Therefore, the decay can proceed only if at least one neutrino has mass, regardless of whether there are right-handed currents.[25]

If massive neutrino effects are included, the total neutrinoless decay rate is

$$\frac{1}{\tau^{0\nu}_{1/2}} = |M^{0\nu}_{GT}|^2 \left[\begin{array}{c} C_1 \left(\frac{\langle m_\nu \rangle}{m_e}\right)^2 + C_2 \langle\lambda\rangle^2 + C_3 \langle\eta\rangle^2 \\ + C_4 Re\left(\frac{\langle m_\nu \rangle}{m_e}\langle\lambda\rangle\right) + C_5 Re\left(\frac{\langle m_\nu \rangle}{m_e}\langle\eta\rangle\right) + C_6 Re\left(\langle\lambda\rangle\langle\eta\rangle\right) \end{array} \right],$$

where $\langle\eta\rangle = \eta \sum_i U_{ei} V_{ei}$ and $\langle\lambda\rangle = \lambda \frac{cos\theta'}{cos\theta} \sum_i U_{ei} V_{ei}$. (The κ term is of second order and has been neglected.) Here, Re stands for the real part of the quantity in parentheses, θ is the Cabbibo angle and θ' is the Cabbibo angle for right-handed hadronic currents. The first term (proportional to C_1) is equal to $\frac{1}{\tau^{0\nu, m_\nu \neq 0}_{1/2}}$, and overall the six coefficients, C_i depend on eight matrix elements and nine kinematical factors. These kinematical factors vary as the fifth to seventh power of the energy release and are strong functions of the nuclear charge.

Why Q^7? In decay involving right-handed currents the final state electrons are emitted with opposite helicities. In $0^+ \rightarrow 0^+$ transitions, and if the electrons are in relative S-wave states, they must be emitted predominantly in the same direction to preserve angular momentum; i.e. their angular correlation is given by $(1 + \beta_1 \beta_2 cos\theta)$. This leads to an asymmetrical sharing of the energy release between the electrons: a purely algebraic consequence, due to sign differences encountered in calculations involving the scalar part of right-handed current contributions. The single-electron energy spectrum becomes bimodal, and this changes the integrated phase-space factor.

The vector-part consequences are much different. To preserve parity (and since vectorial factors are odd under parity) the electrons must be emitted in a relative P-wave state. Thus, $0^+ \rightarrow 2^+$ transitions are allowed in lowest order, if the electrons are emitted in opposite directions. As in the massive neutrino case, energy is again shared symmetrically between the electrons and a Q^5 decay rate dependence is obtained.

2.2.3 More, Exotic Mechanisms

The following mechanisms avoid the hypothesis that neutrinoless double beta decay must be mediated by Majorana neutrinos. In each, the final state left-handed electrons are expected to share the energy release symmetrically and to be emitted in a relative S-wave state and predominantly in opposite directions. Therefore, $0^+ \rightarrow 2^+$ transitions are forbidden, and decay rates are expected to vary as Q^5.

In the Higgs mode (see Fig. 2.5a) a doubly charged Higgs, emitted either by ordinary W gauge bosons or by a doublet Higgs pair, decays to two electrons. The likelihood for this process is in doubt, depending on the nature of the extra Higgs and coupling constants. Large suppression factors have been found, appropriate to the simplest cases in which these Higgs are responsible for the generation of quark and lepton masses. If more complicated Higgs are invoked, with couplings to fermions which are not given directly by the fermion masses, then neutrinoless double beta decay via this process is not necessarily suppressed.[26]

Within the context of supersymmetric (SUSY) models, neutrinoless double beta decay can occur if two quarks inside the nucleus emit either two squarks or sleptons which subsequently exchange a gaugino and emit two electrons (see Fig. 2.5b). In this scheme, non-gauge interactions are allowed, and lepton number violations occur through the breaking of R-symmetry; $R = (-1)^{3B+L+2S}$, where B, L and S are baryon number, lepton number and spin respectively. The decay rate is very sensitive to squark or slepton masses; so strong experimental limits on decay lifetimes may place stringent constraints on SUSY theories.[27]

Neutrinoless double beta decay could occur in first-order via a super-weak $\Delta L = 2$ interaction analogous to the $\Delta S = 2$ interaction postulated by Wolfenstein to account for CP violation in the decay $K^\circ \rightarrow \pi^+\pi^-$. Decay rates comparable to those for the two-neutrino mode are possible with a coupling constant on the order of $10^{-9}G_F$.[28]

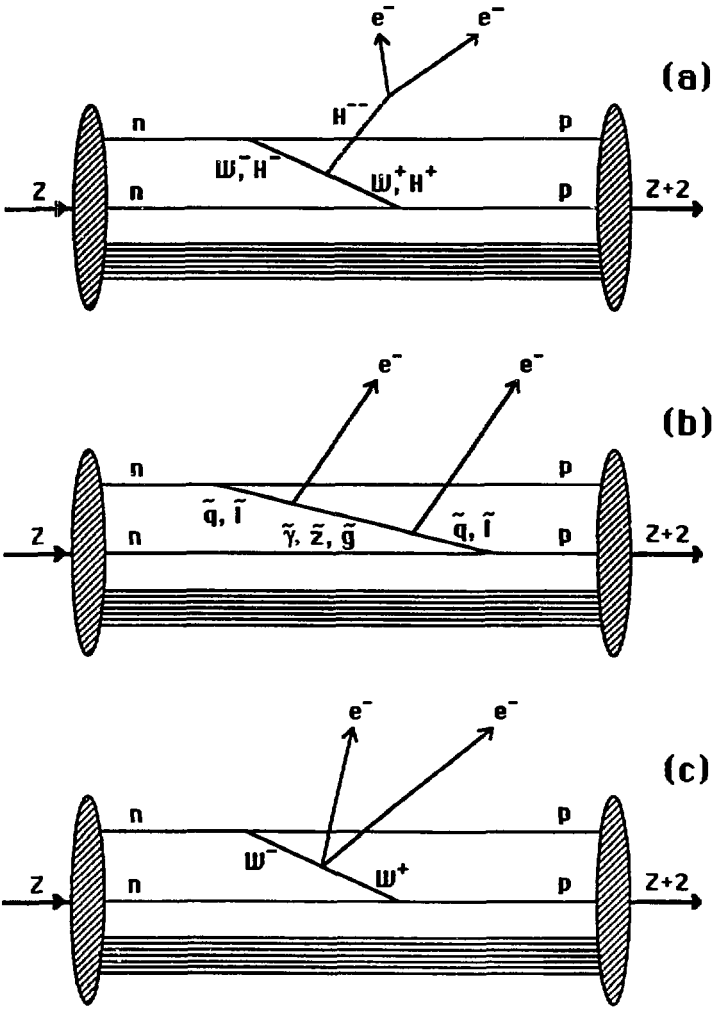

Figure 2.5: **"Exotic" neutrinoless double beta decay** not involving the exchange of Majorana neutrinos. a: decay via Higgs exchange, b: decay via supersymmetric particle exchange, c: decay via first-order $\Delta L = 2$ interactions.

2.3 Expectations for ^{100}Mo

Most theoretical work has concentrated on the isotopes ^{48}Ca (with matrix elements that are relatively easy to calculate) or ^{76}Ge, ^{82}Se, ^{128}Te and ^{130}Te because there has been extensive experimental activity directed their way (with strong limits set or measurements made). Only one modern calculation for ^{100}Mo is available (courtesy of Engel et al.[29]) and that is limited to the quantities $M^{2\nu}_{GT}/\mu$ and $M^{0\nu}_{GT}$. These are QRPA-based results, from which (when similar calculations were performed) accurate estimates of the lifetimes of ^{82}Se and ^{130}Te can be made. Unfortunately, of the three groups employing the QRPA approach and getting results which satisfy this accuracy test, Engel et al. returns values for g_{pp} (the particle-particle interaction strength) which are the least stable. (In other words. the measured lifetimes of ^{82}Se and ^{130}Te can be used to fix g_{pp} – here treated as a free parameter – but Engel et al. gets values for $g_{pp}(^{82}Se)$ and $g_{pp}(^{130}Te)$ that differ more than those of the other groups.)

The Engel et al. matrix elements are plotted in Figure 2.6 as they vary with the particle-particle interaction strength (here represented as a parameter α'_1). Also shown are the ranges of values indicated for this strength by the two-neutrino lifetimes of ^{82}Se and ^{130}Te (inclusive of extremes in measurement uncertainties) and by the rates of certain positron-emitting decays. The vertical lines connect two-neutrino half-lives (in years) with neutrinoless half-lives in the massive neutrino case where $\langle m_\nu \rangle = 1$ eV.

One can see from the figure that the half-life for neutrinoless decay (in the region indicated by auxiliary measurements) varies much more slowly with the particle-particle coupling strength than does the half-life for two-neutrino decay. This insensitivity to g_{pp} also holds for the other isotopes mentioned above and is a common result of QRPA calculations. (Engel et al. calculate matrix elements for only a few, particular values of α'_1. To interpolate between these values, smooth lines were drawn through the indicated points to make this figure. Therefore, the matrix element values plotted may be uncertain by small amounts, but still serve to indicate the range of half-lives expected and this, above-mentioned insensitivity of $\tau^{0\nu}_{1/2}$ to g_{pp}.)

Expectations for neutrinoless decay of ^{100}Mo involving right-handed currents are harder to establish. The nine kinematical factors have been calculated; but to date, no one has examined the ^{100}Mo case in establishing the eight necessary matrix elements. To-

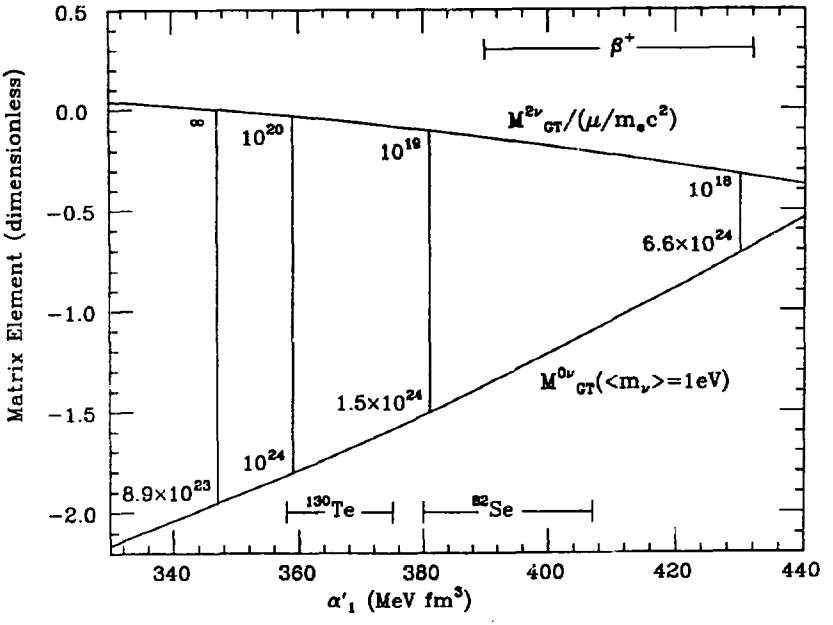

Figure 2.6: **Engel et al. results for ^{100}Mo**

α_1' is the particle-particle interaction strength; allowed ranges for which are indicated by the measured rates of ^{82}Se, ^{130}Te and certain positron-emitting decays. Vertical lines connect two-neutrino and neutrinoless matrix elements, with corresponding half-lives (in years) inset.

moda and Faessler have calculated these matrix elements for ^{76}Ge, ^{82}Se, ^{128}Te and ^{130}Te, however, and their QRPA-based results vary only slightly among these isotopes.[30] Such uniformity is echoed to some degree in most calculations regardless of the techniques employed. Assuming that the matrix element averages found by Tomoda and Faessler correctly represent the ^{100}Mo case (and rescaling the Doi et al.[17] kinematical factors to correspond with the former's conventions) we find...

$$\frac{10^{14}yr}{\tau^{0\nu}_{1/2}(^{100}Mo)} = |M^{0\nu}_{GT}|^2 \left[\begin{array}{c} 7.65\left(\frac{\langle m_\nu\rangle}{m_e}\right)^2 + 24\langle\lambda\rangle^2 + 260000\langle\eta\rangle^2 \\ -4.9Re\left(\frac{\langle m_\nu\rangle}{m_e}\langle\lambda\rangle\right) + 1100Re\left(\frac{\langle m_\nu\rangle}{m_e}\langle\eta\rangle\right) - 20Re\left(\langle\lambda\rangle\langle\eta\rangle\right) \end{array} \right].$$

For the overall scale, $|M^{0\nu}_{GT}|^2$ we must rely on Engel et al.. It is unknown what systematic differences would appear between the results of the two groups, Tomoda and Faessler and Engel et al., if they both calculated the same things. Consequently, the accuracy of this half-life formula is in some doubt.

There have been no calculations performed, QRPA-based or otherwise, regarding matrix elements for $0^+ \rightarrow 2^+$ transitions or "exotic" $0^+ \rightarrow 0^+$ transitions in ^{100}Mo. Neither are there many, modern results available for other isotopes which might be used to guess at ^{100}Mo transition rates.

2.4 Summary of the Evidence

This chapter will conclude with three short subsections in which the empirical status of double beta decay is examined. In the first, the best experimental results are presented. Next, experimental techniques are reviewed, providing a brief introduction to the details of the empirical situation. Finally, previous ^{100}Mo results are examined, establishing the context within which was performed the experiment that is the subject of this thesis.

2.4.1 Leading Experimental Results

Table 2.2 indicates some of the strongest double beta decay work that has been done. The ^{82}Se and ^{130}Te measurements were used in Figure 2.6 to indicate ranges for the particle-particle interaction strength. Integrated counting times are given in moles (of the candidate isotope) times years (of live time).

The most stringent limits on Majorana neutrino masses and right-handed current parameters are got through the neutrinoless ^{76}Ge results. Using the matrix elements of

Group	Parent	Mole-years	Mode	$\tau_{1/2}$ (yrs)
UCSB/LBL[13]	^{76}Ge	7.4	2ν	$> 1.9E20(68)$
		9.8	0ν	$> 7.0E23(68)$
		9.8	RHC	$> 2.0E23(68)$
		9.8	M	$> 1.4E21(68)$
UCI[14]	^{82}Se	.086	2ν	$(1.1^{+0.8}_{-0.3})E20$
			0ν	$> 1.8E22(68)$
			RHC	$> 3.4E21(68)$
			M	$> 1.6E21(68)$
Heidelberg[10]	^{82}Se	Geo.	all	$(1.3 \pm .05)E20$
	^{130}Te	Geo.	all	$(1.5 - 2.75)E21$
Missouri[11]	^{82}Se	Geo.	all	$(1.0 \pm .4)E20$
	^{130}Te	Geo.	all	$(7 \pm 2)E20$
INR, Moscow[33]	^{150}Nd	.077	2ν	$> 1.8E19(95)$
			0ν	$> 1.7E21(95)$
			RHC	$> 1.1E21(95)$
			M	$> 1.0E20(95)$

Table 2.2: **Experimental Results.**

M: Majoron mode, RHC: neutrinoless $0^+ \rightarrow 2^+$ transitions. 'Geo' indicates geochronological results. Read '$1E20$' as 1×10^{20}. The numbers in parentheses indicate the confidence levels (in percentages) assigned to the limits.

Tomoda and Faessler one finds;

$$\begin{aligned} \langle m_\nu \rangle &< 2.1eV, \\ \langle \lambda \rangle &< 2.9 \times 10^{-6}, \\ \langle \eta \rangle &< 2.3 \times 10^{-8}. \end{aligned}$$

We note that the limit on the effective neutrino mass, $\langle m_\nu \rangle$ is lower than those on $m_{\nu e}$ from tritium decay end-point experiments.[31] The restriction of $\langle \lambda \rangle$, if taken to indicate the ratio $(M_{WL}/M_{WR})^2$ gives a lower limit of 48 Tev on the mass of the right-handed W, much higher than the best limits from muon precession/decay experiments.[32] Of course both these results depend also on the likelihood that neutrinos are Majorana in character and that no large cancellations occur in the effective mass and coupling formulae.

The best limit on any Majoron coupling is provided by the ^{82}Se result...

$$\langle g_M \rangle < 3.8 \times 10^{-4},$$

again, using Tomoda and Faesslers' matrix elements.

It should be emphasized that, due to uncertainties in matrix elements, just one positive result is not enough. In order to establish convincing limits on Majoron neutrino masses (and on the other parameters of theoretical interest) consistency must be gained among experimental results and between theory and measurement for a number of decay modes and candidate isotopes. Thus, more theoretical work is called for in the evaluation of matrix elements for isotopes other than those mentioned in Section 2.3. Also, redundant measurements of (or limits on) lifetimes are necessary, especially for the expected two-neutrino decay mode.

2.4.2 Lessons on Experimental Technique

There are alternative ways of evaluating these experiments; emphasizing aspects that are independent of matrix elements, and of specific interest to prospective empiricists. It is clear, for instance, that large counting times are attainable in ^{76}Ge experiments, or ones like them which take advantage of isotopic sources which form a part of the detector. Large amounts of source can then be counted with good resolution in a compact volume. This aids in the avoidance of backgrounds, which often increase with detector size and

complexity. To improve upon this technique one should increase the relative source mass to that of the detector by using materials enriched in the candidate isotope. There are a number of groups currently pursuing this route; making solid state detectors out of enriched ^{76}Ge, making bolometric detectors out of solid samples of ^{100}Mo (or other isotopes), and constructing Time Projection Chambers (TPCs) with enriched ^{136}Xe gas fills.[34]

Another measure of the sensitivity of an experiment is the rate at which a certain limit can be reached, given the amount of source observed. To advance here is often a matter of rejecting background based on topological information. The Irvine, TPC experiment gains a great deal by being able to reconstruct each event. They can therefore distinguish between events involving one or two electrons, events in which two electrons originate from separate positions (which positions may not even be on the source plane) and events involving alpha particles. For double beta decay modes which return broad sum-electronic energy spectra, the loss of resolution to dead-source effects is of less influence.

It is evident that only a modicum of topological information helps considerably. The INR experiment with ^{150}Nd used a sheet source between scintillators and was therefore able to reject alpha backgrounds by ignoring events in which only one detector fired. They claimed the distribution of energy deposited between the detectors allowed them further to distinguish among decay modes.

The question of utilizing active versus passive local shielding is unsettled. Certainly, as in the above-mentioned ^{82}Se experiment, when the apparatus is operated essentially above-ground, an active cosmic ray veto is required. Deep underground, however, such vetos may contribute as much background, due to residual radioactive contamination of the materials employed, as is actively rejected. Clean passive local shielding may then prove advantageous. Although the UCSB/LBL experiment uses an active veto, other ^{76}Ge experiments which approach this one in sensitivity do not.

A number of other aspects prove germane to the empirical problem. An ability to replace the source to study backgrounds or to observe different candidate isotopes is desirable. Also, working with an isotope with a relatively large energy release provides increased sensitivity in two ways; (1) by the kinematic factor in the half-life which scales as Q^5 to Q^{11}, depending on decay mode, and (2) by placing the energy region-of-interest above that of most common radioactive backgrounds.

Group	Mole-years	Mode	$\tau_{1/2}$ (yrs)
Kiev[35]	.61	0ν	$> 2.1E21(68)$
Milan[36]		RHC	$> 2.0E18(90)$
Osaka[37]	.0067	2ν	$> 2.6E17(68)$
		0ν	$> 1.9E20(68)$
		RHC	$> 2.9E19(68)$
		M	$> 7.0E18(68)$
UCI[12]	.00076	2ν	$> 6.8E17(68)$
		0ν	$> 1.3E19(68)$
		M	$> 7.5E18(68)$
LBL/Mt.H/UNM[15]	.087	0ν	$> 1E22(1\sigma)$
	.022	2ν	$> 3.8E18(90)$
	.022	M	$> 3.3E20(90)$

Table 2.3: **Experimental Results on ^{100}Mo.**

2.4.3 ^{100}Mo Experiments and Results

Table 2.3 shows the ^{100}Mo results.

The Kiev apparatus consisted of many ^{100}Mo source foils, wrapped around scintillator bars, all viewed with a common phototube. Backgrounds were relatively high and energy resolution was poor, but a large counting time allowed the highest neutrinoless lifetime limit to be established.

Milan's design was simple; a lump of normal molybdenum was placed near a solid state germanium detector and the deexcitation gammas from $0^+ \rightarrow 2^+$ decay were sought. A low counting efficiency reduced the attainable limit.

Osaka utilized the same technique as is exploited in the present experiment: a set of enriched ^{100}Mo foils were interleaved between lithium-drifted silicon solid state detectors. Their source foils were relatively thick, however, and contaminated with ^{238}U and ^{232}Th at the 100 parts per billion (ppb) level. Their detectors were also thicker than those used in this experiment, and had $\approx 15\ \mu$m dead entrance windows on one side.

The UCI experiment resulted from replacing their ^{82}Se source with a sheet of normal molybdenum. They counted for only a short time, and their source was contaminated with 60 ppb of uranium and 30 ppb thorium. Nevertheless, through the use of their event reconstruction capabilities, they obtained the best two-neutrino and Majoron decay mode lifetimes.

In none of these experiments was a "dummy" source used, not containing ^{100}Mo. Consequently, some systematic effects in energy depositions and background contributions could not be studied. Also, the sources were all somewhat heavily contaminated, although the UCI technique avoided many of the associated problems.

Earlier results from the present experiment are listed last in Table 2.3. (Together with people at the Lawrence Berkeley Laboratory were collaborators from Mt. Holyoke College and the University of New Mexico.) Clearly, these limits provide a benchmark for ^{100}Mo experiments. The methods employed can be reviewed, for the most part, by following the remainder of this thesis. However, there is one major difference between current and earlier analyses: until now a dummy data sample has not been available. For the present work a completely independent investigation of backgrounds was mounted and, to maintain consistency within this thesis, new half-life limits were derived in a uniform manner. A comparison with earlier results will be presented in the concluding chapter.

Chapter 3

Description of the Experiment

In this experiment a coaxial array of 40 silicon detectors, interleaved with ^{100}Mo source films and mounted in a copper cage, was contained within a titanium cryostat and surrounded by a massive shield. The detectors were operated cold and under vacuum. Other films of ^{96}Mo, and some without any metal were substituted to study backgrounds.

Residual radioactivity within the materials used could constitute a major source of background in experiments of this type. To reduce this contribution, most of the materials herein employed in construction of the apparatus were selected on the basis of samples observed in a special, low-background counting facility at Lawrence Berkeley Laboratory (LBL). This facility consisted of a 28% efficient, high-purity germanium detector mounted in a low activity cryostat, housed within lead walls at least four inches thick, and surrounded on five sides by a scintillator, cosmic ray veto. With this setup, trace amounts of contaminations at the level of 1-10 ppb by weight of uranium and thorium could be detected, depending on counting time and sample size. Where available, the results of these measurements will be noted.

The following description of the apparatus will proceed from the outside (shielding) in toward the detector array.

3.1 Experimental Site

Cosmogenic backgrounds were all but eliminated by siting the experiment 4000 feet (3300 meters of water equivalent) underground in the disused Consolidated Silver mine near Osburn, Idaho. At that depth the muon flux is 0.44 ± 0.13 cm^{-2}sr^{-1}yr^{-1}, as was

measured by a stack of four, 1 ft.×2 ft.×1 in. scintillators operated in coincidence. (This value agrees with the published world average.[38])

Rock taken from underground was found to contain 3.3% potassium, 10.7 parts per million (ppm) thorium and 4.0 ppm uranium by weight. Also, radon daughter activity was measured at around 6 picocuries per liter of undisturbed air. A heavy, local shield and gas purge (to be described in more detail below) were used to reduce backgrounds from ^{40}K decays and from the ^{232}Th, ^{238}U and ^{235}U chains.

The experimental site consisted of an large, air conditioned enclosure, within which ambient conditions remained relatively stable year-round. The air flow pattern through the mine did change, however, necessitating a constant monitoring of the basal data collection rate, indicative of radon activity.

3.2 Shielding and Mechanical Apparatus

To thermalize and then capture incoming neutrons from ^{235}U fission within the rock, a shield consisting of 22 inches of wax (outermost) followed by 2-4 inches of 5% borated polyethylene was installed (see Figure 3.1).[39] These materials contained around 10 ppb of uranium by weight. Inbound of these and immediately surrounding the cryostat which housed the detector array was a 10 inch thick gamma ray absorber made of low activity lead (< 1 ppb of uranium or thorium by weight).[39] The polyethylene and lead shields were erected to disallow as many long, straight-line paths (cracks or gaps) through which radiation could penetrate to the innermost cavity (10 in.×10 in.×18 inches in height) as was consistent with a self-supporting structure.

A movable portion of one of the shield walls, mounted on a cart along with the cryostat and attached cooling, electronic and vacuum equipment, formed a door by which access could be gained to the cavity and detector array (see Figure 3.1). The cryostat extended through a 2×4 inch aperture in this door, and extra lead bricks and borated polyethylene pieces were fitted around the above-mentioned equipment to effectively close this hole. A separate cart on the common set of steel rails carried a portion of the outer wax shield. The entire shield provided estimated factors of 10^4 and 10^5 reductions in neutron and gamma ray induced backgrounds, respectively.

An inflatable mylar gasket was attached to the door and, when pressurized with boil-

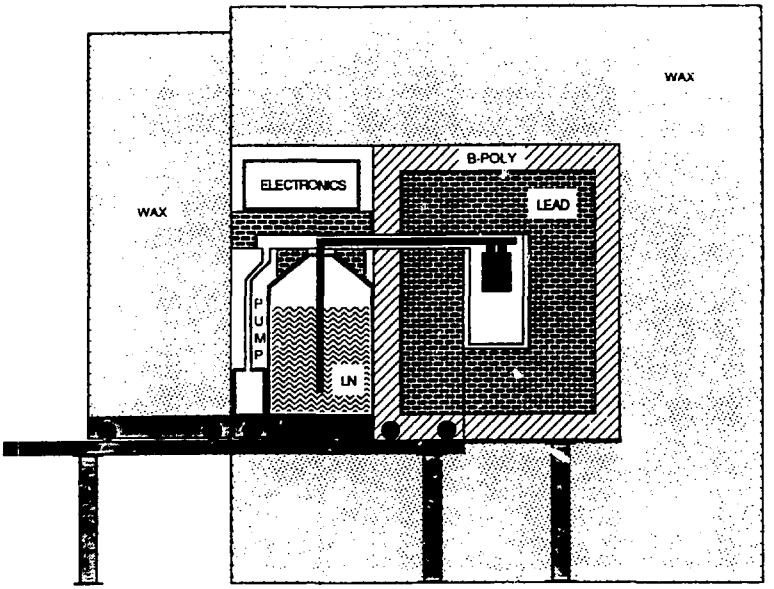

Figure 3.1: **Schematic elevation of the apparatus and shielding.**

off nitrogen gas effectively sealed the cavity from airborne radon backgrounds. Boil-off nitrogen was also used to flush the cavity.[39] About 13 liters of liquid nitrogen per day was used for these purposes, corresponding to a gas flow of $\approx$ 6 liters/minute. When the array was empty of source films, the raw data collection rate dropped from nearly 35 events per hour to around 13 events per hour as a result of implementing these measures.

The cryostat itself was made mostly of $\frac{1}{16}$ in. thick sheets of commercially pure titanium, welded together without using thoriated tungsten stingers. It was sealed with titanium screws and a pure indium wire gasket. The internal construction consisted almost entirely of oxygen-free high conductivity (OFHC) copper bar stock joined together with brass or OFHC copper screws. Indium foil, 5 mil thick, placed in the joints helped insure good thermal contact. The major materials were found to contain less than 1 ppb

of uranium and thorium.

The copper formed a four foot long, cantilevered cold finger from which the detector array hung. Its bulk (≈ 2 in^2 cross-section) allowed the array to be cooled to operating temperatures near 120 K in less than five hours. All copper surfaces were bright-dipped (cleaned with acid) and gold-plated to increase their reflectivity. A cold, 5 mil thick gold foil surrounding the array reflected infrared radiation from the cryostat walls. An ion pump maintained a vacuum of $\approx 9 \times 10^{-7}$ Torr inside the cryostat, thus avoiding convective heat flow. (For a clean, roughing pump a sorption pump was used first to reach pressures of $< 10^{-2}$ Torr.)

Cooling was accomplished by immersing the end of the cold finger into liquid nitrogen, contained in a 30 liter dewar. This dewar was automatically filled from a pressurized (10 PSI) 50 liter supply dewar. Filling could occur only during a hiatus in data collection, and was controlled though feedback from sensors inside the 30 liter dewar. (Data collection was resumed after a waiting period of 15-20 minutes, to allow time for boiling to cease and to avoid the associated microphonics.) Cooling needs of 7-8 liters of liquid nitrogen per day meant the system could run unattended for periods of up to 9 days.

Inside the cryostat, two cable ways on either side of the cold finger carried signal lines to/from the detectors. To reduce cross-talk between adjacent channels, lines from odd and even numbered detectors used different cable ways. These lines were approximately one meter long and made of RG174/U coaxial cabling, with ground braids removed to minimize possible sources of radioactivity and capacitance to ground seen at the input of the electronics. This lack of shielding resulted in less than 0.3% cross-talk between adjacent lines, relative to typical signal amplitudes.

3.3 Detectors, Support Structure and Contacts

The lithium-drifted silicon, Si(Li) detectors used in this experiment were 7.6 cm in diameter and 1.4 mm thick. They were fabricated at LBL as surface-barrier devices, requiring special techniques. P-type, single-crystal silicon was first lithium compensated to raise its resistivity well above the starting value of ≈ 2 kΩcm. This was accomplished by plating one surface of a cut and lapped crystal with lithium and applying an electric field across the device while it was heated to increase lithium ion mobility. A deep groove

had already been ground into the crystal to define the active region and provide a surface which was treated to decrease leakage around the edge of the device. The heavy, surface layer of lithium was then lapped off. An additional lithiation around the perimeter of the active region (just inside the grooves) was driven in to form an n-type, inverting contact. An N^+, surface barrier was formed by plating $20\mu g/cm^2$ of aluminum on this side. Gold, $40\mu g/cm^2$ thick was plated on the opposite surface to form a P^+, ohmic contact, which also served as the ground plane. Finally, hydrogenated, amorphous silicon was sputtered into the groove to adjust the electrical properties at the edge of the active region.

Finished detectors had active diameters of 6.86 cm, resulting in typical, fully depleted capacitances of 280 pF. They were essentially windowless with dead layers totalling only $60\mu g/cm^2$ of metal. They were extremely pure radioactively, being formed from zone refined silicon. Due to the surface treatments, they had to be operated well below room temperature if good signal-to-noise was desired. As a measure of their robustness, they usually survived many temperature cyclings with no degradation in performance. Occasional problems included a gradual increase in noise over a period of many weeks, or a decrease in breakdown voltages (which were often in the 100-200 volt range) following temperature cycling. Almost without fail, however, such problems could be successfully treated by reforming the contacts or sputtering new coatings of amorphous silicon into the grooves.

To operate the detectors a positive bias was applied to the aluminum surface. An energetic charged particle traversing the silicon ionized electrons, creating electron/hole pairs, which were then swept toward opposite surfaces by the electric field. In silicon, an average energy of 3.6 eV is needed to produce such a pair, and there is no charge multiplication, so the total collected charge was proportional to the total energy loss. Depletion (reach-through of the electric field) occurred at $\approx$ 40 V for the above detectors, but typical operating biases were 60-90 V. This produced a nonzero electric field throughout the interior, helping to guarantee full charge collection for minimum ionizing particles. For alpha particles this bias was still too low, however, since the field could not completely penetrate heavily-ionized tracks, and electron/hole recombination could occur.

The detectors were inserted into slots, cut at 0.1 inch intervals in two OFHC copper cold posts. Gold foil, infrared shields were attached to two OFHC copper plates screwed

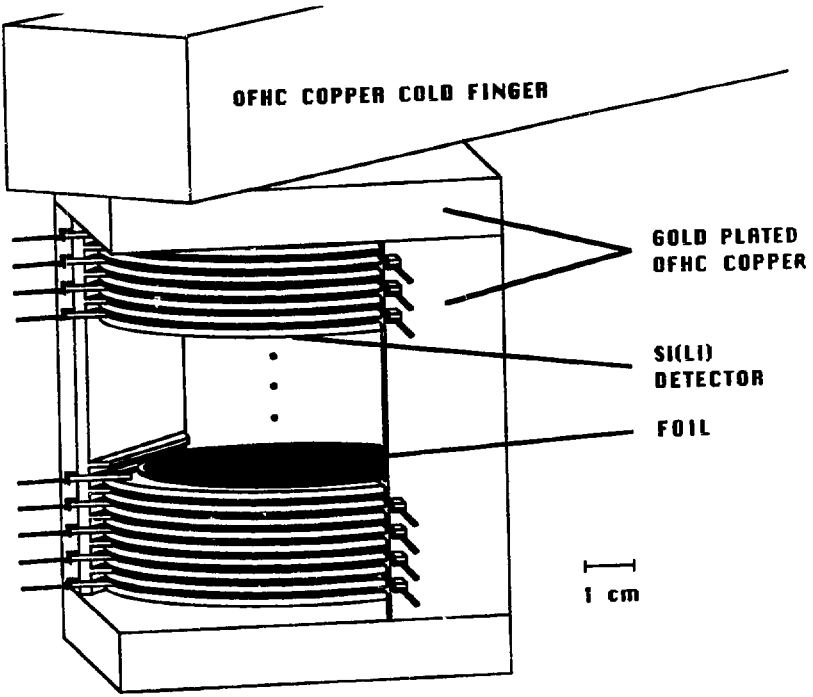

Figure 3.2: **Detector array and support structure.**

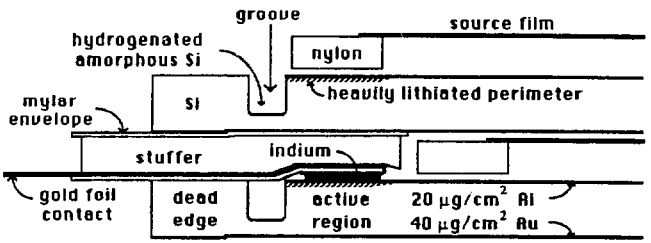

Figure 3.3: **Detail of electrical contacts.**

onto the ends of the posts. In order to reduce radiative heating of this "cage" through gaps in these shields, the foil had to be held flush to the copper surfaces. This entire arrangement was bolted to the cold finger (see Figure 3.2). Indium foil was placed in joints to insure thermal contact, and all screws were made of gold-plated, OFHC copper. The cage was positioned well below the level of the lead door hole through which the cold finger and cable ways extended. This prevented radiation originating outside the cavity from taking a direct path to the array.

Narrow strips of gold foil, enveloped in mylar, extended through alternating slots in the cold posts to make electrical contact with the detectors' aluminum surfaces. (see Figures 3.2 and 3.3) Thin indium pads pressed onto the gold at one end helped insure contact, while short lengths of gold-plated, stainless steel wire was soldered to the other end to provide thermal isolation from the signal lines. This assembly was wedged between detectors, holding them in place, with a folded "stuffer" of mylar. The detectors' gold surfaces, resting on copper in their slots, established the electrical grounds.

3.4 Source Films

For use in source films, 134 grams of isotopically enriched ^{100}Mo and about 20 grams of ^{96}Mo were obtained on loan from Oak Ridge National Laboratory. These were separated at the same time (from the same calutron runs in the late 1960's) and had not been used for any other experiments. The ^{100}Mo was $94.46 \pm 0.08\%$ pure. Enrichment factors were not given for the ^{96}Mo, but from earlier examples this sample was believed to be $98 \pm 2\%$ pure. From fission track counting performed by ORNL the ^{100}Mo was found to contain 3.2 ± 1.0 ppb uranium. Neutron activation analysis revealed 6 ± 3 ppb thorium by weight. No contamination levels were given for the ^{96}Mo sample. (Speculations as to the source(s) of uranium and thorium will be deferred until after comparative contamination levels are reported, as measured with the apparatus of this experiment.)

Source films were produced by collaborators at the University of New Mexico. The finely powdered metal was ultrasonically mixed with formvar, chloroform and cyclohexanone to form a slurry, a thin pouring of which was allowed to settle and dry in a mold. Assuming all the liquid evaporated, and there were no trapped gasses, the final films consisted of only metal and formvar. A large sample of formvar was observed in LBL's Low Background Counting Facility and found to contain less than 10 ppb of uranium and thorium.

Film	Effective Density	Thickness
formvar ("blank")	1.23 g/cc	5.01 ± 0.15 mg/cm^2
^{96}Mo	4.96 g/cc	31.91 ± 2.00 mg/cm^2
^{100}Mo	4.92 g/cc	33.90 ± 1.05 mg/cm^2

Table 3.1: **Effective film parameters.**

Three types of films were produced; one set with ^{100}Mo, one with ^{96}Mo and one without any metal (designated as "blanks"). The metal films were 85% molybdenum, 7% oxygen, 7% carbon and 1% hydrogen by weight; but also quite porous, at 60% empty space by volume. They were rather uniform, with less than 10% variations in thickness

routinely achieved. The purely formvar films bulged in the center, but were solid. For this experiment, the effective thicknesses and densities of films used are given in Table 3.1. (The uncertainties reflect film-to-film variations.) Metal-film depth was limited by fragility; thicker films tended to crack.

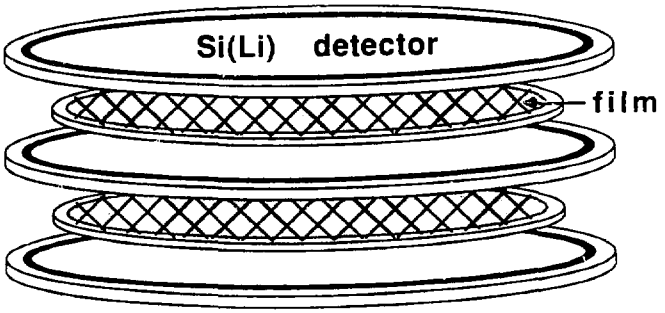

Figure 3.4: **Exploded view of the array.**

These films curled up when cooled to liquid nitrogen temperature. They were therefore constrained on circular nylon rings with nylon thread woven around them (see Figure 3.4). Films were 6.04 cm in diameter while the rings were of dimensions 6.38 cm O.D., 5.93 cm I.D. and 0.069 cm thick. The constraints prohibited electrical shorts and helped reduce noise caused by stray charges on microphonic films from imaging on the detectors. (No radioactive contamination could be seen in the small samples of nylon counted.) These assemblies were inserted in the $\approx$ 1.1 mm gaps between detectors. Coaxial stacking could not be achieved due to the presence of the electrical contacts, but offsets of 2 mm had to be tolerated; i.e. successive assemblies were inserted first 2 mm to the "right" of the array axis, then 2 mm to the "left", etc.. The films were mounted on top of the nylon rings, putting them 0.9 mm above and 0.2 mm below the nearest detector surfaces. The small ($\approx$ 0.6 mm) overlap of film-on-ring was essentially all that kept the full source area from being presented to the active detector surfaces.

3.5 Electronics and Calibration

The detectors were biased through isolation resistors off common voltage buses from two high voltage supplies. Signal/bias lines inside the cryostat were continued via BNC vacuum feedthroughs on patch-panels to 3 nanosecond lengths of RG58C/U cabling and then capacitively coupled to preamplifier inputs on two OFHC copper electronics boxes (one box each for all even and odd numbered detectors). From there each detector had its own electronic channel consisting of a charge sensitive preamp[40] followed by a conventional amplifier/shaper circuit and ADC in parallel with a fast timing circuit (see Figure 3.5).

Detector-plus-cabling capacitances of $\approx$ 350 pF were presented at the preamplifier inputs, necessitating the use of quiet preamps to avoid degrading the energy resolution with electronic noise. Large area FETs and GHz transistors provided a noise slope of approximately 15 eV/pf referenced to the input (with a 5 keV intercept) and a conversion gain of 22 mV per MeV of deposited energy in silicon. Each preamp output circuit was capable of driving a 50 Ω load, and was capacitively coupled to both the shaper and timing circuit inputs.

The signal shaper pole-zero compensated the preamp voltage output pulse, differentiated it, integrated it twice, and amplified it for a gain of 10. The two integration stages consisted of low-noise Op-Amps with 2.2 μs RC time constants. This circuit produced a unipolar, approximately gaussian voltage output pulse with a rise-time of 4 μs, satisfying ADC input requirements. Shaper outputs were connected via 50 ns, double-shielded coaxial cables to LeCroy CAMAC model 2259B, 11-bit peak sensing ADCs.

The timing circuit amplified the preamp pulse by means of a fast Op-Amp and then differentiated it to produce a unipolar output pulse with similar rise and fall times of approximately 100 ns. This circuit had a gain of 3 and a transistor output driver for 50 Ω loads. Fast timing pulses were sent down 50 ns cables to be amplified by an additional factor of 10, and then into discriminators set to trigger for inputs indicative of more than about 300 keV of deposited energy in silicon. All timing pulses above threshold were logically added to form a single trigger. This was delayed for 3 μs and then used to gate all ADCs for 2 μs, in coincidence with the peak of the signal shaper output.

An absolute energy calibration was carried out several times each year. The carts

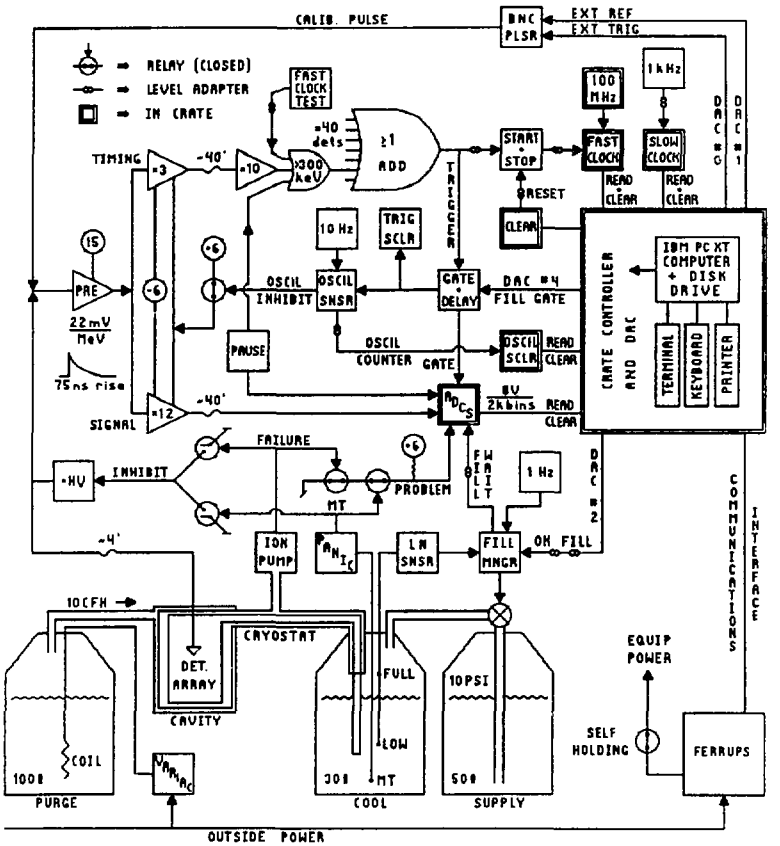

Figure 3.5: **Schematic of electronics and control systems.**

were rolled out and a thorium source was taped to the side of the cryostat. Double escape peaks from the 2.614 MeV transition of ^{208}Tl in each detector's spectrum were sought. These peaks were then fitted with gaussians, which averaged 14 keV in full width at half maximum (FWHM). The position of the Compton edge from this same transition helped confirm a detector's linearity.

The stability of the electronics chain from preamp to ADC was measured at the beginning of every data taking run. (Typically, only a few hours of down-time passed between runs.) A computer controlled series of pulses was sent through a 2 pf test capacitor into the input of each preamp. The digitized output from each ADC channel was then measured 40 times at 21 discrete and precisely known pulse heights. Above an equivalent deposited energy of about 1.2 MeV, the electronics were linear to better than 10 keV. ADC responses routinely drifted 10 keV at $\approx$ 3 MeV from run to run, however; but such drifts were accurately tracked by these procedures. The centroids of the double escape peaks in successive absolute energy calibrations were found to shift less than 6 keV, well within the FWHM resolution of 14 keV.

3.6 Safety Features

Two different computers were used during the course of this experiment; a Kinetics Systems micro, and then an IBM PC XT. Little difference in performance was noted. Regularly, during every data taking run, the computer monitored many critical systems. If any unusual condition was detected the computer would either make an adjustment or shut down the run, depending on the occurrence.

Nearly the entire experiment was powered through a 2 kVA uninterruptable power supply (labeled by its trade name, FERRUPS in Figure 3.5). This supply, which communicated with the computer via an RS-232 interface, acted as a line conditioner most of the time, but in the event of a power failure was capable of powering the experiment for more than 30 minutes on battery backup. If a failure longer than this occurred, the computer sensed steadily decreasing battery voltages and preserved any collected data by stopping the run. Eventually, if battery voltages dropped too far, a self-holding relay was tripped which kept the experiment shut down until it could be manually restarted.

In addition to liquid level sensors in the 30 liter cooling dewar which controlled

automatic filling (mentioned in Section 3.2) there was an "empty" sensor positioned just above the end of the cold finger dipstick. If the liquid nitrogen level dropped too low, this sensor would turn off the detector voltages (in order to avoid damaging them when they began to get warm). A signal would also be sent to a particular ADC channel, informing the computer of the shutdown.

The ion pump was so critically needed (to preserve the detectors from icing over with atmospheric vapors while under bias) that it was connected to this same system. In the event of a failure it too would cause the detector voltages to be turned off and a signal to be sent into an ADC channel.

The online software thresholds were also monitored. These were ADC levels, peculiar to each channel and known to the computer through a working file, below which no energy would be recorded as being deposited in that channel. The establishment of these thresholds helped exclude baseline noise in the signal circuits from entering the data. Typical thresholds of 70 keV were encountered, but occasionally these would need readjustment due to shifting noise levels. The computer sensed these shifts, and made the necessary changes.

The timing circuit sometimes entered into 1 MHz oscillations, often in response to glitches in line power due to mine pumps being switched on or off. By cycling the +6 volt power supply, these oscillations could be stopped. An oscillation sensor was therefore installed to monitor the trigger rate and, whenever that rate exceeded 10 Hz, the AC power to the +6 volt supply was turned off and back on. The number of times this cycling occurred during a run was recorded, through a signal sent to a CAMAC scaler. The dead time per cycling episode was only ≈ 2 seconds, and all cyclings usually accounted for less than 0.1% accumulated dead time per run.

3.7 Data Aquisition

Whenever an event triggered a gating of the ADCs, it also generated a Look At Me signal, which was received by the computer, and initiated an event readout (lasting from 10 ms to 100 ms depending on which computer was used). The energy deposited in each of the forty channels was then recorded if it exceeded the online software threshold. No information was kept as to which timing channel(s) delivered the pulse(s) that initiated

any readout.

The time, in milliseconds since the previous trigger was also recorded. This time interval was obtained by reading, and almost immediately clearing, a 24-bit CAMAC scaler which counted a 1 kHz pulser. This "slow" clock was read after the deposited energies were recorded, and so was not accurate to within the few milliseconds difference it took to record large events (with many channels containing energy) versus small events.

The event trigger also started a "fast" clock consisting of another 24-bit CAMAC scaler counting a 100 MHz pulser. If a second trigger occurred during the readout, this clock was stopped. Again, any information as to which timing channels delivered pulses that caused this clock to stop was lost: but more, the energy of the second event was lost (excepting that it was above discriminator thresholds). Furthermore, if a third (or fourth ...) trigger occurred during the readout, this information was also lost. At the finish of the readout this scaler was read and, if it had been stopped by a second trigger the elapsed time was recorded. If no other trigger had occurred, a zero was recorded. In either case, the fast clock was reset to be started by the next event.

Total live time was kept with reference to the onboard computer clock. At about 15 minute intervals during each run, data collection was stopped and the computer would interrogate all the systems mentioned in Section 3.6. A running log was kept of the raw data rate and of any problems encountered. These log files proved diagnostically useful when peculiarities in the data were found later.

At the end of each run, the data was fed through a crude but effective onsite summary program. A few, otherwise hidden problems could be discovered in this way; problems such as an inoperative fast clock, excessive oscillations, etc. The data was then stored on floppy disks and sent to LBL for analysis.

Chapter 4

Data and Analysis

As suggested at the end of Chapter 2, the segmented design of this experiment provided considerable advantages. It permitted the rejection of many backgrounds and, by removing and/or replacing the source films, remaining backgrounds could be studied in some detail. The following discussion covers all aspects of this endeavor; from the characteristics of gathered data to the Monte Carlo simulations and physical assumptions on which analyses were based, and finally to the reduced spectra in which double beta decay signals were sought. The treatment is rather extended; many modes of broad-spectrum double beta decay were studied, and multiple background contributions had to be examined.

4.1 The Data

Detectors were numbered from the bottom, making the uppermost detector #40. Further characteristics of the data include; what operational peculiarities were encountered, when and where source films were placed in the array and with what integrated counting times they were observed. The latter factor(s) could not be established without first defining what data was to be accepted. A review of acceptance criteria might properly follow the assessment of backgrounds, but is given in this section because only minor portions of data were rejected.

4.1.1 Survey

The data analyzed in this experiment was taken from 1 May 1987 to 19 Sept. 1988. Seven separate series of runs were initiated during which source films were deployed in different arrangements. (Before this time, the experiment had been operated above ground and then underground with rather badly contaminated films or in shakedown runs, identified as series 1-12.) In the following itemization, the start and stop dates of each series are given in parentheses after the series numbers.

Series 13 (1 May to 12 June, 1987) No films were in the array.

Series 14 (19 June to 10 July, 1987) 20 ^{100}Mo films were placed above detectors #19-38, with one rather more contaminated film above detector #18.

Series 15 (17 July to 21 August, 1987) The contaminated film of series 14 was removed, and 12 blank films (not containing molybdenum in any form) were placed above detectors #6-17.

Series 16 (28 August to 4 November, 1987) 2 more blank films were added above detectors #4 and 5.

Series 17K (18 Nov. 1987 to 21 March 1988) The blank films of series 16 were removed and 16 more ^{100}Mo films were placed above detectors #3-18. This was the last series in which the Kinetics Systems microcomputer was used.

Series 17I (21 March to 31 May, 1988) The IBM PC XT computer was installed. Otherwise this series was identical to that above.

Series 18 (6 June to 19 September, 1988) The ^{100}Mo films above detectors #18-38 were removed and 20 ^{96}Mo films were placed above detectors #19-38.

Thus, four data samples could be distinguished; an "Empty" sample (series 13), a "Blank" sample (from the lower region of the array in series 15 and 16), a ^{96}Mo sample (upper array, series 18) and a ^{100}Mo sample (from various regions of the array throughout series 14-18).

The following points serve to specify the instrumental circumstances encountered when these data were taken

- The slow clock was inoperative during part of series 13, and the fast clock was inoperative during all of series 15.

- A curious (and unexplained) periodicity appeared in slow-clock times for those runs taken with the Kinetics Systems microcomputer. Even though the clock speed remained 1 kHz, this effectively broadened the slow-clock resolution (the accuracy with which time intervals between event readouts could be measured) to around 50 ms.

- Readout times differed between runs taken with the Kinetic Systems microcomputer and those taken with the IBM PC XT. For the former, readout times were 85 ± 10 ms, depending on how "large" the event was (i.e. how many detectors were involved). For the latter, readout times were 16 ± 5 ms. These differences had their roots in (1) differing clock speeds of the two computers and (2) relative efficiencies of the programming languages used.

- The fast clock facility could not distinguish between two triggers occurring closer together than about 100 ns. This was simply a consequence of the $\approx$ 100 ns width of timing pulses. By sending a series of closely spaced pulses through the timing circuits, it was determined that the fast clock became 100% efficient only for events occurring at least 200 ns apart. Timing accuracy remained at 10 ns, set by the clock speed.

- Occasionally, ertain channels, large timing pulses were echoed (i.e. double pulsing occurred in events when > 4 MeV was deposited in a detector) rendering fast-clock timing useless for events less than ≈ 3 μs apart, for those channels.

- The discriminator (trigger) thresholds averaged 315 ± 15 keV throughout the array; but the highest such threshold was nearly 500 keV.

- Online software thresholds averaged 70 ± 20 keV throughout the array; with the highest around 100 keV.

- The ADCs saturated at pulse heights equivalent to $\approx$ 7.6 MeV of deposited energy in silicon.

- Due to absent detectors, weak electrical contacts, low breakdown voltages or large noise problems a number of channels in each series of runs were declared "bad" and either disconnected from their bias supply or had their inputs removed from corresponding ADC ports. These included;

Series	Bad Channels	Live Time (hr)
13	1,3,14,15,18,19	883.53
14	1,2 3,14,33	396.62
15	1,2,3,4,9,14,21,33	302.67
16	1,2	1283.66
17K	1,2,11,21,32,40	2530.95
17I	1,2,11,21,32,40	1385.87
18	15,38	2154.77

Table 4.1: **Bad channels encountered.**

- A few channels tended to be noisy enough to warrant removal from the trigger, but not from their ADCs. Energy deposited in the indicated detectors would still be recorded, but could not have caused event readouts to occur. These included channel #40 in series 13 and 14, and channel #23 for the last 557.31 hours of series 17K and throughout series 17I.

- There was a degree of cross-talk between certain channels. This was traced to their proximity in that they either shared the same timing circuit board or they entered into adjacent ADC ports. Relative cross-talk pulse heights of under 5% were typical.

4.1.2 Criteria of Acceptance

The determination of what data was accepted for analysis took a number of factors into account. Not the least of these was an increase in raw data collection rate at the beginning of some runs after the cavity had been opened. This was due to the unfinished flushing of the cavity and/or the uncompleted decay of radon in the cavity. Usually after an hour or two data collection rates stabilized at their typical, low levels. Since radon daughters

constituted potential background sources, the first portion of any run displaying this increased collection rate was excised, resulting in only miniscule reductions in integrated counting times.

Data from series 13 indicated that empty backgrounds in the upper and lower sections of the array differed. This difference manifested itself not only in the energy spectra, but in the multiplicities of events (or, how many detectors "fired" in each event). Moreover, an increased event-rate involving detectors #11-13 persisted throughout the entire series of runs, suggestive of the presence of a radioactive "hot spot". Also, the lower section of the array tended to be punctuated with many bad channels. When reasonable cuts were made to avoid these dirty(?) detectors and account for bad channels, collection efficiencies for any type of signal in this lower section, including signals indicative of double beta decay, were severely depressed. Furthermore, the most reliable form of non-film backgrounds - from reduced ^{96}Mo data - was noncommittal about contributions from below detector #19. As a consequence, in order to maintain a uniformity in backgrounds and to avoid collection efficiency uncertainties, only data from the upper section of the array were included in subsequent searches for double beta decay. The complexity of the analysis was thereby reduced, and the resulting half-life limits became more reliable, compensating for any moderate loss of integrated ^{100}Mo counting time.

By considering only those films above detector #19, 19.425 grams in 20 ^{100}Mo films were observed in series 14-17, 16.47 grams of which was metal, for $(9.37 \pm 0.01) \times 10^{22}$ atoms of ^{100}Mo. Also, 18.286 grams in 20 ^{96}Mo films were observed in series 18, 15.63 grams of which was metal. For studying contaminations in formvar alone, the lower section of the array in series 16 had to be examined. In the 14 blank films installed there were 2.01 grams of formvar.

As the analysis proceeded, it became clear that fast clock information not only helped in determining contamination levels, but the fact that many fast-clock times were nonzero was crucial for vetoing background events. Hence, the entire series 15 was eliminated, resulting in only a $\approx 5\%$ drop in integrated ^{100}Mo counting time.

In the analysis to be presented care was taken to assess differing contamination levels indicated in the various series of runs. Such differences could occur if there were any sources in the array (other than the films above detector #19) which were radioactive. Also, variations in electronic communications efficiencies between Kinetics Systems and

IBM PC XT computer controllers could artificially change collection rates. For the most part, no statistically significant differences were found. Event rates in the upper region of the array changed very little when blank films, and then ^{100}Mo films were installed in the bottom. Therefore, series 14, 16 and 17 were added together to form one ^{100}Mo data sample.

After accounting for these factors, the following total live times were established. The total ^{100}Mo exposure was therefore (36.28 ± 0.03) mole days.

Data Sample	Empty	Blank	^{96}Mo	^{100}Mo
Live time (hr)	883.53	1283.66	2154.77	5597.10

Table 4.2: **Live times of exposure.**

4.1.3 Preliminary Cuts

Some preliminary off-line processing of data was instituted to eliminate variations in detector/electronics characteristics. Thereafter, all channels could be treated as responding in a uniform manner, and one source of uncertainty in signal collection efficiencies (to be described later) was removed.

The first adjustment made was to force bad channels to be completely dead. Any energy (accidentally or circumstantially) recorded in a bad channel was set to zero.

Next, an off-line threshold of 110 keV was imposed. Any channel with less than 110 keV of recorded energy was removed from the event, regardless of which channel it was. Thus, a "contiguous" three-detector event in which the middle detector contained energy less than this threshold became a separated, two-detector event.

Cross-talk between channels was much reduced by imposing a cut on the ratio of energies recorded in different channels. All detectors containing less than $1/20^{th}$ of the energy recorded in any other detector were eliminated from the event. Thus, a multi-detector event with noise in an isolated channel became more contiguous with the removal of the noisy channel.

Only after these adjustments were made did each event become characterized as to which detectors were involved and what the recorded energies were. Certainly, some very

minimal decrease in the collection efficiency for double beta decays had to be tolerated. The cleanliness of the data samples were, however, significantly improved.

The establishment of a common, off-line trigger threshold was delayed until final analyses were begun. For the most part, this threshold could be set at 500 keV when searches were made for signals from double beta decay or from many backgrounds. In certain cases to be described below, however, the average value of 315 keV was more appropriate.

4.1.4 Reconnoiter: Trigger Rates and Spectra

A 10 cm high stack of forty detectors, each with 37 cm^2 active areas, presents $\approx$ 14 cm^2sr to incoming, long range particles. During the 0.99 year total live time of this experiment (through series 13-18) 8 events occurred in which > 400 keV of energy was deposited in each of at least 10 detectors. (For minimum ionizing particles, the most probable energy loss in 1.4 mm of silicon is $\approx$ 430 keV.) Assuming these were caused by cosmic ray muons, the flux indicated was 0.6 ± 0.2 $cm^{-2}sr^{-1}yr^{-1}$, consistent with that measured by the stack of scintillators.

When the ^{100}Mo films were installed, raw data collection rates rose by a factor of 5, to $\approx$ 65 events/hr. Events came distributed in energy from discriminator thresholds to ADC saturation levels (see Figure 4.2). If broad-spectrum, two-neutrino double beta decay half-life sensitivities of over 10^{20} years were desired (corresponding to event rates of at most 6.6 hr^{-1} with perfect collection) then a systematic study of backgrounds had to be instituted.

After accounting for bad channels and the presence or absence of films, events were more or less randomly distributed among the various detectors. The typical multiplicity (number of detectors firing) was quite low, averaging just over unity throughout all series. One-detector events dominated the data for all energies up to 9 MeV (see Figure 4.3).

4.2 The Monte Carlo

In this experiment extensive Monte Carlo simulations were required to predict double beta decay signatures, obtain collection efficiencies, study backgrounds, etc. Two programs were developed; one written by collaborators in the experiment, and GEANT311,

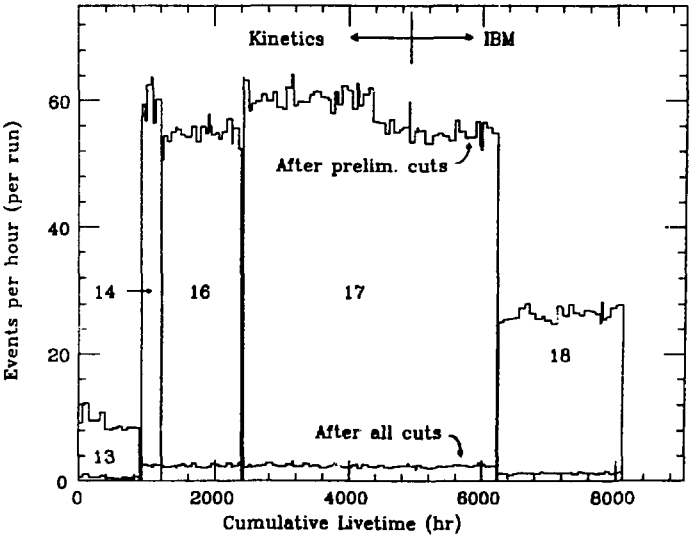

Figure 4.1: **Data collection rates for runs used.**

Preliminary cuts were imposed. Data from the lower region of the array were excluded. Series numbers are inscribed. The lower histogram was obtained after cuts described in sections 4.1.3 and 4.4.1 were imposed (except that of limiting energies to > 1.4 MeV).

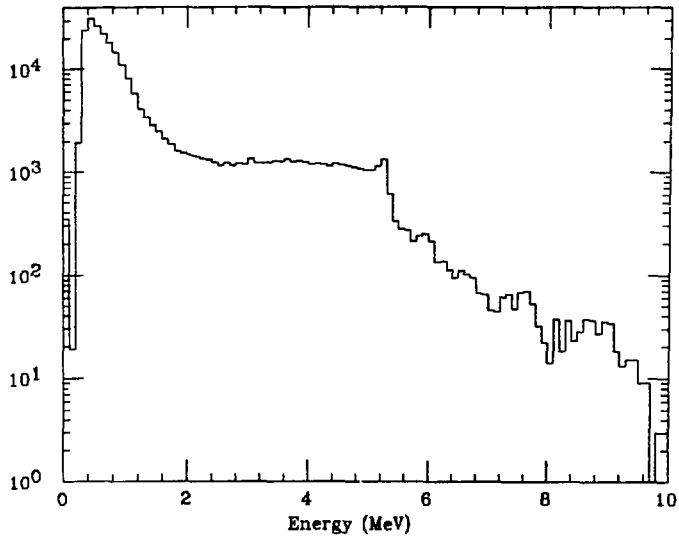

Figure 4.2: **Spectrum of events in the ^{100}Mo data sample.**
Preliminary cuts were imposed. Data from the lower region of the array were excluded.

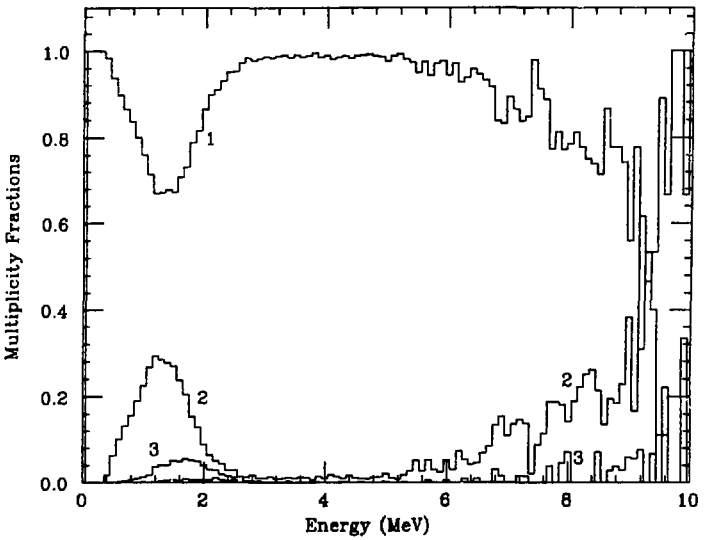

Figure 4.3: **Fractions of events in the ^{100}Mo data sample.**
The number of detectors involved in each event is the parameter. (Preliminary cuts were imposed. Data from the lower region of the array were excluded.

a large multipurpose code constructed at CERN.[41] The latter was more complete with respect to capabilities and physical processes. It also proved more accurate, after being augmented for use at such low energies as were encountered in this experiment, and so became the preferred event simulator. (All accumulated experience and intimate knowledge of the in-house program was not abandoned, however, but provided a foundation on which to assess GEANT311 advantages.)

4.2.1 Features and Accuracy

The basic Monte Carlo assignment was to track electrons through various materials, calculating energy loss and scattering appropriately with each step. To do so accurately while simultaneously improving the speed with which events were simulated required a balanced tuning of the step size. Steps rather shorter than film or detector thicknesses were needed, but could not be so small that thousands of time consuming iterations were taken in every event, resulting in possibly large cumulative errors. Step sizes corresponding to ≈ 100 atomic collisions were chosen, allowing a full Moliere treatment of scattering to be performed.

Energy losses for steps of this size ($\approx 50\mu$ in Si, $\approx 12\mu$ in Mo, both decreasing with β^2) varied statistically as described by a Landau distribution.[44] A comparison of average and most probable energy losses with expectations is shown in Figure 4.4. Bremsstrahlung losses were neglected for this Figure, but were reestablished in subsequent analyses. The discrepancy between GEANT311 results and expectations from the literature for $(dE/dx)_{avg}$ in molybdenum stem from truncating Monte Carlo output at high values. Large, single-collision losses did occur, and knock-on electrons were separately tracked.

Cumulative errors were assessed by simulating events in which a beam of electrons was directed into blocks of silicon. For normal incidence, extrapolated ranges and backscattering fractions were compared with semiempirical formulae (see Figures 4.5 and 4.6). The agreement was quite satisfactory. For oblique incidence, backscattering fractions increased as expected.[47] Simulations involving molybdenum blocks displayed similar agreement.

The next most important Monte Carlo assignment was to track gamma rays through the array. In GEANT311 pair production, Compton scattering and photoabsorption

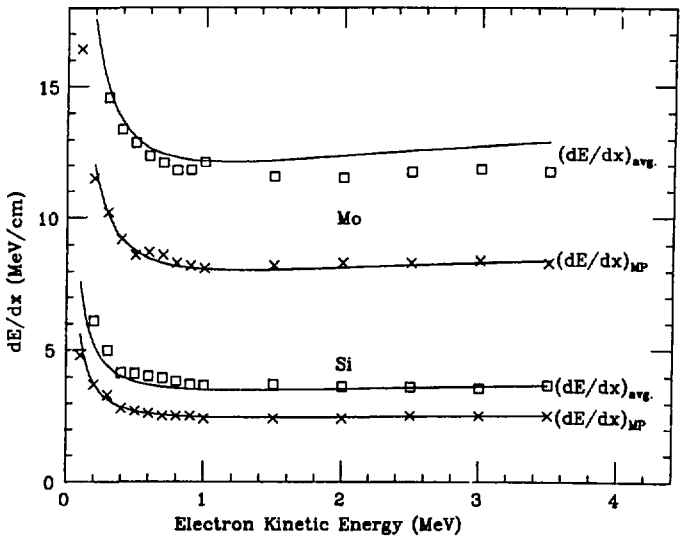

Figure 4.4: **Energy loss vs. kinetic energy for electrons.**
The curves indicate expectations taken from references [42] and [43]. Data points result from Monte Carlo analysis.

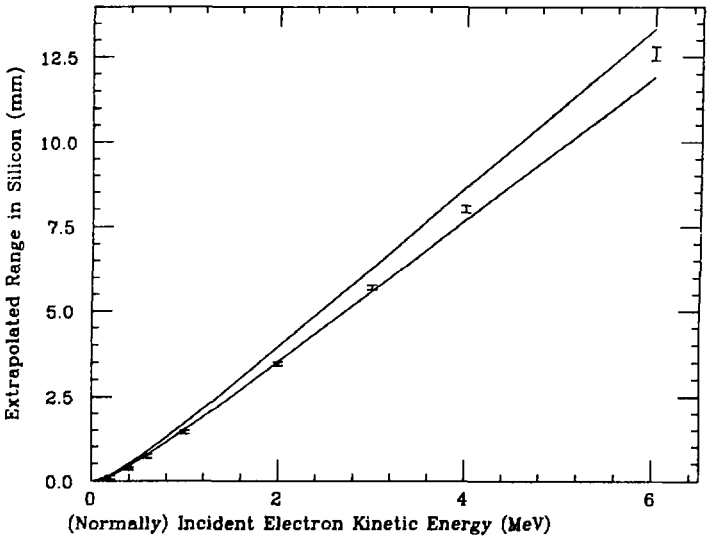

Figure 4.5: **Electron extrapolated range vs. kinetic energy in silicon.** The two curves indicate extremes of values allowed by the semiempirical formulae of [45]. Data points indicate Monte Carlo results.

were all incorporated. By simulating gamma rays of different energies entering thick silicon and molybdenum absorbers, the attenuation lengths plotted in Figure 4.7 were obtained. Positrons from pair production were accurately followed, with annihilation gammas emitted at the ends of their tracks.

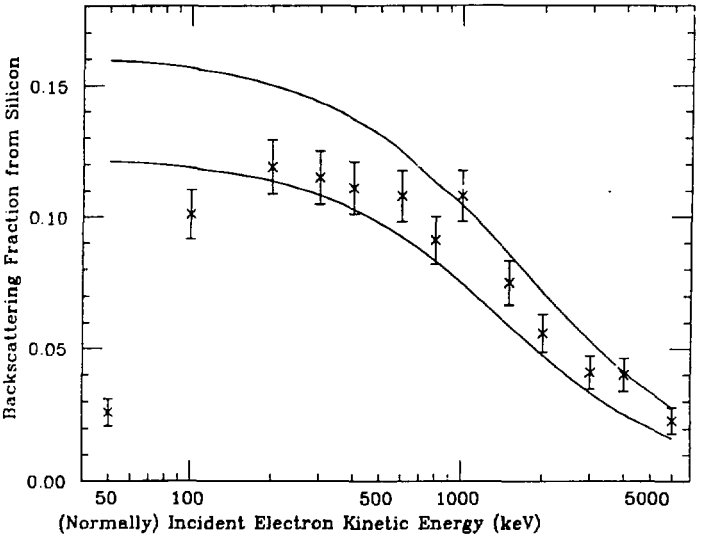

Figure 4.6: **Electron backscattering vs. incident energy in silicon.** The two curve indicate extremes of values allowed by the semiempirical formulae of [46]. Data points indicate Monte Carlo results.

All modes and mechanisms of double beta decay were simulated, as were most backgrounds. Further assessment of GEANT311's accuracy was obtained when events of the latter type were compared with the actual data collected in this experiment. The correspondence in cases when signals were quite pure will be noted in the next Section.

Alpha particle backgrounds were not simulated, owing to the poor accuracy with which these events could be modeled. Tiny variations in dead layer thicknesses or departures from hypotheses concerning the distribution of alpha emitters in the films could dramatically effect energy loss calculations. The incomplete charge collection of alpha

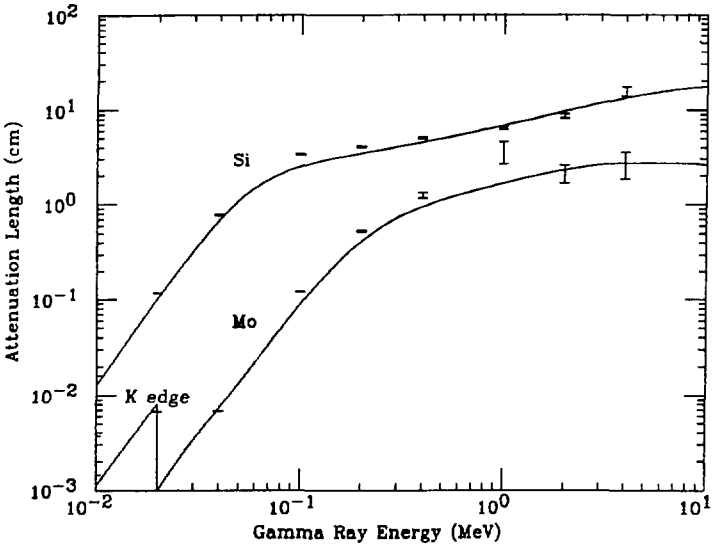

Figure 4.7: **Gamma ray attenuation lengths vs. energy.**
Theoretical expectations (the curves) are taken from [48]. Data points indicate Monte Carlo results.

energy depositions in silicon (mentioned in Section 3.3) was very difficult to model. In the end, the expedient of analytic calculations based on simple assumptions was used.

4.2.2 The Array Model and a First Look at Signals

The detectors were modelled in Monte Carlo calculations as pure silicon disks, with no dead surface layers (metalizations) and no grooves, but they did have dead edges, 3.2 mm wide around their circumferences. Collection of charge carriers liberated in the active volume was assumed to be complete. Films were composed of the appropriate, homogenous mixtures of elements; i.e. the formvar polymer was not treated as a molecule. The array geometry was preserved, but there were no electrical contacts or leads, nor any copper support structures. There existed no gold, infrared reflector, no titanium cryostat, nor any lead, polyethylene or wax shielding. As modeled in the Monte Carlo, then, no radiation escaping the array could bounce back in from surrounding materials, but instead was lost to infinity.

The effects of preliminary processing adjustments (mentioned in Section 4.1.3) were carefully mimicked in the analysis of Monte Carlo simulations. Bad channels were declared dead, a lower level threshold of 110 keV was established, and a ratio cut of 1:20 was imposed on relative energy depositions. Trigger thresholds followed the choices made in analyses of the data.

Double beta decay signatures could be almost completely anticipated from what has already been given, but two further pieces of information were helpful. Any particular decay electron emitted from a film entered the adjacent detector at random angles. Its path within the detector would then be severely limited by scattering. Consequently the normally incident, extrapolated ranges of Figure 4.5 were much larger than the typical depths attained. However, there remained a small probability that, even at the energies involved in ^{100}Mo double beta decay, electrons could emerge from the other side of the detector to encounter the next film.

Secondly, backscattering increased as the incident angle increased. Monte Carlo simulations revealed that this also varied with energy. A 1 MeV electron entering silicon at 60° with respect to the normal backscattered about one third of the time.

Via backscattering from and transmission through detectors, then, a decay electron might navigate more than just the amount of film encountered in its initial exit. On the

average, 1 MeV electrons passed through about twice the thickness of one film. Variations in energy lost to this dead material dominated the resolution of the array. The energy deposited in detectors by each electron in double beta decay spread downward with respect to their initial kinetic energy. Highly asymmetrical energy loss distributions were obtained, reminiscent of Landau-like straggling variations. When the two distributions for each electron were folded together, the combined distribution spread even wider.

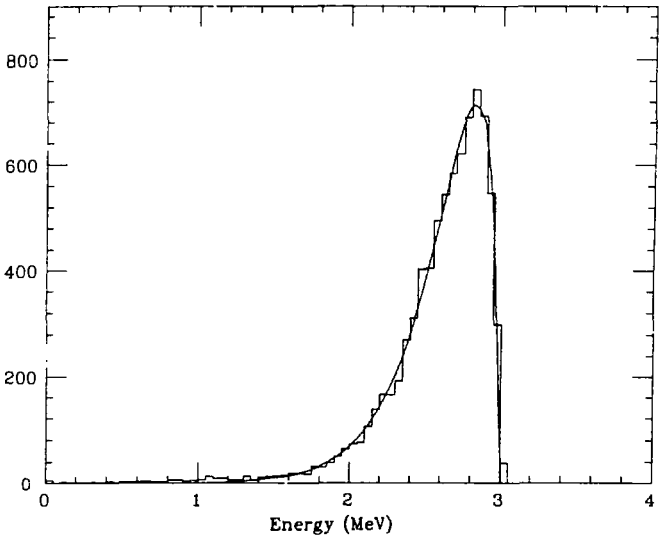

Figure 4.8: **Raw Monte Carlo sum-energy spectrum for neutrinoless $0^+ \rightarrow 0^+$ double beta decay.**

The energy deposited in detectors from $0^+ \rightarrow 0^+$ neutrinoless decay of ^{100}Mo is shown in Figure 4.8. Electronic noise has not been included, but would be of negligible influence anyway. A chi-squared lineshape ($x^{0.94}e^{-x}$, where $x = (3.03 - E)/0.21$ with E the total energy in MeV) fits the spectrum quite well. The full width at half maximum (FWHM) is 490 keV and contains 71.3% of the spectrum. The average energy shift is 448 keV, while the most probable is 214 keV. Geometric parameters reflective of this experiment were fixed, but variations in resolution could be determined by Monte Carlo analysis.

The FWHM was found to depend roughly linearly on film thicknesses and inversely with the square root of detector thicknesses. (The FWHM was reduced by nearly 15% after the imposition of further cuts; see Sections 4.4.1 and 4.4.4.)

As could be surmised from previous analyses, energy was usually deposited in fewer than three detectors in typical double beta decay events. Also, the detectors in two-detector events were likely to be those on either side of the film of origin. One could guess that more two-detector events occurred in decays in which the electrons tended to be emitted back-to-back than otherwise. Backscattering was so severe, however, that no such distinction could be made with any reasonable statistical significance. Scattering dissipated the multiplicity differences expected of various double beta decay modes.

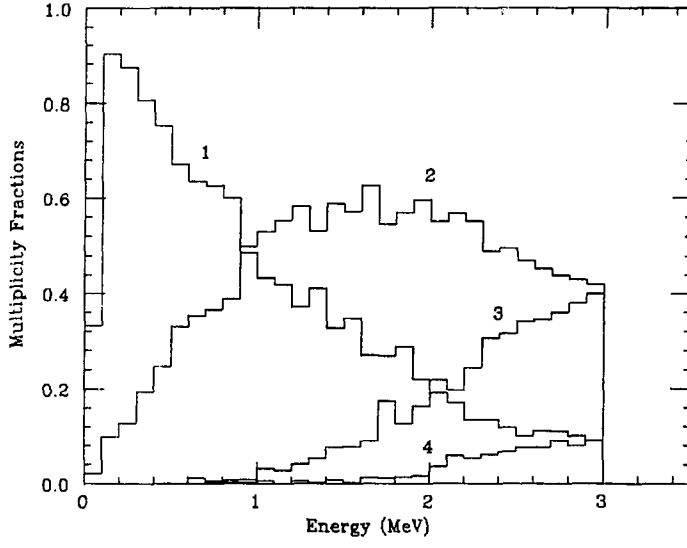

Figure 4.9: **Fractions of events in double beta decay signals.** The number of detectors firing is the parameter. This figure is to be compared with Figure 4.3.

The multiplicity fractions for generic, broad-spectrum double beta decay are shown in Figure 4.9. The abscissa indicates the total recorded energy. A equal sharing of phase

space between the two electrons was assumed. Over ten thousand events were simulated to produce this Figure.

4.3 Analysis of Backgrounds

As evidenced by energy and multiplicity distributions, backgrounds dominated ^{100}Mo data. These had to be understood before double beta decay signals could be assessed with any accuracy. Since backgrounds could arise from many sources, a thorough and systematic study was undertaken. Each data sample was analysed separately; for the array without films and then with blank, ^{96}Mo and ^{100}Mo films inserted. By comparing results, the completeness and precision of background estimates could be appraised.

At the measured cosmic ray flux, muon bremsstrahlung and muon capture and decay in the lead shield must have occurred at negligible rates. Backgrounds were therefore dominated by natural radioactivity in the surrounding materials and in the source films. Barring possible long-lived, cosmogenically induced activity from before the materials were brought underground, these backgrounds were most likely due to inevitable crustal abundances of uranium, thorium and potassium. Fortunately, the topological, energy distribution and timing information provided by the array allowed a relatively accurate measure of these contaminations to be taken.

In the analysis that followed, separate results were sought for radioactivity in the top versus bottom halves of the array. Channels #1-19 were used as vetos for measuring contamination in the upper 20 source films, and in the upper half of the array when there were no films present. Channels #18-40 were vetos when seeking contamination in the blank films installed during series 16. In addition, the extreme channels, #1-3 and #40 were used as vetos regardless of what radioactive signal was sought. Thus were excluded from the data samples events due to charged emanations from radioactivity in the copper end-plates of the support structure. (Since for most of the signals originating in the films, fewer than three adjacent detectors fired, the loss in collection efficiency engendered by these final vetos was minimal.)

4.3.1 Background Signals

The most straightforward background signals that could be sought were spectral peculiarities indicative of certain radiations. Unfortunately, gamma ray interactions in silicon returned largely featureless spectra. For energies of order 1 MeV, photoabsorption and pair production occurred at miniscule rates compared with Compton scattering. Alpha backgrounds, on the other hand, could return sharp edges or even peaks if their full energies were collected. However, alpha spectra were quickly degraded by partial absorption in dead layers, so such signals were also typically of limited informativeness.

Each of the naturally occurring decay chains contain short-lived isotopes with half-lives ranging from less than a microsecond to several minutes (see Figure 4.10). By measuring time intervals between events in the same or adjacent detectors, a particular decay sequence could be identified. The effective abundance of that chain's parent could then be established.

The ^{238}U, ^{232}Th and ^{237}Np chains each contain a Bi beta decay that is rapidly followed by a Po alpha decay. In this experiment, the beta could trigger an event readout, and the alpha might exit the film with enough remaining energy to stop the fast clock, "tagging" the event. For sequences $^{212}\mathrm{Bi} \xrightarrow{\beta} {}^{212}\mathrm{Po}(\tau_{1/2} = 0.3\mu\mathrm{s}) \xrightarrow{\alpha} {}^{208}\mathrm{Pb}$ and $^{213}\mathrm{Bi} \xrightarrow{\beta} {}^{213}\mathrm{Po}(4.2\mu\mathrm{s}) \xrightarrow{\alpha} {}^{209}\mathrm{Pb}$ the alpha could follow so rapidly that the energy it deposited in a detector would add to that deposited by the beta. (Recall that ADC gates were opened for 2 μs, 3 μs after a trigger.) If the beta passed through only one detector, and the alpha entered a detector on the opposite side of the film, then a two-detector event would result. Therefore, the distribution of the number of detectors firing in each event would shift to higher multiplicities. On the other hand, the sequence $^{214}\mathrm{Bi} \xrightarrow{\beta} {}^{214}\mathrm{Po}(164\mu\mathrm{s}) \xrightarrow{\alpha} {}^{210}\mathrm{Pb}$ proceeded too slowly for the alpha energy to have been recorded. Thus, at least three signals identifying the ^{232}Th, ^{238}U and ^{237}Np chains could be distinguished via differing energy, multiplicity and tagging time distributions. (Timing correlations could be extended only as far as was allowed by accidental rates. With $\approx$ 1.1 events per minute occurring in the entire array, the time interval between accidentals in the same, two-detector group averaged $\sim \frac{40}{2} \times 1.1$ minutes.)

Relatively fast, three-alpha decay sequences commence with ^{224}Ra in the ^{232}Th chain, ^{223}Ra in the ^{235}U chain and ^{225}Ac in the ^{237}Np chain. Alpha emitter half-lives decrease,

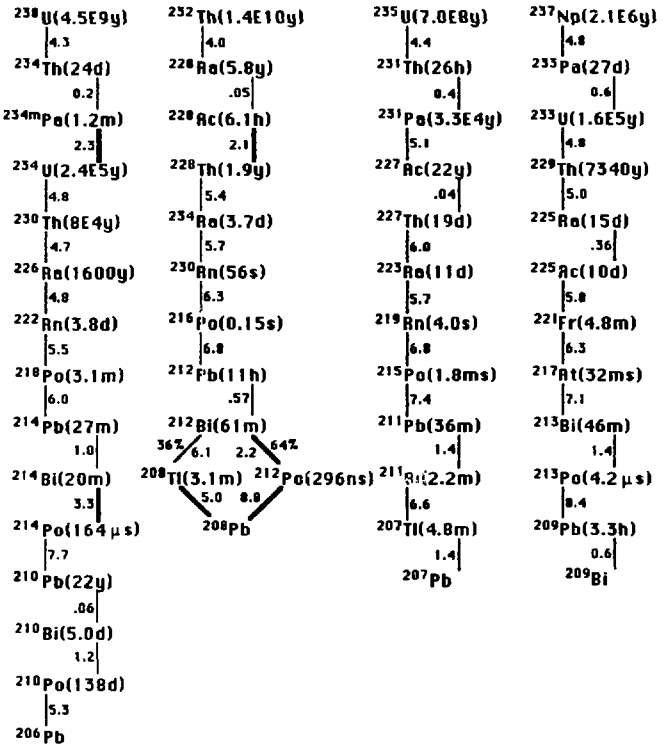

Figure 4.10: **Naturally occurring radioactive decay chains.**

Half-lives are given in parentheses. Left-justified vertical lines indicate alpha decays, while right-justified lines tell of beta decays. The available transition energies are noted beside these lines. Heavy lines denote major backgrounds to double beta decay.

while emission energies increase as the sequences proceed. Therefore, time interval measurements between high-energy single-detector events could also reveal contamination levels. Signals differed, depending upon which alphas escaped the films. For example, if the first alpha – say from ^{224}Ra decay – was observed, a two-alpha sequence would result if $\sim$ 1 minute later only one of the ^{220}Rn or ^{216}Po decays was also observed. Owing to the long and similar half-lives of ^{220}Rn and ^{221}Fr, however, such two-alpha signals would be hard to distinguish not only from each other, but from accidentals and the sequence ^{222}Rn $\xrightarrow{\alpha}$ ^{218}Po(3.05min) $\xrightarrow{\alpha}$ ^{214}Pb in the ^{238}U chain.

An independent two-alpha signal could result if both the second and third alphas escaped a film (the first alpha being disregarded). Time intervals for the sequences, ^{220}Rn $\xrightarrow{\alpha}$ ^{216}Po(0.15sec) $\xrightarrow{\alpha}$ ^{212}Pb, ^{221}Fr $\xrightarrow{\alpha}$ ^{217}At(32ms) $\xrightarrow{\alpha}$ ^{213}Bi and ^{219}Rn $\xrightarrow{\alpha}$ ^{215}Po(1.8ms) $\xrightarrow{\alpha}$ ^{211}Pb differed sufficiently to allow them to be separately discerned.

If all three alphas exited a film with energies over trigger thresholds, then another signal would be observed, not necessarily independent of the two above. Only the sequences ^{224}Ra $\xrightarrow{\alpha}$ ^{220}Rn(56sec) $\xrightarrow{\alpha}$ ^{216}Po(0.15sec) $\xrightarrow{\alpha}$ ^{212}Pb in the ^{232}Th chain and ^{223}Ra $\xrightarrow{\alpha}$ ^{219}Rn(4sec) $\xrightarrow{\alpha}$ ^{215}Po(1.8ms) $\xrightarrow{\alpha}$ ^{211}Pb in the ^{235}U chain could be distinguished in this way. In the former, all three alphas could be emitted sufficiently far enough apart in time that they were recorded as three separate events. Otherwise, if the third alpha was emitted before the event readout for the second alpha was completed, then it simply tagged the second event. This last case constituted an independent measure of the ^{232}Th and ^{235}U chains.

In all, 14 different decay sequence signals were sought, 12 of which were independent (see Appendix B for details). Decay chain contaminations were measured redundantly, aiding in the assessment of systematic errors.

Betas and Alphas

Owing to the importance attached to these background measurements, a somewhat detailed discussion of how beta and alpha decays were handled is in order. To begin with, contaminants were assumed to be uniformly distributed in the films. This was of little consequence for signals arising from beta decays. For alpha decays, however, deviations from this assumption could dramatically affect spectral shapes and collection efficiencies.

At least some of the time, all the beta decays of interest proceeded via excited states

of their daughter nuclei. Several gamma rays could have been emitted, nearly simultaneously with the beta. To model these deexcitations, energy level diagrams for daughter nuclei had to be installed in the Monte Carlo.[49] The completeness and precision with which this was done depended on the ultimate numbers of events the uranium and thorium chains contributed to ^{100}Mo data. Levels for which the beta decay branching fractions were less than 1% were grouped together with nearby levels. Subsequent deexcitation branching fractions were ignored if less than 1%.

To get corresponding collection efficiencies, 10000 simulated beta decays for each emitter were analyzed. Monte Carlo events (and the actual data) had to survive the preliminary processing mentioned in Section 4.1.3 and the vetos, in addition to a few other cuts. For ^{214}Bi betas, an off-line trigger threshold of 500 keV was applied, helping to make every detector appear to operate with the same characteristics. For ^{212}Bi and ^{213}Bi betas no off-line trigger threshold was applied to real data, but one of 315 keV was imposed on the simulations. This allowed the alpha energies to add to each event, but increased collection efficiency uncertainties because the hardware (discriminator) thresholds peculiar to each channel were not taken into account. To avoid false tags due to echos (double-pulsing) some extra channels were used as vetos when fast-clock times were less than 20 μs. (An alternative event scenario could proceed in the ^{212}Bi and ^{213}Bi sequences: the beta might not trigger a readout but while its deposited energy remained above online software thresholds – on the falling tail of its signal pulse – the alpha would exit the film and trigger. But then no fast clock time would be recorded, unless double-pulsing occurred.)

Alpha decays were recorded either as large-energy depositions in single detectors or as tagging events which stopped the fast clock before readouts of previous events had finished. In order to distinguish alpha decays from others, an off-line trigger threshold of 2 MeV was imposed on one-detector events. When alpha decays tagged other events, no off-line threshold could be imposed. Alphas then had to exit the films within certain time windows and with more than 315 keV in energy (the hardware discriminator level). Therefore, range-energy information was needed. By using Bragg's additivity rule, alpha ranges in the source films could be calculated, with the results shown in Figure 4.11.[50]

Film thicknesses of 34 mg/cm^2 would stop the most energetic alpha (of 8.78 MeV from ^{212}Po decay). In fact, two alphas of any particular decay sequence would be completely

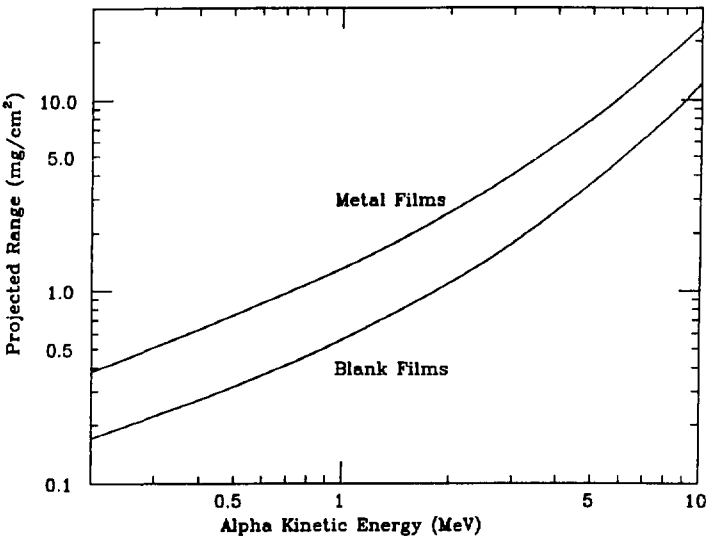

Figure 4.11: **Alpha ranges in the films.**

Due to slight differences in composition, alpha ranges in the ^{96}Mo films were 98% of those in ^{100}Mo films.

absorbed if emitted from the center of a film, even if emitted in opposite directions. Hence, collection efficiencies were calculated assuming all alphas of any sequence exited the same (metal) film face (see Appendix A). Also, time intervals were accumulated for every channel separately; i.e. the time between events in one particular channel was undisturbed by events in other channels. Finally, if contamination was evenly distributed among the films, then collection efficiencies had to be scaled by the fraction of "live faces" of films observed. Thus, even though to 20 films there were 40 surfaces, due to the use of detector #19 as a veto, the existence of bad channels and of channels not in the trigger, in series 13 and 16 there were only 39, in series 14 only 37, in series 17K only 35 (for the first 1973.64 hours, due to the loss of one timing/trigger channel afterward) and in the rest of series 17 only 33 film faces observed by detectors which were sensitive to alpha triggers.

Checks

For every background signal observed, certain factors were checked...

- Since a few decay sequences involved similar half-lives and energies, separate contributions to some signals from the different chains were ambiguously determined. Consistency checks among the various signals were performed to insure accuracy.

- The number of "extra" events in the data samples from accidentals or from other signals had to be estimated. This was accomplished empirically by noting the numbers, and time distributions of events in adjacent time windows; i.e. at times short and long with respect to the half-lives of the sought-for decay sequences.

- An effort was made to discern contributions from other sources which could mask the sought-after background signals.

- The appropriate exponential decay half-life had to describe the time interval distribution.

- The expected energy spectrum had to be found.

- The detector multiplicity distribution had to reproduce that expected from Monte Carlo analysis for signals involving beta decays.

- The frequencies with which each channel was involved in the data samples should have been appropriately (e.g. randomly) distributed among the non-vetoed channels if contaminants were evenly distributed throughout the array/films.

- The rates of signals per day in each run and between runs should have been uniform, otherwise some other contaminant existed which was slowly being removed from the array via decay or purging.

4.3.2 Results

As noted above, 14 background signals were sought in each of the four data samples. Beside statistical uncertainties due to the finite number of background events observed, there were many possible sources of systematic error. These had to be examined before decay chain contamination levels were calculated.

Detailed information on background cuts, collection efficiencies and numbers of events observed can be found in Appendix B (see in particular Table 4). In the following report of that study, more general results are presented. The most important issues addressed include; which signals were trustworthy, what evidence could be found in support of the assumptions made concerning the physical nature and sites of contamination, how were uncertainties assessed, and what further backgrounds could exist but were not discernable with the methods employed.

Empty-Running Results

Silicon of 2 kΩcm resistivity contains impurities at concentrations of $\approx 7 \times 10^{12}$ cm^{-3}. If these impurities were contaminated with typical crustal abundances of uranium and thorium ($\sim 10^{-6}$ to 10^{-5} by weight) then in this experiment one would not expect a single case of ^{238}U, ^{235}U or ^{232}Th decay to have occurred in the active regions of the detector array. Therefore, the backgrounds observed when the array was empty of source films must have come from contaminants on detector surfaces or in contacts, electrical leads, support structures and shielding.

The high-energy, one-detector event rates for channels #34 and #35 in series 13 were roughly five times above those for other channels. An edge at 5.8 MeV in the spectrum for channel #35 (see Figure 4.12) pointed to the presence of ^{244}Cm. This

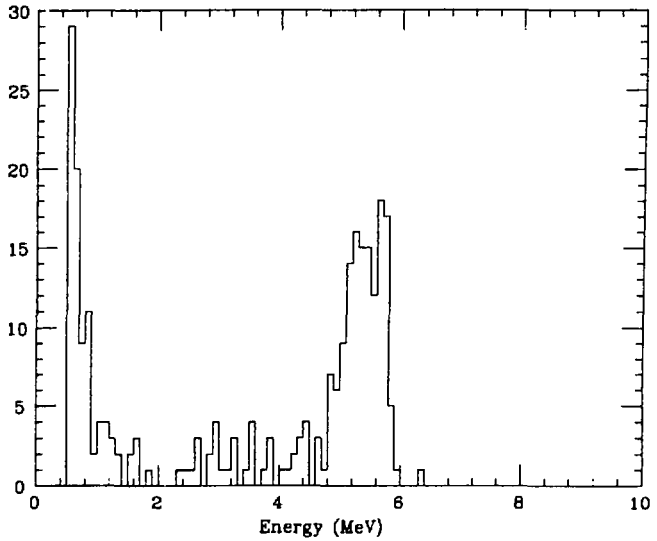

Figure 4.12: **One-detector spectrum for channel #35 in series 13.**

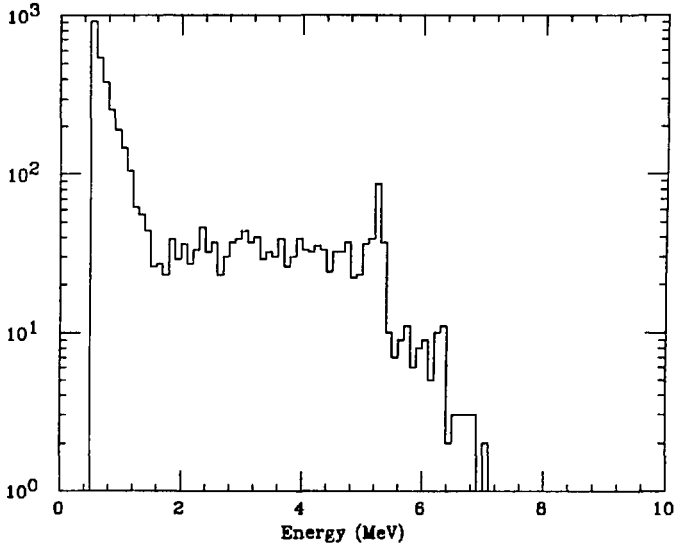

Figure 4.13: **One-detector spectrum for channels other than #34 and 35 in series 13.**

alpha emitter was used to test detectors during manufacture, and a microscopic amount of the "swipable" source might have been deposited on the ohmic surface of detector #35. If so, the width of this spectrum was indicative of alpha-liberated charge carrier losses due to recombination effects. (The metal plated on that surface would not lead to such full widths, since a 5.8 MeV alpha loses only $\approx$ 9 keV in passing though a 40 $\mu g/cm^{-2}$ thickness of gold.)

The one-detector spectrum for all other channels (shown in Figure 4.13) was much different. An edge/peak at 5.3 MeV indicated alphas from ^{210}Po decay, at the end of the ^{238}U decay chain. Since no other edges of similar size appeared, this chain must have been broken. The most likely source for ^{210}Po was a supply of ^{210}Pb: the rest of the ^{238}U chain having been selectively removed via some earlier, and unknown chemical processing. (^{210}Pb has a half-life of 22 years and is present in nearly all forms of lead, including solder.) The spectral flatness, continuing through lower energies, may have resulted if this source was distributed inside some absorbing material(s) like the mylar or gold foils in detector contacts.

When one-detector events were eliminated the spectrum of Figure 4.14 remained. (A few other cuts were imposed which made a small difference, see Section 4.4.1.) There were no counts above 2.5 MeV. The highest-energy region is shaped like a Compton edge, which might have been due to ^{208}Tl. This isotope, at the bottom of the ^{232}Th chain, emits a 2.614 MeV gamma ray with every decay. The lack of strong evidence for thorium-chain alphas during Empty running implied the source of this contamination was outside the array. A simple calculation revealed that $\sim$ 0.1 ppb of ^{232}Th by weight in the lead shield could have contributed these gammas. This level of contamination is consistent with that determined by other means at the LBL Low Background Counting Facility.

The remaining higher-energy spectrum could be fitted with Compton scattering energy depositions from incoming ^{214}Bi gamma rays. This isotope emits all of the most penetrating gamma rays in the ^{238}U decay chain. Only $\sim$ 0.2 ppb of uranium by weight in the lead would produce the necessary gamma ray flux.

Combined ^{214}Bi and ^{208}Tl contributions fit the spectrum above $\approx$ 1.4 MeV quite well. Contributions below this cut-off turned out to be of lesser concern (see Section 4.4.1). Nevertheless, much of the lower-energy data could be attributed to the remaining

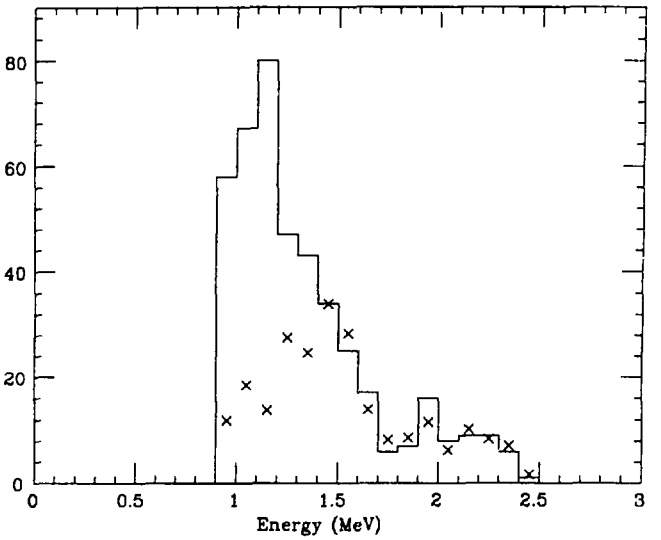

Figure 4.14: **Multi-detector spectrum for empty running.**
Data from the lower region of the array was excluded. A fit of contributions from ^{214}Bi and ^{208}Tl gamma rays is superimposed (crosses).

thorium and uranium chain gamma rays. A few ^{40}K decays were all that was needed to supply the final Compton edge at 1.2 MeV.

The data presented above came from the upper detectors of the array, where there were no bad channels. Multi-detector event rates in this region were more or less uniform within statistics. In contrast, rates among the bottom detectors varied by as much as a factor of four. Attempts were made to determine the cause(s), but spectral and other analyses were inconclusive.

To estimate collection efficiencies for signals from decay sequences, contaminants could be imagined as being distributed in absorbing layers (say, as thin as the blank films) placed between detectors. Results confirmed the nonexistence of decay chain parents within the array (on or near the detectors). Fewer than ≈ 1 decay per day of ^{232}Th near the detector surfaces was allowed by the best alpha-sequence signal rates. This was ≈ 50 times lower than that needed to account for the ^{208}Tl Compton edge.

Source Film Results

In general, one-detector spectra appeared like Figure 4.13: flat from ~ 2 Mev to an edge at 5.3 MeV, followed by residual, higher-energy alpha signals. By noting the increased alpha rates above those encountered in series 13, ^{210}Pb contaminations of $\approx 4.1 \times 10^{-16}$ in the ^{100}Mo films, $\approx 1.7 \times 10^{-16}$ in ^{96}Mo films and $\approx 2.5 \times 10^{-16}$ in blank films (all by weight) could be estimated.

Multi-detector event rates involving channels #18 and 19 in series 14 were ≈ 4 times higher than those from channels above #19. This was traced to ~ 20 ppb by weight of ^{40}K in the film above detector #18. (That film was the very first one fabricated, which would imply that cleanliness had not yet been assured in the manufacturing process.) By designating channels #18 and 19 as vetos, nearly all backgrounds due to ^{40}K beta decay from that film could be removed. Gamma ray backgrounds from the 1460 keV transition in ^{40}K electron capture contributed negligibly to event rates in the rest of the array.

Low energy gamma rays would interact close to their points of emission, while at higher energies, gamma rays tended to escape the array. Therefore, the presence of other films had little effect on event rates in channels #20-39. During series 14-17 the same set of ^{100}Mo films were installed between detectors #19-39, and so data from these

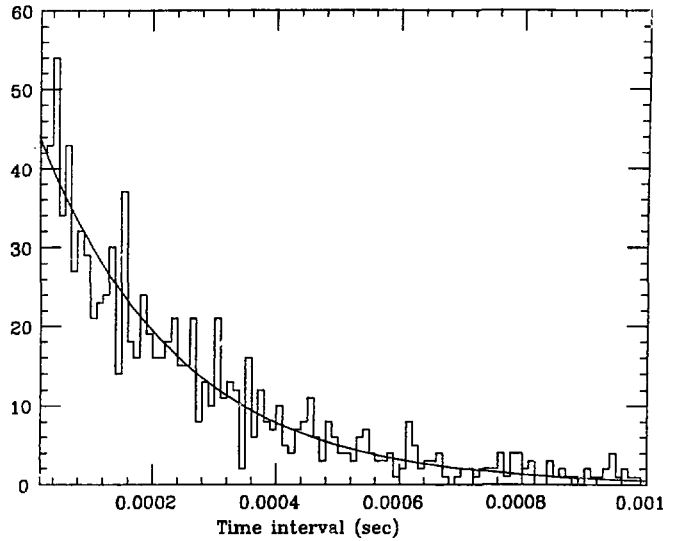

Figure 4.15: **^{214}Bi time intervals in ^{100}Mo data.**

The best-fit exponential corresponds to a half-life of 153.5 ± 6.7 μs.

channels could be treated as a whole.

Tagged ^{214}Bi signals were quite pure; i.e very few accidentally tagged events were recorded. In all but one aspect, data agreed with expectations. Timing and energy distributions for the ^{100}Mo sample are shown in Figures 4.15 and 4.16 respectively. There were $\approx$ 163 c'scontiguous events in that sample, or $\approx (16.8 \pm 1.4)\%$ with respect to the rest of the ^{214}Bi events, compared with Monte Carlo expectations of $(15.2 \pm 0.7)\%$.

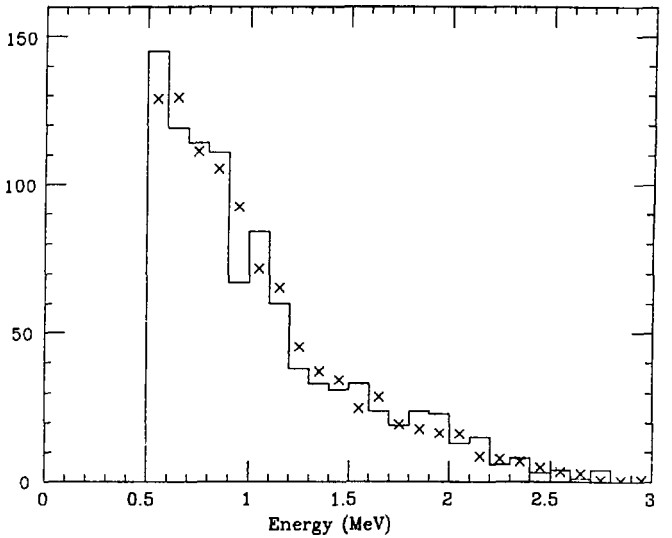

Figure 4.16: **^{214}Bi energy spectrum for ^{100}Mo films.**
The spectrum from tagged events in the ^{100}Mo data sample (solid line) is compared with a Monte Carlo simulation (crosses) containing the same number of events.

Multiplicities, however, were significantly, and systematically high for ^{214}Bi signals throughout all data samples. The average number of detectors firing in tagged events from the ^{100}Mo films was 1.33 ± 0.06, compared to Monte Carlo expectations of 1.26 ± 0.03. This discrepancy persisted for events with energies above 1.5 MeV (albeit with reduced statistical significance) and so could not have resulted from errors in the low-energy calibration or thresholds.

This became one of the few possible indications of inaccuracy in the Monte Carlo. Calculated multiple scattering angles and/or dE/dx for electrons in the films may have been over-estimated. Errors might have resulted if the fractions of elements in the formvar were not as reported by the manufacturer. (The root-mean-square scattering angle for a 1 MeV electron traversing 40 mg/cm^2 of molybdenum is calculated to be $\sim 40°$. Scattering in composite materials - incorporating hydrogen, carbon and oxygen - was more difficult to calculate. In simulated events, too many electrons may have backscattered from the films, rather than passing through to reach detectors on the other side, shifting the expected average multiplicity downward.) Since Formvar mixtures could vary unpredictably, little effort was expended attempting to determine the precise composition of our samples.

Fortunately, completely accurate contamination estimates were not required. Since one-detector events were to be cut when the search finally began for double beta decay, the multi-detector signals were taken as representative. (The weighted mean of tagged one-detector and multi-detector signals may have reflected ^{214}Bi decay rates more precisely.) Multi-detector ^{214}Bi decay rates may have been over-estimated, but this was balanced by the under-estimation of ^{214}Bi contributions to untagged multi-detector backgrounds.

Further inaccuracies in Monte Carlo results were possible, despite how well the dE/dx, electron range, backscattering, etc. agreed with expectations. The geometry and composition of detectors, films and other inert materials (support structures and shields) could have been incorrectly modeled; e.g. the nylon rings may have been contaminated. Branching fractions of the energy level decay schemes used might not be totally accurate. Also, since the number of simulated events could not be infinite, statistical errors in GEANT311 results were unavoidable. In general, the direction of these errors could not be determined; signal collection efficiencies may have been either suppressed or enhanced.

Thorium chain signals (i.e. decay rates) in the ^{100}Mo data sample were not consistent within statistical uncertainties (see Appendix B, Table 4). Large errors could have resulted from poorly modeled alpha emissions. Straight trajectories (no scattering) were assumed, and projected range estimates may have been inaccurate. More importantly, it might have been incorrect to model contaminants as though uniformly distributed in

homogenous films, and the collection of alpha-liberated charge carriers in the detectors may have been less than unity. These faults could affect alpha collection efficiencies in different ways. By noting variations in signal rates, charge-collection losses were found to dominate, but with an unconvincing statistical significance. (Thorium decay rates indicated by the observation of all three alphas in the triplet-alpha sequence were lower than those calculated from observing any two alphas. The incomplete collection of charge carriers due to recombination had already been implicated; see Figures 4.12 and 4.13 and the associated discussion.)

By neglecting those signals which were "dirty" (i.e. likely to include many accidental events, or decay sequences from other chains – leaving those signals starred in Appendix B, Table 4) the thorium chain results fell into much better agreement. Therefore, the weighted mean of these signals were taken as representative. However, tagged ^{212}Bi signals from the ^{100}Mo films indicated lower ^{232}Th decay rates than did signals from the triplet-alpha sequence. This may have been due to the same cause that led to the disagreement between one-detector and multi-detector ^{214}Bi results.

Evidence was found for the presence of ^{235}U and ^{237}Np contamination in the ^{100}Mo and ^{96}Mo films. Signals were dirtier and rates were lower than those from the ^{238}U and ^{232}Th chains. Since by use of cuts (especially on energy) ^{235}U and ^{237}Np background contributions were to be avoided anyway, minimal effort was put into assessing contamination levels.

For the most part, the magnitudes of systematic errors could only be guessed. In general, if alpha collection efficiencies were over-estimated (as suggested by thorium-chain triplet-alpha results) then calculated contamination levels were suppressed, and large upward corrections should be entertained. On the other hand, it was still possible that background source rates could have been over-estimated if, say, the ^{214}Bi multiplicity discrepancies resulted from other, more subtle mechanisms. Rough estimates of the sizes of these systematic errors were obtained by noting the variations in triplet-alpha signal rates compared with those involving beta decays.

Table 4.3 summarizes results for the four data samples. For ^{214}Bi (qua ^{238}U) and ^{232}Th decay rates in the ^{100}Mo and ^{96}Mo films, systematic errors are listed last. All statistical uncertainties reflect the limited number of background signal events observed.

If blank-film decay rates were subtracted from those of the ^{100}Mo films, contamination

Sample	^{238}U	^{232}Th	^{235}U	^{237}Np
# decays per day				
Empty	< 0.6	< 1	< 1	< 1
Blank	2.4 ± 0.9	4.2 ± 1.1	0.33 ± 0.29	0.51 ± 0.28
^{96}Mo	$120.3 \pm 9.1 \pm^{23.}_{15.}$	$12.1 \pm 2.5 \pm^{2.3}_{1.5}$	2.6 ± 0.9	6.0 ± 2.3
^{100}Mo	$85.3 \pm 5.1 \pm^{6.3}_{2.3}$	$37.8 \pm 3.1 \pm^{2.8}_{1.0}$	14.4 ± 1.3	17.4 ± 2.4
contamination levels (by weight of film)				
Blank	1.1 ± 0.4 ppb	6.0 ± 1.6 ppb	24 ± 21 ppt	0.11 ± 0.06 ppt
^{96}Mo	$6.12 \pm^{1.26}_{0.89}$ ppb	$1.89 \pm^{0.53}_{0.46}$ ppb	21 ± 7 ppt	0.15 ± 0.06 ppt
^{100}Mo	$4.08 \pm^{0.39}_{0.24}$ ppb	$5.57 \pm^{0.62}_{0.46}$ ppb	107 ± 10 ppt	0.40 ± 0.05 ppt

Table 4.3: **Background source rates and consequent contamination levels.** The indicated contamination levels were calculated assuming each decay chain was in equilibrium.

levels in the ^{100}Mo metal itself of $4.6 \pm^{0.5}_{0.3}$ ppb ^{238}U, $5.5 \pm^{0.8}_{0.6}$ ppb ^{232}Th, 122 ± 12 ppt ^{235}U and 0.5 ± 0.1 ppt ^{237}Np by weight would be implied. (Recall Oak Ridge's measurements were 3.2 ± 1.0 ppb ^{238}U and 6 ± 3 ppb ^{232}Th.)

4.4 Data Reduction

Having assessed many backgrounds, one could then estimate double beta decay half-life limits and/or make half-life measurements. The basic procedure was to (1) establish cuts, (2) subtract the known backgrounds from ^{100}Mo data and (3) scrutinize what was left for any remaining backgrounds and attribute these, along with double beta decay signals, to the residual data. For broad-spectrum double beta decay - the two-neutrino and Majoron modes - a least-squares fit of spectral shapes could be used to reveal signal contributions. For the neutrinoless decay mode (in either $0^+ \rightarrow 0^+$ or $0^+ \rightarrow 2^+$ transitions) a single-bin analysis would suffice.

4.4.1 Cuts

The purpose of cuts was two-fold; to increase the double beta decay "signal to noise" ratio and to reduce errors. There were two ways in which uncertainties in residuals spectra of the ^{100}Mo data could be avoided. Large background contributions may be rejected, reducing statistical errors. Lesser contributions from sources with inadequately known signals or which were of poorly determined strength could be eliminated, thus removing systematic errors. At the same time, however, collection efficiencies for various double beta decay signals should not be too severely affected. A set of cuts meeting these criteria were devised. These cuts were not necessarily "optimized" in any way, but thoroughly eliminated many known backgrounds, leaving others which could be accurately estimated and/or simulated.

Clearly, all one-detector events had to be rejected, eliminating most of the alpha backgrounds at a small cost to double beta decay collection efficiencies. There remained possible alpha+gamma contributions, mostly from the ^{235}U chain, in which alpha decays to excited states of daughter nuclei were quickly followed by deexcitation gamma ray emissions of up to 400 keV in energy. By requiring at least 400 keV depositions in each channel of two-detector events, all these decays could be removed.

Working above 1.4 MeV total energy allowed one to neglect all contributions from ^{40}K, ^{237}Np and any surviving ^{235}U chain decays. The remaining, known higher-energy backgrounds included decays of ^{234m}Pa and ^{214}Bi from the ^{238}U chain and ^{228}Ac, ^{212}Bi and ^{208}Tl from the ^{232}Th chain.

Residuals spectra could be further reduced with no loss to the collection efficiencies of interest by rejecting those types of events, regardless of origin, which would never – or rarely – occur in double beta decay. These cuts were either anticipated, given certain knowledge of decay chain backgrounds, or discovered through systematic examinations of the data. Thus, tagged events were excised to avoid fast decay sequences. (Cuts to avoid correlations in time intervals longer than those needed for readouts were both unnecessary and would have adversely affected live times.) Discontiguous events, indicative of gamma ray contributions, could be rejected. To remove some backgrounds from gamma rays which interacted close to their origins of emission, more than 400 keV was required in the middle channels of three-detector events, and events involving four or more detectors

Cuts	1.4-2.5 MeV		2.5-3.0 MeV	
	# events	$\epsilon_{2\nu}$(%)	# events	$\epsilon_{0\nu}$(%)
(1) Preliminary (dead bad channels, threshold of 110 keV, 1:20 ratio on 2-det. events) plus; a trigger threshold of 500 keV, making vetos of channels #1-19 and 40	19118	14.5	5932	58.8
Plus				
(2) Rejecting one-detector events	4067	8.8	163	49.9
Plus				
(3) Requiring contiguity, > 400 keV in each channel of 2-det. events and > 400 keV in middle channels of 3-det. untagged events	3050	8.7	50	47.1

Table 4.4: **Effects of cuts on ^{100}Mo data.**

The number of events remaining in each energy window and the collection efficiencies for two double beta decay signals are given for successive sets of cuts.

were simply eliminated. (Energy depositions from minimum ionizing particles, inclusive of straggling variations, could never be less than 400 keV.)

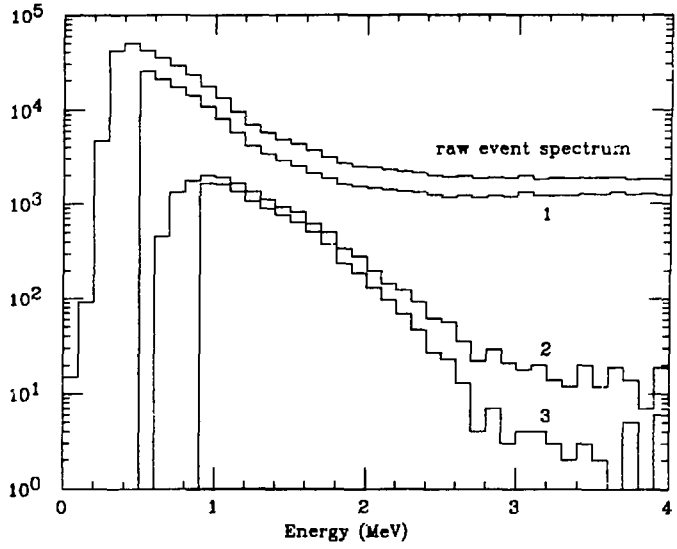

Figure 4.17: **Effects of cuts on ^{100}Mo data.**

The number of events per 100 keV are plotted. Spectra indicate the effects of successive sets of cuts, as listed in Table 4.4.

Table 4.4 serves to recap all the cuts made up to this point and their effects on ^{100}Mo data (see also Figure 4.17). Representative collection efficiencies for two-neutrino and neutrinoless double beta decay (and for the array as it appeared in series 16; i.e. without any bad channels in the upper section of the array) are also given. Collection efficiencies dropped mostly in response to how little phase space was available in the roughly appropriate energy windows. To assess their efficacy, one might compare the "signal to noise" ratio, $\frac{\epsilon}{\sqrt{N}}$ (where N is the number of events remaining) after successive sets of cuts. This figure of merit should not be allowed to fall.

For the broad-spectrum double beta decay modes, these cuts were nearly as strenuous as could be allowed, before signal losses began out-pacing background reductions.

However, the search for neutrinoless decay was found to benefit from further, or modified restrictions on acceptable data. For example, in the case of $0^+ \rightarrow 2^+$ transitions discontiguous events could be selected, rather than eliminated. The introduction and justification of other augmentations and/or modifications of cuts will be postponed until data reductions specific to these neutrinoless modes are described.

4.4.2 Treatment of Backgrounds

Broadly considered, backgrounds could be separated into two classes; those present when the array was empty, and those brought in with the source films. Ideally, both classes could be accounted for in a completely empirical way by observing a set of "dummy" films which were just as thick (in mg/cm^2) and similarly contaminated as the ^{100}Mo films. Unfortunately, the ^{96}Mo films contained differing amounts of contaminants.

The two classes had therefore to be treated separately. For uranium and thorium chain backgrounds in the ^{100}Mo films, Monte Carlo simulations could provide the necessary spectra. Simulated events would be subjected to the same cuts as real data, and generated in such numbers as was indicated by the results of Section 4.3.

Remaining backgrounds could not be addressed quite so straightforwardly. There were three ways to treat these. To start with, events in the Empty data sample might be adjusted - "by hand" - in number, energy, etc. to account for changes incurred due to the presence of films. (Monte Carlo investigations could be undertaken to estimate the magnitudes of these adjustments.) Alternatively, the presumed origins of EMPTY data could be mimicked and Monte Carlo spectra generated which simulated the influences of films. Finally, since the ^{96}Mo data sample incorporated these changes as a matter of course, equivalent non-film backgrounds could be recovered after uranium and thorium chain spectra intrinsic to the ^{96}Mo films were subtracted. To insure accuracy all methods were investigated and an assessment was made of their relative merits.

Contributions of the ^{232}Th Decay Chain from within the Films

The thorium chain was assumed to be equilibrated. This was quite reasonable since the molybdenum isotopes used were separated sometime in the late 1960's and had not been employed in any other experiment. The longest half-life in that chain (besides that for ^{232}Th itself) is 5.77 years for ^{228}Ra. No chemical processing in the intervening years

could have altered the relative isotopic abundances.

The ^{232}Th chain contributions, after cuts, were as follows:

^{228}Ac: Without restriction.

^{212}Bi: At branching fraction 0.64, but also

- Without any ^{212}Po alpha contribution, if the alpha did not exit the film (at probability 0.7158 for ^{100}Mo films, 0.7044 for ^{96}Mo films).
- With less than 315 keV of alpha energy included, if the alpha exited the film with not enough energy to stop the fast clock (at probability 0.0078 for ^{100}Mo films, 0.0192 for ^{96}Mo films). Note, there was no spectral simulation available for this case, but since the expected spectrum was not greatly different from that of the case above, these two backgrounds were lumped together.
- With more than 315 keV in alpha energy, if ^{212}Po decayed before the fast clock was sensitive ($\approx$ 100 ns) or if it decayed during readout when the fast clock was only $\sim$ 50% efficient (between 100 ns and 200 ns) - this case the spectrum of tagged ^{212}Bi events was used, scaled by the rel. probability that ^{212}Po decayed within the time windows mentioned ($\approx$ 0.46)

^{208}Tl: At branching fraction 0.36.

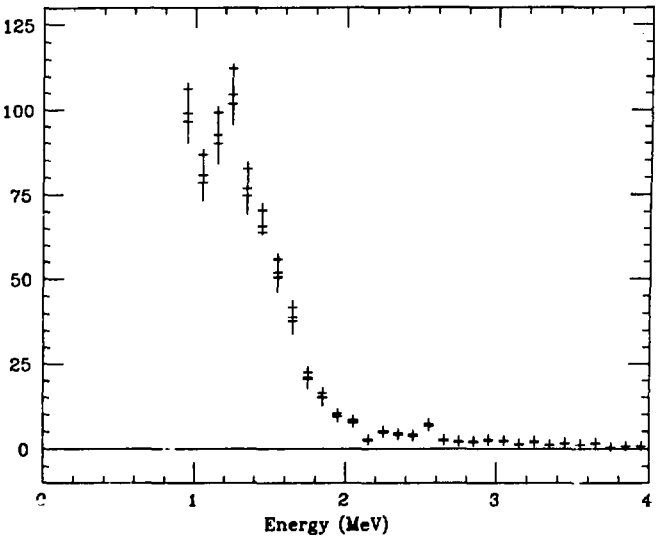

Figure 4.18: **Monte Carlo thorium background in the ^{100}Mo data.** Vertical error bars indicate statistical uncertainties. Horizontal bars denote systematically low, central, and systematically high contamination levels, as given in Table 4.3.

Contributions of the ^{238}U Decay Chain from within the Films

Between ^{234m}Pa and ^{214}Bi in the ^{238}U decay chain there are many long lived isotopes and, if this chain was broken, these beta emitters could contribute at quite different rates. Arguments concerning this assumption follow.

- Since the only identifiable background signal observable from that chain was tagged ^{214}Bi decay, there was no evidence – originating in this experiment – supporting equilibration. The contribution of ^{234m}Pa was undetermined.

- Any argument supporting equilibration was circumstantial at best, but – as was shown when fits to residual spectra were attempted – there was positive evidence against equilibration.

- The ^{238}U chain could easily become, and remain broken for many years via chemical processing. It could also have been present in a broken state from a time just after the molybdenum sample was separated. (Oak Ridge is, after all, a laboratory where large scale separations of uranium have taken place. Uranium, as well as thorium contaminants may have been introduced through normal handling or deposition from airborne radon.)

- An earlier, more heavily contaminated ^{100}Mo sample loaned to this experiment by Oak Ridge contained the ^{238}U chain in a clearly broken state. (There was a deficit of ^{238}U compared with ^{234}U as determined by the sizes of alpha edges.)

- Oak Ridge's "uranium" measurement for the current sample was obtained by fission-track counting, which is specific to ^{235}U, not ^{238}U. The normal isotopic abundances of 0.72% ^{235}U to 99.275% ^{238}U were then assumed, to calculate the uranium content. From the signals observed in this experiment, however, these two isotopes were not present in the expected ratio.

Therefore, ^{238}U chain contributions, after cuts, where treated as follows:

^{234m}Pa: Allowed to float in the fits; i.e. not yet subtracted.

^{214}Bi: Restricted to those occasions in which the ^{214}Po alpha did not exit with enough energy to tag the event (at probability 0.7811 for ^{100}Mo films, 0.7724 for ^{96}Mo

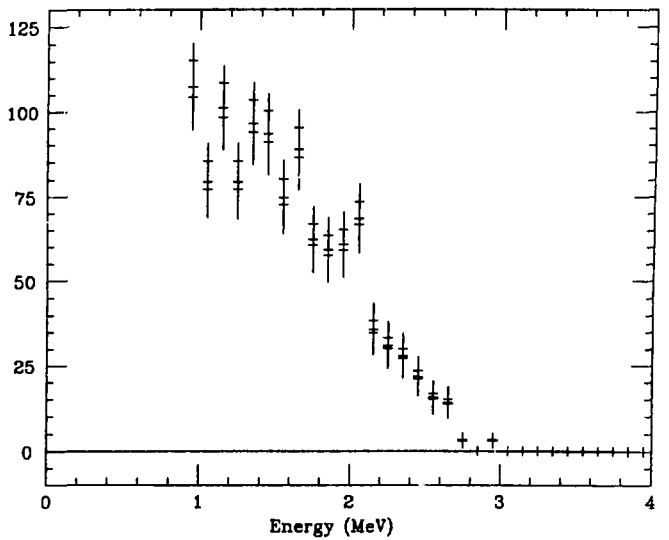

Figure 4.19: **Monte Carlo ^{214}Bi background in the ^{100}Mo data.** Vertical error bars indicate statistical uncertainties. Horizontal bars denote systematically low, central, and systematically high contamination levels, as given in Table 4.3.

films). Since only multi-detector events were to be accepted, the number of ^{214}Bi decays occurring throughout any series of runs was estimated using multi-detector ^{214}Bi signals.

Monte Carlo (GEANT311) simulations were used to give most background spectra. In doing so, all contaminants in the films were presumed to be inside the metal plus formvar mixture, while the nylon rings were assumed to be clean. The results for thorium are shown in Figure 4.18 and those for ^{214}Bi in Figure 4.19. Also shown are the ranges allowed by the uncertainties of Table 4.3. Statistical errors were determined by adding, in quadrature, the allowed bin by bin Monte Carlo statistical variations with counting uncertainties in background analyses. Systematic errors simply reflected the systematic variations noted in Table 4.3.

Non-Film Background Contributions

Three methods were used to estimate background contributions from outside the films. In the first, Empty data was adjusted to represent remaining backgrounds in the ^{100}Mo data sample by employing various scaling and shifting factors...

1. Scaling by relative live time (5597.10 hr/ 883.53 hr).
2. Scaling by 1.1 to account for an additional 10% radiation-length's worth of material represented by the films.
3. Scaling to account for the collection efficiency differences incurred by the presence of bad channels and shifts in event multiplicities.
4. Shifting in energy to account for losses to films.

To obtain these factors Monte Carlo simulations were run in which monoenergetic electrons were generated randomly in position and direction within the array, with and without the films inserted. This replicated the effects of the presumed origin of Empty data, the Compton scattering of incoming gamma rays.

The third scaling factor was found to vary with energy. This was understood to mirror changes in average event multiplicities caused by scattering and energy losses in films. Some two-detector events - especially ones with low energies - became one-detector events and so were cut. A linear relationship between ^{100}Mo and Empty data collection

efficiencies ($0.210 \times (E/MeV) + 0.345$ for deposited energies over 1 MeV) described this effect well.

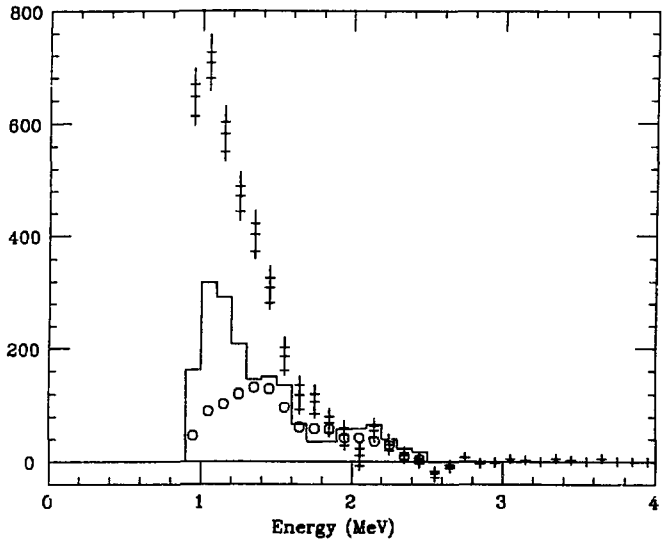

Figure 4.20: **Empty-Backgrounds as generated by three different methods.** Histogram: shifted and scaled Empty data. Open circles: simulated Empty data. Points with error bars: ^{96}Mo data after removal of Monte Carlo decay chain backgrounds. Errors on the histogram and open circles are as big as those on the ^{96}Mo points.

Energy shifts were found to depend mostly upon multiplicity, and not on energy. (High energy electrons could backscatter between detectors more than low energy electrons, making up for any lower average dE/dx at which they lost energy to films.) Two-detector, and three-detector events were treated separately. The shifts for two-detector events were typical of minimum ionizing electrons passing through twice the thickness of one film; i.e. as though only one film was encountered with mean angles of incidence around 60°. Energy shifts for three-detector events were, of course, larger by almost a factor of two.

Uncertainties in the resulting spectrum were somewhat ambiguously determined. Empty-data events in any particular energy bin were variously shifted to other bins. However, typical shifts could be discerned, and uncertainties were given by the product of all scaling factors times the square root of the number of events in the corresponding Empty-data bins.

Another rendition of the non-film background spectrum was generated by simulating the effects of incoming gamma rays when films were inserted. Energies and fluxes corresponding to those found to reproduce Empty data spectra were used. No scaling or shifting was required. Uncertainties in overall normalization were simply related to the statistics of simulated ^{214}Bi and ^{208}Tl gamma ray events needed to account for Empty data.

The final version of non-film backgrounds was obtained by subtracting ^{214}Bi and (equilibrated) thorium spectra from ^{96}Mo data. Contribution fractions similar to those derived in the last subsection for decay chain backgrounds in ^{100}Mo data were used. Following the same arguments, ^{234m}Pa contributions were not subtracted. Variations in the observed decay chain signal rates dominated overall uncertainties.

Above about 1.5 MeV, the three alternative non-film spectra agreed within errors. However, in certain energy regions of residual ^{100}Mo spectra bin-counts were smaller than these errors, so subtle differences could not be ignored. To avoid confusion, only one version - the final one - was chosen as best representing remaining backgrounds. The bases of this choice were many-fold...

- The first version was produced in a rather rough and ad-hoc way, resulting in large and ambiguous bin-to-bin uncertainties. Also, the sources of Empty data had to be assumed to be of a certain type.

- For the second version, an even more specific hypothesis for the origins of Empty spectra was required.

- On "global" grounds, the use of either of the above spectra was questionable. Series 13 (by which Empty data was otherwise known) displayed the greatest run-to-run variation in collected event rates. The boil-off nitrogen purging system had just been established, and may not have stabilized. Series 13 was taken well before the majority of ^{100}Mo data (series 17) and for a relatively short duration. Background

rates may have changed a little; e.g. as a result of changes that did occur in operating conditions underground (i.e. in airflow patterns). Finally, most of ^{100}Mo data was collected when there were films in the lower half of the array, which may have emitted gamma rays into the upper half. Those films remained during series 18 (when ^{96}Mo data was taken) but were absent in series 13.

- For the final version of non-film backgrounds, no assumptions needed to be made about the origin(s) of Empty data, or the effects of films on that data. Series 18 was taken just after most of the ^{100}Mo data, and its live time was relatively long. Certainly, the ^{96}Mo and ^{100}Mo films held differing levels of contamination, and could even contain dissimilar species of contaminants. In fact, there is a hint in Figure 4.20 – an enhanced count rate in the region from 1.4 to nearly 2 MeV – that the ^{96}Mo data include some extra background(s); but those backgrounds not uncovered by tagging decay sequences would have to be considered anyway.

Final Assessment: Could Anything Have Been Missed?

After all confirmed backgrounds had been subtracted from ^{100}Mo data, the residual spectrum of Figure 4.21 remained. (To obtain this Figure, the spectra of Figures 4.18, 4.19 and 4.20 were first added together, and the combined background then subtracted from the lowest spectrum of Figure 4.17.) Before any fits of double beta decay signals could be attempted, an assessment of hitherto unaccounted for (or "missing") background sources had to be made.

The first two versions of non-film background spectra were not subsequently discarded, but played an important role in limiting the possibilities for missing sources. The correspondence above 1.5 MeV among the spectra of Figure 4.20 was evidence that few backgrounds were neglected in the ^{96}Mo data. But just as significantly, this correspondence served to bolster confidence in the entire procedure; using tagged signals from decay sequences to estimate background rates and then simulating the contributions of those backgrounds after cuts. (For example, alpha collection efficiencies could not have been too far wrong.)

If ^{234m}Pa had been in equilibrium with ^{214}Bi in the ^{96}Mo films the above correspondence would not have been so strong. To check this, a version of the non-film spectrum

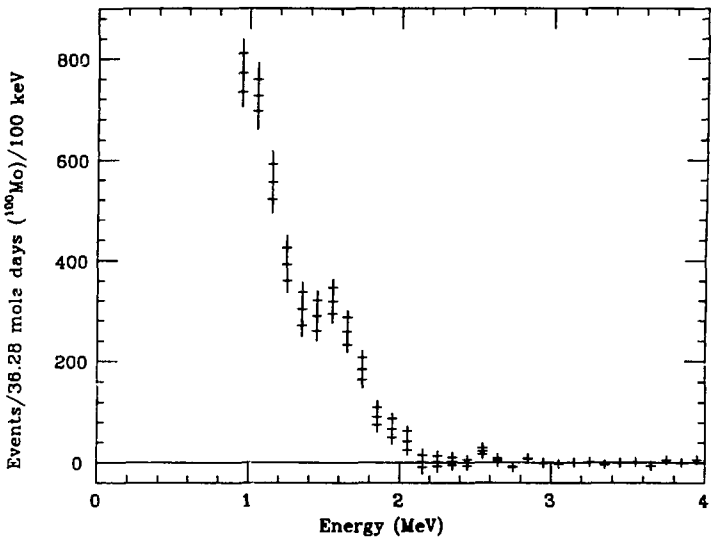

Figure 4.21: **Residual spectrum of ^{100}Mo data.**

Systematic uncertainties (given by high and low horizontal bars) were obtained by linearly extremizing backgrounds from contamination and non-film sources before subtracting same from ^{100}Mo data. Vertical error bars indicate combined statistical uncertainties (added in quadrature, bin by bin, from all sources).

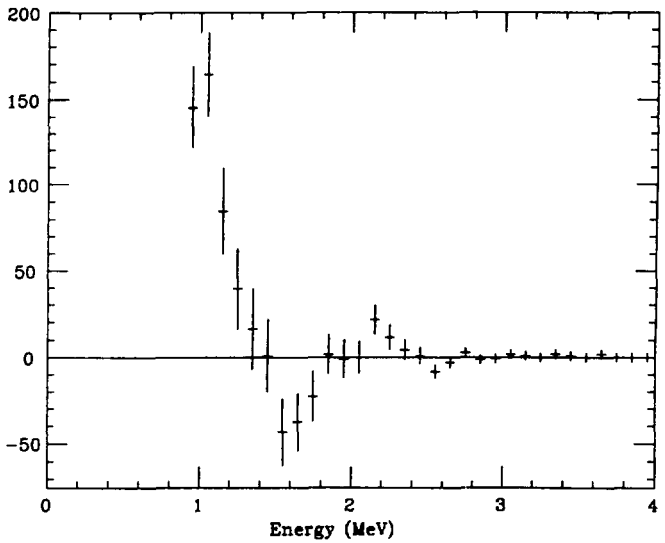

Figure 4.22: **The ^{96}Mo spectrum after subtracting equilibrated Uranium and Thorium backgrounds.**

was produced from ^{96}Mo data with the ^{238}U chain assumed to be in equilibrium (see Figure 4.22). The resulting hole at $\sim$ 1.6 MeV is clear evidence against equilibration. This did not mean, however, that the ^{238}U chain was not in equilibrium in the ^{100}Mo films. Contributions from ^{234m}Pa could not be neglected, and were included in the final fits.

To circumscribe the characteristics of any other background source that might exist, the following set of criteria were assembled.

- It could not be a pure alpha emitter, since one-detector events were cut.
- It could not emit positrons or intense gamma rays, since when discontiguous events were examined no significant Compton edges were found. (Positrons would produce annihilation gamma rays, and the number of discontiguous events could be quite sensitive to gamma ray sources.)
- The lack of Compton edges (other than those already accounted for) in Empty and residual spectra meant that it had most likely to be a beta source contained in the films.
- It had to produce events over 1.4 MeV with some substantial relative intensity. Beta decays with end-points lower than $\sim$ 1.5 MeV could be ignored.
- It had to be maintained by a parent isotope with a half-life of at least one year; otherwise a fall-off of event rates after cuts would have been noted throughout series 14-17.
- Its origin could not be too far-fetched. For example, by absorbing a neutron and emitting a gamma ray, ^{153}Eu may become ^{154}Eu which has a half-life of 8.5 years and which beta decays with an end-point of nearly 2 MeV; but where could the ^{153}Eu come from?

The most likely background sources to satisfy these criteria, besides the thorium and uranium sources already known to be present, were fission/fallout products. Among these, ^{90}Sr could occur with highest probability. It has a half-life of 28.8 years and decays to ^{90}Y which, in turn, beta decays with an end-point of 2.29 MeV. This last step occurs over 99% of the time without any coincident gamma ray emission, which makes

^{90}Y decay appear similar to that of ^{234m}Pa (a 98.6% probable beta decay with the same end-point). (An obvious origin for ^{90}Sr contamination was fallout from the Chernobyl disaster. This occurred about one year before the ^{100}Mo films were made. The ^{96}Mo films, which were made two years after Chernobyl, might not be expected to contain the same levels of contamination.)

Many, more exotic background sources were investigated. All were discarded.

4.4.3 Fits for Broad-Spectrum Double Beta Decay

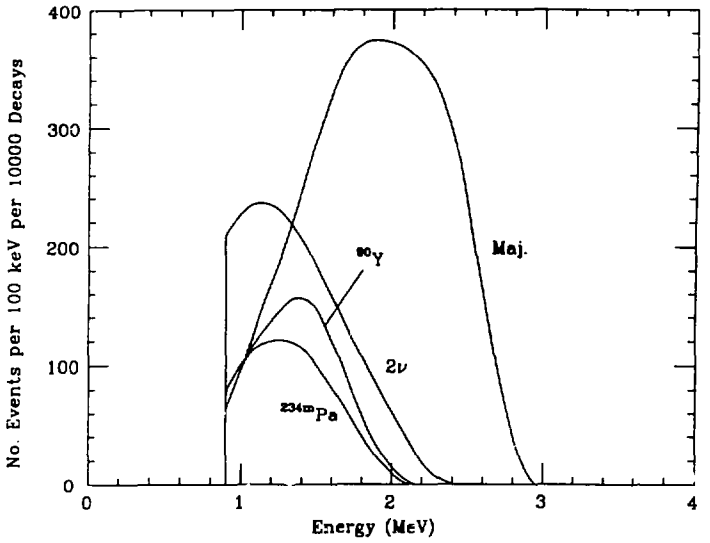

Figure 4.23: **Backgrounds and signals, after cuts to be fit to residual ^{100}Mo spectrum.**

The "missing" backgrounds fitted to the residual spectrum of Figure 4.21 were from ^{234m}Pa and/or ^{90}Y beta decays. All combinations of one or the other or both (or neither) ^{234m}Pa and ^{90}Y backgrounds were tried. At the same time, only one ^{100}Mo double beta decay signal was fitted - from either the two-neutrino or else the Majoron decay mode. Thus, maximum signal amplitudes were not limited by the assumed contributions from

other double beta decay modes. In this way conservative bounds on lifetimes could be established.

To obtain the appropriate spectra, cuts were imposed on simulations including many thousands of events for each of these backgrounds and signals. Bin-to-bin jitter was removed by hand by drawing smoothly varying curves though Monte Carlo spectra. (None of these decays involve coincident gamma ray emissions which might produce Compton edges, so they should return relatively smooth spectra.) The results (see Figure 4.23) reproduce spectral shapes from an effectively infinite number of simulated events, reducing statistical errors.

Systematic errors in spectral shape were likely to be minor, as evidenced by the previous analyses. In every case in which real and simulated backgrounds had been compared (tagged ^{214}Bi signals, Empty data and the three versions of non-film backgrounds) a good correspondence was obtained.

There remained only subtle differences between ^{234m}Pa, ^{90}Y and two-neutrino spectral shapes. (Since ^{90}Y beta decay is first-forbidden, and its nuclear charge is smaller than that of ^{234m}Pa - resulting in differing Coulombic effects - their spectral shapes are not identical.) Shape information could be retained, and differences accounted for, by subdividing the 1.4-3.0 MeV region into sufficiently many bins. It was unnecessary, however, to choose bins narrower than the sharpest spectral features. Widths of 100 keV were quite fine enough.

Uncertainties in the residual spectrum deserve some comment. Statistical errors from each of the ^{100}Mo and ^{96}Mo data samples and from all background contributions were added in quadrature, bin by bin. These are represented by the error bars in Figure 4.21, and were reflected in the least-square fitting uncertainties (and χ^2's).

Systematic errors were handled conservatively. The three subtracted backgrounds - from non-film, uranium and thorium chain sources - had been assessed separately. There were not sufficiently many different components to these assessments that systematic variations for each background could be considered independently of the others. (For example; over-estimated alpha collection efficiencies would affect all decay chain background rates similarly.) Therefore, variations in decay chain contaminations were added linearly in such a way as to extremize their contributions to total, residual background levels. Fits to the resulting maximized and minimized residual spectra were

Background(s)		$\beta\beta$ spectrum (region of fit)	$\chi^2/D \circ F$
^{234m}Pa	^{90}Y	no $\beta\beta$ decay (1.4-2.2 MeV)	
$-395 \pm 1032^{+533}_{-648}$	$1645 \pm 1054^{+809}_{-677}$	——	1.794/6
$1209 \pm 95^{+139}_{-126}$	——	——	4.228/7
——	$1243 \pm 97^{+150}_{-135}$	——	1.940/7
^{234m}Pa	^{90}Y	2ν (1.4-2.4 MeV)	
$-469 \pm 1309^{+46}_{-73}$	$1772 \pm 1743^{+364}_{-393}$	$-57 \pm 623^{+544}_{-579}$	1.810/7
$815 \pm 345^{+194}_{-242}$	——	$447 \pm 377^{+435}_{-363}$	2.844/8
——	$1170 \pm 460^{+271}_{-336}$	$80 \pm 491^{+531}_{-444}$	1.938/8
——	——	$1302 \pm 104^{+183}_{-162}$	8.413/9
^{234m}Pa	^{90}Y	Majoron (1.4-2.9 MeV)	
$-70 \pm 1104^{+133}_{-199}$	$1273 \pm 1145^{+295}_{-220}$	$85 \pm 101^{+118}_{-104}$	11.090/12
$1152 \pm 1039^{+82}_{-77}$	——	$129 \pm 94^{+130}_{-112}$	12.327/13
——	$1200 \pm 108^{+89}_{-81}$	$87 \pm 95^{+125}_{-108}$	11.094/13

Table 4.5: **Contributions to the residual spectrum of ^{100}Mo data.**
Read "$D \circ F$" as "Degrees of Freedom". The first error is statistical and the second is systematic.

Background(s)	$\beta\beta$ signal (energy region)	$\tau_{1/2}$ (yrs) (90% CL)
^{234m}Pa + ^{90}Y	2ν	$> 2.61 \times 10^{18}$
^{234m}Pa		$> 2.74 \times 10^{18}$
^{90}Y	(1.4-2.4 MeV)	$> 2.79 \times 10^{18}$
^{234m}Pa + ^{90}Y	Majoron	$> 5.42 \times 10^{19}$
^{234m}Pa		$> 4.77 \times 10^{19}$
^{90}Y	(1.4-2.9 MeV)	$> 5.32 \times 10^{19}$

Table 4.6: **Half-life limits on the broad-spectrum double beta decay modes of ^{100}Mo.**

then compared with the earlier fits. Systematic errors could be obtained by noting the differences in fitting parameters.

The results of least-squares fitting are listed in Table 4.5. Fits were limited to energy regions in which missing background and/or double beta decay contributions were non-zero. The volume of residual counts in each region was 1255.4 (from 1.4 to 2.2 MeV), 1259.6 (from 1.4 to 2.4 MeV) and 1284.4 (from 1.4 to 2.9 MeV). As expected, all fits tended to account for these numbers of counts.

By itself, the spectral shape reflective of two-neutrino double beta decay did not match the residual spectrum very well. This was taken as evidence that, indeed there were missing backgrounds. Fitted separately, the χ^2 for ^{90}Y was more than twice as good as that for ^{234m}Pa. When fitted simultaneously, ^{90}Y was heavily favored. If there really were $1243 \pm 97^{+150}_{-135}$ counts from ^{90}Y decay in the residual spectrum, then the contamination of ^{90}Sr in the ^{100}Mo films must have surpassed that in the ^{96}Mo films by around $(4.4 \pm 0.6) \times 10^{-18}$ parts by weight. If, instead, there were $1209 \pm 95^{+139}_{-126}$ counts from ^{234m}Pa, then the indicated ^{238}U contamination difference was 2.8 ± 0.4 ppb by weight.

When missing backgrounds were included, double beta decay contributions could easily vanish, within errors. Hence, lower limits on lifetimes via two-neutrino and Majoron

decay modes were to be established. To calculate these, the statistical and systematic errors on fitting parameters were first added in quadrature. The resulting decay rate probability distributions could be thought of as following a nearly Gaussian form with most probable values close to zero. Next, negative (i.e. unphysical) signal contributions were excluded. A 90% confidence level limit on signals would then be indicated by the value at which 90% of the volume of the remaining distribution was reached.

Results are listed in Table 4.6. It can be seen that all fits returned closely similar half-life limits; i.e. there was little background dependence. Certainly, this could be traced to the size of the error bars in Figure 4.21 and the similarity of ^{234m}Pa and ^{90}Y spectra.

In the case of double beta decay via Majoron emission, a simple alternative method of establishing the half-life limit existed. There were no missing backgrounds expected to contribute with energies above about 2.1 MeV. Therefore, the residual spectrum could be accounted for entirely by signals from the Majoron decay mode. A fit in that region was not attempted, however, because bin counts were too small for Gaussian statistics to apply. (Normally distributed data, on a bin by bin basis is a prerequisite of least-squares fitting.) Instead, the number of events with energies between 2.1 and 2.9 MeV from the ^{100}Mo sample surviving cuts (284) was compared with the estimated total background ($252.6 \pm 40.8^{+17.9}_{-21.5}$) from non-film, uranium and thorium chain sources. A signal of $(284 - 252.6) \pm (284 + (40.8)^2 + (21.5)^2)^{1/2}$ events, together with a collection efficiency of 16.5% indicates a lower half-life limit of 6.7×10^{19} years at 90% confidence.

4.4.4 Reductions for Neutrinoless Decay

The analysis of neutrinoless modes in double beta decay was much less complex than for other modes. The transition energy of 3.033 MeV in ^{100}Mo put the signal above nearly all anticipated backgrounds. What backgrounds remained could be estimated in an almost completely empirical manner. Also, counting statistics were so small that simple, single-bin reductions were allowed.

The $0^+ \rightarrow 0^+$ and $0^+ \rightarrow 2^+$ transitions were treated separately.

$0^+ \rightarrow 0^+$ Transitions

Above about 2.5 MeV, non-film data could be ignored, and only three backgrounds from contaminants in the films needed consideration. One was ^{208}Tl decay, at the end of the ^{232}Th chain. The available energy is nearly 5 MeV, shared by a beta and gamma rays. Almost nothing could be done to reduce, or to estimate this contribution beyond those cuts and background analyses already performed.

The beta decay of ^{212}Bi, followed by ^{212}Po alpha decay could also produce 3 MeV, multi-detector events. (As described earlier, the two decays may occur too rapidly to be resolved by the fast clock. Energy depositions from both the beta and alpha would then combine, in possibly different detectors.) This contribution was difficult to simulate, but the availability of tagged ^{212}Bi events made simulations unnecessary. The number of such events could be scaled by the ratio of non-tagging to tagging probabilities.

Upon investigation, a feature peculiar to this background, but not to double beta decay was uncovered. In Figure 4.24 can be seen the ratio of energies (plotted against total energy) in two-detector events from tagged ^{212}Bi decays, untagged ^{100}Mo data and 4000 simulated neutrinoless decays. The lopsidedness of high energy tagged events is evident, and is present in the ^{100}Mo data but not in double beta decay. By requiring energy ratios of at least 1:3 in two-detector events, the signal to noise ratio for neutrinoless decay could be improved.

The last background to consider was ^{214}Bi decay. Contributions at high energies could be estimated empirically from the observed spectrum of tagged ^{214}Bi events. No features peculiar to this decay could be discerned.

The spectrum of events with energies between 2.5 and 3.1 MeV from the ^{100}Mo data sample, and surviving this augmented set of cuts is shown in Figure 4.25, together with the expected neutrinoless signal. Real data and double beta decay were indistinguishable: there were no statistically significant differences in event multiplicities nor any departures from randomness with respect to which detectors were involved. There was, however, a clear enhancement in the number of events with energies near 2.6 MeV. Whatever the cause (photoabsorption of 2.614 MeV gamma rays from ^{208}Tl decay?) the search for neutrinoless signals was subsequently restricted to energies above 2.7 MeV.

In the region from 2.7 to 3.0 MeV there remained 6 events. A contribution of $3.2 \pm$

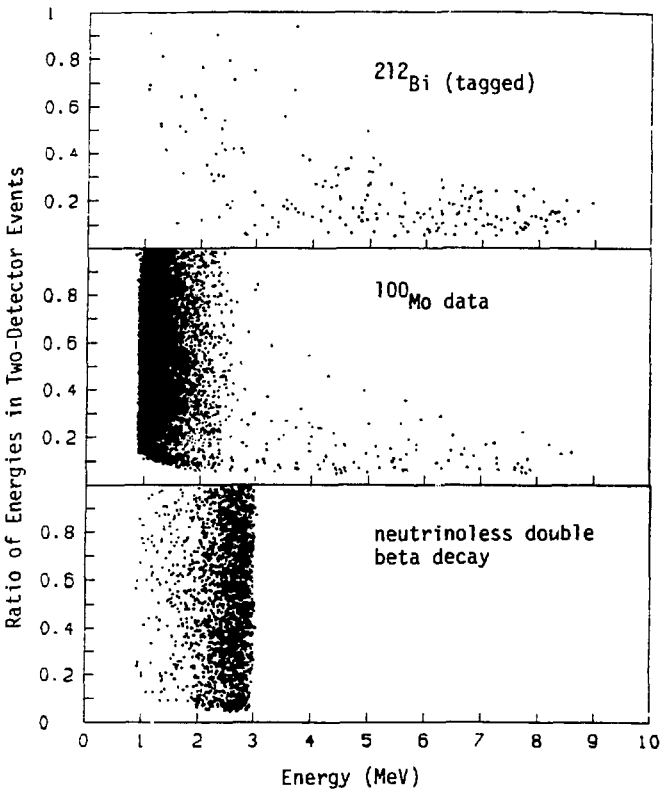

Figure 4.24: **Two-detector event energy ratios**

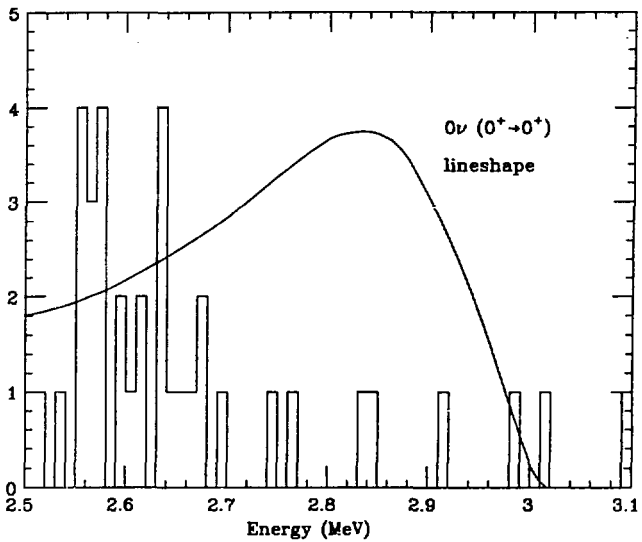

Figure 4.25: **Residual data in the neutrinoless $0^+ \rightarrow 0^+$ decay region.**

$1.6^{+0.2}_{-0.1}$ events could be expected from ^{208}Tl, given the results in Table 4.3 and Monte Carlo simulations. From 3 observed, tagged multi-detector ^{212}Bi decays in the energy interval of interest, an estimate could be made that 1.4 ± 0.8 untagged decays would survive the cuts. Only one, tagged ^{214}Bi event occurred with an energy between 2.7 and 3.0 MeV. When scaled by relative tagging probabilities, 55 ± 55 were expected to contribute after cuts. If Table 4.3 and Monte Carlo simulations could be used instead, $6.2 \pm 3.1^{+0.5}_{-0.2}$ untagged ^{214}Bi decays would result.

Total background contributions of 10.8 ± 3.5 events were expected. Hence, the indicated signal included $-4.8 \pm (6 + (3.5)^2)^{1/2}$ events. The collection efficiency, after cuts for neutrinoless decays in the energy interval 2.7-3.0 Mev was 25.0%. Following the same reasoning as was employed in the last subsection, the half-life for neutrinoless double beta decay of ^{100}Mo could be limited to 2.2×10^{21} years, at 90% confidence.

This result was felt to be somewhat conservative, and therefore rather robust. Recalling the multiplicity discrepancy of tagged ^{214}Bi events; if multiple scattering and/or dE/dx in the films was indeed overestimated by GEANT311, then the simulated neutrinoless peak was artificially broadened. (It is unclear whether neutrinoless event multiplicities might also be suppressed.) Therefore, the collection efficiency of 25.0% used above would be an under-estimate.

$0^+ \rightarrow 2^+$ Transitions

In a neutrinoless $0^+ \rightarrow 2^+$ transition, two decay electrons share less than the total decay energy. The rest is released electromagnetically, from the deexcitation of the daughter nucleus. In this experiment the gamma ray from double beta decay of ^{100}Mo, with an energy of 540 keV, was likely to escape the detector array without interacting. A neutrinoless signal/peak would result, much like that shown in Figure 4.25 but shifted down in energy. Analysis mirroring that above would then provide a half-life limit.

However, the augmented set of cuts used for $0^+ \rightarrow 0^+$ transitions did little to enhance signal to noise at lower energies. Also, more backgrounds contributed, and non-film sources could not be ignored. In Figure 4.26 the comparison is made between residual data and a neutrinoless $0^+ \rightarrow 2^+$ signal apropos of 10,000 simulated decays. (The high energy tail resulted when deexcitation gamma rays scattered locally, depositing energy in the same detectors traversed by the electrons.) For energies between 2.1 and 2.5

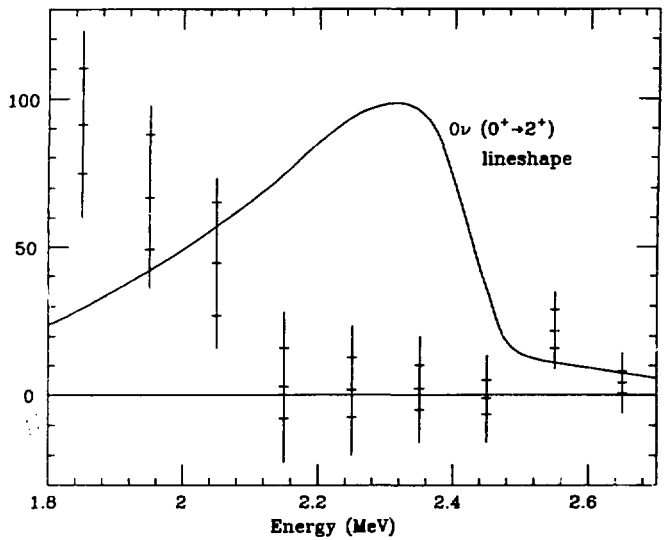

Figure 4.26: **Residual spectrum in the region of the $0^+ \rightarrow 2^+$ peak.**

MeV there were 237 events collected, after cuts, while the background was estimated at $231.5 \pm 37.3^{+16.6}_{-19.9}$ events. With a collection efficiency of 29.8% included, the half-life for this mode of decay could be limited to 1.6×10^{20} years, at 90% confidence.

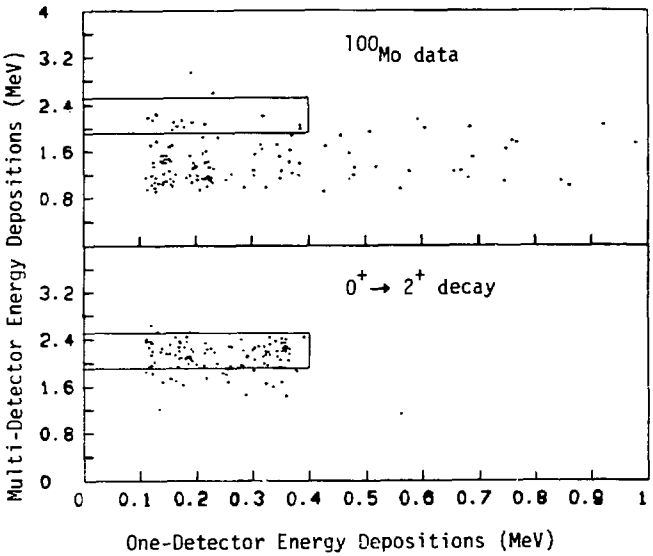

Figure 4.27: Energies of discontiguous events.

The energy deposited in a contiguous set of detectors containing most of the energy in the entire event is plotted against separated, one-detector depositions.

If the deexcitation gamma ray did not escape the array, and yet did not interact locally, a discontiguous signal may result. Certainly this would occur with much reduced probability, but backgrounds for such events would also be severely restricted. A modified set of cuts appropriate to this signal might be as follows; two, separated depositions could be sought, the one containing most of the energy satisfying the cuts imposed as before – except for discontiguousness – on double beta decay signals while the other could involve only one detector and occur anywhere in the array. Figure 4.27 shows the results of these cuts on ^{100}Mo data and Monte Carlo simulations of $0^+ \rightarrow 2^+$ double beta decay. A window of 0-400 keV on one-detector energy depositions and 1.9-2.5 MeV on

multi-detector depositions contains 13 ^{100}Mo events and 2.3% of the decay signal.

Only ^{214}Bi, ^{212}Bi and ^{208}Tl decays in the uranium and thorium chains would be expected to contribute from contamination within the films. The two former sources could be assessed by counting the numbers of real events, surviving cuts, which were read out with nonzero fast clock times. No tagged events fell within the acceptance window. Untagged decays, however, would occur with greater probability. Given the levels of contamination listed in Table 4.3, 3 ± 3 events could result from ^{214}Bi and ^{212}Bi decay, as estimated via Monte Carlo analysis. Similarly, an estimate of 7 ± 2 events from ^{208}Tl beta+gamma decay was obtained. (In this latter contribution the decay electron could deposit some energy, while the 2.614 MeV gamma ray may scatter discontiguously.)

Non-film backgrounds for this signal were not taken from ^{96}Mo data. Beside those decays already accounted for, no other source common to both ^{96}Mo and ^{100}Mo films could be expected to contribute. When the same cuts were imposed on the Empty data sample, however, three events remained within the acceptance window. This was determined, through Monte Carlo simulation, to be consistent with doubly scattered ^{208}Tl gamma rays; indicating a ^{232}Th contamination in the surrounding lead shield of 0.3 ± 0.2 ppb by weight (consistent with earlier findings). The presence of films would reduce the observed energies and multiplicities, taking some events out of the window. After scaling by relative live times, 9 ± 7 events were estimated to contribute from non-film backgrounds.

Total background contributions of 18 ± 8 events were expected, nearly all due to ^{208}Tl decay. A signal of approximately -5 ± 9 events remained, from which a half-life limit of 8×10^{19} years could be obtained, at 90% confidence. The correspondence with 1.6×10^{20} years, found earlier, was taken as an indication that this latter method – of seeking discontiguous events – had merit despite reduced statistical significance.

Chapter 5

Summary and Conclusions

In this experiment thin source films containing ^{100}Mo were interleaved and observed with a coaxial array of windowless silicon detectors. All materials used in and around this array were selected for low levels of radioactivity. The entire assembly was positioned deep underground to eliminate cosmogenic activity; with heavy local, passive shielding and gaseous purging employed to further reduce ambient backgrounds.

Data taken included the amount of energy deposited in detectors, the timing between events and the time intervals between occasional, rapid sequences of events. The system worked more or less continuously for over one year without major difficulties. During this time calibration drifts were accurately tracked and various other source films were installed, to study backgrounds. Due to the presence of a few bad channels, and to the choices made in background analysis, part of the array and certain runs were disregarded in the search for double beta decay. The total ^{100}Mo exposure obtained was 0.0994 mole years.

A systematic study of backgrounds was instituted, with results (in terms of spectra, collection efficiency variations, etc.) that largely conformed with modelling and Monte Carlo expectations. From the observation of short-lived decay sequences, the ^{100}Mo films were found to be contaminated with uranium and thorium decay chains at levels of a few parts per billion by weight. Dummy films containing ^{96}Mo separated at the same time as the ^{100}Mo contained differing levels of contamination. As evidenced by fitting inconsistencies (between ^{96}Mo data and measured ^{214}Bi plus assumed ^{234m}Pa contributions) the uranium chain was definitely broken in the dummy films.

Decay Mode	$\tau_{1/2}$ (yrs) (90% confidence levels)
2ν	$> 2.7 \times 10^{18}$
Majoron	$> 5.2 \times 10^{19}$
0ν $(0^+ \rightarrow 0^+)$	$> 2.2 \times 10^{21}$
0ν $(0^+ \rightarrow 2^+)$	$> 1.6 \times 10^{20}$

Table 5.1: **Half-life limits for ^{100}Mo double beta decay obtained in this experiment.**

Non-film backgrounds could be analyzed variously; reflecting data obtained when *no* films were present in the array, or the remaining ^{96}Mo data after accounting for known decay chain contributions. The latter results were chosen as most representative.

All confirmed background contributions to the ^{100}Mo data were subtracted. By fitting the residual spectrum, missing backgrounds could be assessed. The most likely missing contributions were all that was needed to completely account for the residual data. (This consisted of either fallout ^{90}Sr at around 4.4 parts per 10^{18}, or enough ^{234m}Pa to allow the ^{238}U chain in the ^{100}Mo films to be in equilibrium – equivalent to 3.4*to*6.8 ppb of ^{238}U depending on the amount of equilibrated ^{238}U there was in the ^{96}Mo films.) Signals from double beta decay were not required, nor were fits substantially improved by invoking their presence.

Contributions from the broad-spectrum – two-neutrino and Majoron – modes of double beta decay could be limited by least-squares fitting results. Neutrinoless decay mode contributions were restricted simply by the numbers of events surviving cuts, compared with estimated backgrounds. In all cases, 90% confidence level half-life limits were calculated (see Table 5.1). The results exceed those achieved by any other previous experiment using ^{100}Mo as a source. (In the case of neutrinoless $0^+ \rightarrow 0^+$ transitions, confidence levels on the half-life limit have been increased.)

The comparison with earlier results from this same experiment does not seem as favorable. Much of the variation can be accounted for by differences in the analysis. In

the present work procedures leading to new limits for neutrinoless double beta decay have been altered as follows (each of which tend to reduce the attainable half-life).

- 90% confidence level limits were sought, rather than "1σ" limits.
- Data were restricted by the elimination of series 15 and by neglecting events from below detector #19.
- Cuts were "looser" in that energy deposited in detectors on either side of bad channels was not used to veto events.
- The neutrinoless peak simulated by GEANT311 was wider than that predicted by the earlier Monte Carlo program.
- Backgrounds have been accounted for. Before, half-life limits were derived by assuming the maximum neutrinoless signal was given by the square root of the total number of remaining counts, after all cuts were imposed; i.e. without reference to estimated background contributions and uncertainties.

For the broad-spectrum modes of double beta decay, differences with past analyses amount to...

- The ^{238}U decay chain was not assumed to be in equilibrium.
- Non-film backgrounds were obtained with the use of dummy films, not from data arising when the array was empty.
- The treatment of systematic errors was more detailed in that no crude, across-the-board estimate of uncertainties, good for all background signals, was entertained.
- Unphysical (i.e. negative) decay rates were disallowed.

Throughout the present analysis, an effort has been maintained to treat data and uncertainties conservatively. Caution was not so great that, for example, missing background spectra fit the residual data much better than anticipated given the size of error bars. Consequently, it is expected that the half-life limits presented here are more "robust"; i.e. that these results will not fluctuate severely but improve with the accumulation of more data.

To convert the limits of Table 5.1 into numbers of theoretical interest the appropriate matrix elements must be extracted. For this purpose, the formulae of Chapter 2 should be referred to, together with the integrated kinematical factors of Table 2.1. Assuming Gamow-Teller dominance, the half-life limit for two-neutrino decay restricts the corresponding matrix element, $|M_{GT}^{2\nu}|/(\mu/m_e c^2)$ to values below 0.20. If the curves of Figure 2.6 are employed (derived from the results of Engel et. al. [29]) then the neutrinoless matrix element, $|M_{GT}^{0\nu}|$ will be forced to obtain values above about 1.14. The half-life for neutrinoless, $0^+ \rightarrow 0^+$ transitions, and the formula of Section 2.3 can then be used to limit the effective majorana neutrino mass and right-handed coupling constants, with the results,

$$\begin{aligned} \langle m_\nu \rangle &< 35\text{eV}, \\ \langle \lambda \rangle &< 3.8 \times 10^{-5}, \\ \langle \eta \rangle &< 3.7 \times 10^{-7}. \end{aligned}$$

Similarly, the effective Majoron coupling can be restricted;

$$\langle g_M \rangle < 2.3 \times 10^{-3}.$$

These mass and coupling constant limits are six (or around fifteen) times worse for $\langle g_M \rangle$ (or $\langle m_\nu \rangle$, $\langle \lambda \rangle$ and $\langle \eta \rangle$) than those achieved earlier by experiments using different double beta decay candidates. However, those previous limits were determined utilizing different matrix element calculations (in the case of the above comparison, those of Tomoda and Faessler). It should be remembered that theoretical expectations have not yet proven completely stable. An accurate comparison between experiments should await the reliable calculation, among various authors, of matrix elements for ^{100}Mo as well as other isotopes. For now, probably the most objective procedure is to relate empirical findings after accounting for known kinematical factors. By this measure, the limits noted above become only four (or seven) times worse than earlier achievements.

Appendix A: Alpha Collection Probabilities

The following idealizations are invoked..

- contaminants are isotropically distributed throughout films of uniform composition and density.
- nearby film surfaces are planar
- alpha trajectories are straight and there is no straggling.

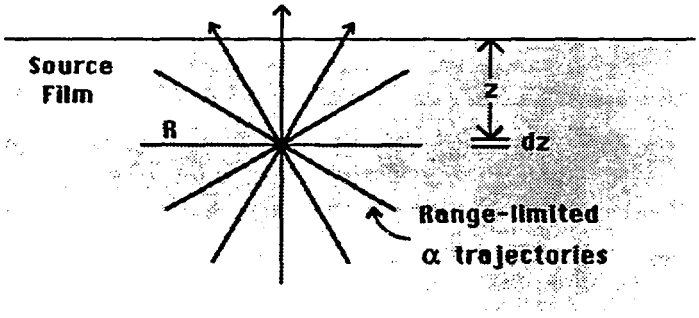

Refer to the above figure and consider an alpha emitted at depth z to $z + dz$, which is less than its range, R in a film. The exitting probability is given by the likelihood that it is emitted into the solid angle $\Omega = 2\pi(1 - \frac{z}{R})$. In a sequence of n alphas, emitted from the same point, the probability that all exit the film through the same face is given by $\prod_{i=1}^{n} \frac{\Omega}{4\pi} = (\frac{1}{2})^n \prod_{i=1}^{n}(1 - \frac{z}{R_i})$ where R_i $(i = 1, 2, \ldots, n)$ are the ranges

The normalized density of emission sites throughout a film of thickness t is $\frac{d\eta}{dz} = \frac{1}{t}$ if contamination is isotropically distributed. The probability that all n alphas in a sequence exit a film whose thickness is greater than all their ranges, either via one face or else the other, regardless of emission depth, is therefore

$$2(\frac{1}{2})^n \int_0^{R_{min}} \prod_{i=1}^{n} (1 - \frac{z}{R_i}) \frac{dz}{t},$$

where R_{min} is the minimum range among the alphas. If, in addition, all alphas must exit with more than a certain kinetic energy, T_{thresh} then effective ranges, $R_i = R_i(T_o) - R_i(T_{thresh})$ should be used, where T_o is their initial energies.

Similar reasoning can be followed to obtain the probability that all but one of the alphas (say, the last one) exit the film...

$$2(\frac{1}{2})^n \int_0^{R^e_{min}} \prod_{i=1}^{n-1} (1 - \frac{z}{R_i})(1 + \frac{z}{R_n}) \frac{dz}{t},$$

where R^e_{min} is the minimum $R_i(T_o) - R_i(T_{thresh})$ for those alphas that do exit.

Appendix B: Background Analysis

Refer to the body of this dissertation for further information.

The preliminary cuts, vetos and definitions were as follows;

bad channels The energy recorded in a "bad" channel was set to zero.

offline threshold The energy recorded in each detector had to exceed 110 keV, else it was set to zero.

cross-talk ratio The energy recorded in each detector had to exceed $(\frac{1}{20})^{th}$ that recorded in any other detector, else it was set to zero.

vetos For backgrounds in metalic films, channels #1-19 and #40 were used as vetos. For backgrounds in blank films, channels #1-3 and #19-40 were used as vetos.

off-line trigger threshold At least one channel had to contain over "trigger" in energy (to be set for each signal separately).

alphas An "alpha" was defined as a one-detector event with more than 2 Mev of recorded energy.

slow(C) The time interval since the last event occured in the same channel.

fast The time recorded by the fast clock.

E The energy recorded.

The specific decay sequences observed are listed below, labelled by the radioactive isotope which decayed first. Short descriptions of the signal cuts are given. All physically

independent events, which must have occured in order that the cuts be satisfied, are also listed. Quantities in parentheses are probabilities of occurance. The notation, 'GEANT' indicates that the corresponding probability was determined for each data sample separately from Monte Carlo analysis. Alpha exitting probabilities are listed, first for blank films and then for ^{100}Mo films. For ^{96}Mo films, compositional differences led to a $\approx 4\%$ increase in alpha-exitting probabilities over those for ^{100}Mo films.

Tagged Betas

^{214}Bi(1): one-detector events tagged with 20μs<fast<1ms, trigger=500 keV, $E < 3$ MeV.

- ^{214}Bi beta triggers and makes cuts (GEANT)
- ^{214}Po alpha exits film w/ $E > 315$ keV (0.650,0.2189)
- ^{214}Po decays in time window (0.9643)

^{214}Bi(2): contiguous, multi-detector events (involving more than one but fewer than 5 detectors) tagged with 20μs<fast<1ms, trigger=500 keV, $E < 3$ MeV.

- ^{214}Bi beta triggers and makes cuts (GEANT)
- ^{214}Po alpha exits film w/ $E > 315$ keV (0.650,0.2189)
- ^{214}Po decays in time window (0.9043)

^{212}Bi: contiguous events, involving fewer than 5 detectors, tagged with 200ns < fast < 2μs, trigger=315 keV, channels #25, 27 and 39 are used as vetos for one-detector events (due to double-pulsing).

- ^{212}Bi beta triggers and makes cuts (GEANT)
- ^{212}Po alpha exits film w/ $E > 315$ keV (0.728,0.2764)
- ^{212}Po decays in time window (0.6168)
- Branching fraction to ^{212}Po (0.64)

^{213}Bi: contiguous events, involving fewer than 5 detectors, tagged with 2μs <fast< 20μs, trigger=315 keV, channels #25, 27 and 39 are used as vetos for one-detector events (due to double-pulsing).

- ^{213}Bi beta triggers and makes cuts (GEANT)

- ^{213}Po alpha exits film w/ $E > 315$ keV (0.699,0.2518)
- ^{213}Po decays in time window (0.6820)
- ^{213}Po branching fraction (0.978)

Table 1

GEANT311 TAGGED BETA COLLECTION EFFICIENCIES

SIGNAL	empty	blank	^{96}Mo	^{100}Mo
^{214}Bi(1)	0.3	0.28 ± 0.014	0.2594 ± 0.0044	0.2415 ± 0.0043
^{214}Bi(2)	0.1	0.11 ± 0.010	0.0788 ± 0.0027	0.0724 ± 0.0026
^{212}Bi	0.7	0.68 ± 0.015	0.5362 ± 0.0050	0.4990 ± 0.0050
^{213}Bi	0.5	0.48 ± 0.016	0.0673 ± 0.0025	0.0613 ± 0.0024

Tagged Alphas

^{224}Ra(1): alpha-to-alpha in the same channel, both untagged, separated in time as 10<slow(C)<100sec.

- ^{224}Ra and ^{220}Rn alphas exit film w/ $E > 2$ MeV and either
  - ^{216}Po alpha decays after readout (0.0249 for Kinetics runs; 0.0346 for IBM runs), or
  - ^{216}Po decays before readout is complete for ^{220}Rn alpha, but does not exit film w/ $E > 315$ keV (0.00725 for Kinetics runs, 0.00160 for IBM runs)
- OR ^{220}Rn alpha does not exit film w/ $E > 315$ keV but ^{216}Po alpha exits w/ $E > 2$ MeV (0.0233). Alpha exitting probabilities for balnk films are ~ 3 times higher for blank films, in each of the above cases.
- ^{220}Rn decays within time window (0.5953)

^{224}Ra(2): as ^{224}Ra(1) but where the second alpha is tagged as 10<fast<70ms. (For IBM runs this signal is not sought.)

- ^{224}Ra and ^{220}Rn alphas exit film w/ $E > 2$ MeV and ^{216}Po alpha exits w/ $E > 315$ keV (0.040,0.0157)

- ^{220}Rn decays within time window (0.5953)
- ^{216}Po decays within time window (0.2377)

^{224}Ra(3): alpha-to-alpha-to-alpha in the same channel, each untagged with 10 < slow(C) < 100sec for the time between the first pair and 110ms < slow(C) < 1sec in Kinetics runs or 20ms < slow(C) < 1sec in IBM runs for the time between the second pair.

- All alphas exit film w/ $E > 2$ MeV (0.038,0.0151)
- ^{220}Rn decays within time window (0.5953)
- ^{216}Po decays within time window (0.5827 Kinetics, 0.9004 IBM)

^{220}Rn(1): as ^{224}Ra(1) but with 0.2<slow(C)<1sec.

- ^{220}Rn and ^{216}Po alphas exit film w/ $E > 2$ MeV (0.147,0.0449)
- ^{216}Po decays within time window (0.3760)

^{220}Rn(2): tagged alpha, with 10<fast<70ms. (For IBM runs this signal is not sought.)

- ^{220}Rn alpha exits film w/ $E > 2$ MeV and ^{216}Po alpha exits w/ $E > 315$ keV (0.157,0.0480)
- ^{216}Po decays within time window (0.2377)

^{223}Ra(1): as ^{224}Ra(1) but with 1<slow(C)<10sec.

- ^{223}Ra and ^{219}Rn alpha exit film w/ $E > 2$ MeV and ^{215}Po decays after $\approx$ 200ns but exits film w/ $E < 315$ keV (0.067,0.0225), or
- ^{219}Rn alpha does not exit film w/ $E > 315$ keV but ^{215}Po alpha exits w/ $E > 2$ MeV (0.073,0.0243)
- ^{219}Rn decays within time window (0.6657)

^{223}Ra(2): as ^{223}Ra(1) but where the second alpha is tagged as 100μs<fast<5ms.

- ^{223}Ra and ^{219}Rn alphas exit film w/ $E > 2$ MeV and ^{215}Po alpha exits w/ $E > 315$ keV (0.054,0.0169)
- ^{219}Rn decays within time window (0.6657)
- ^{215}Po decays within time window (0.8194)

^{219}Rn(2): as ^{220}Rn(2) but with 100μs<fast<5ms.

- ^{219}Rn alpha exits film w/ $E > 2$ MeV and ^{215}Po alpha exits w/ $E > 315$ keV (0.182,0.0552)
- ^{215}Po decays within time window (0.8194)

^{221}Fr(1): as ^{224}Ra(1) but with 110 < slow(C) < 200ms in Kineitcs runs, 20 < slow(C) < 200ms in IBM runs.

- ^{221}Fr and ^{217}At alphas exit film w/ $E > 2$ MeV (0.153,0.0466)
- ^{217}At decays within time window (0.0807 Kinetics, 0.6374 IBM)

^{221}Fr(2): as ^{220}Rn(2), exactly.

- ^{221}Fr alpha exits film w/ $E > 2$ MeV and ^{217}At alpha exits w/ $E > 315$ keV (0.159,0.0492)
- ^{217}At decays within time window (0.5842)

Table 2

TOTAL COLLECTION EFFICIENCIES

SIGNAL	empty	blank	^{96}Mo	^{100}Mo
^{214}Bi(1)	0.2	0.165	0.0534	0.0478
^{214}Bi(2)	0.07	0.062	0.0162	0.0143
^{212}Bi	0.2	0.195	0.0608	0.0544
^{224}Ra(1)	0.01	0.096	0.0341	0.0297
^{224}Ra(2)	0.006	0.0047	0.00214	0.00201
^{224}Ra(3)	0.01	0.013	0.00842	0.00522
^{220}Rn(1)	0.05	0.054	0.0162	0.0149
^{220}Rn(2)	0.04	0.036	0.0110	0.0103
^{223}Ra(1)	0.09	0.090	0.0300	0.0275
^{223}Ra(2)	0.03	0.029	0.0089	0.00815
^{219}Rn(2)	0.2	0.14	0.0435	0.0400
^{213}Bi	0.2	0.23	0.0120	0.0105
^{221}Fr(1)	0.01	0.012	0.0286	0.0090
^{221}Fr(2)	0.09	0.090	0.0277	0.0262

In the next table the numbers given indicate the number of events found in the time window of the cut minus the number of events estimated to occur accidentally in that time window. Accidentals were got by noting the volume and distribution of events found in a much larger and later time window (typically extending from 10 to 100 lifetimes beyond the signal sought), and those from an earlier time window.

Table 3

# EVENTS FOUND				
SIGNAL	empty	blank	^{96}Mo	^{100}Mo
^{214}Bi(1)	1-0	14-0	461-1	693-9
^{214}Bi(2)	0-0	8-0	176-1	286-1
^{212}Bi	1-0	26-3	58-8	408-23
^{224}Ra(1)	3-2	19-9	156-83	850-493
^{224}Ra(2)	2-0	3-0	2-0	20-5
^{224}Ra(3)	0-0	1-0	6-0	39-0
^{220}Rn(1)	0-0	14-2	24-3	164-23
^{220}Rn(2)	6-?	10-2	10-1	155-50
^{223}Ra(1)	2-1	5-2	18-17	180-100
^{223}Ra(2)	0-0	0-0	2-0	20-1
^{219}Rn(2)	3-1	5-2	12-2	162-19
^{213}Bi	0-0	3-2	70-64	145-110
^{221}Fr(1)	4-?	4-4	35-13	125-80
^{221}Fr(2)	6-?	10-2	10-1	155-50

The empty sample includes only channels #20-39, and the last 574.68 hours of empty running, when the slow clock was working. Question marks denote ambiguities. After folding in the collection efficiencies, the following final decay rates are found.

Table 4				
DECAY RATES (# decays per day)				
SIGNAL	empty	blank	^{96}Mo	^{100}Mo
^{214}Bi(1)	0.2 ± 0.2	1.6 ± 0.4	95.9 ± 4.5	61.4 ± 2.4
$\star^{214}$Bi(2)	0.0 ± 0.6	2.4 ± 0.9	120.3 ± 9.1	85.3 ± 5.1
^{212}Bi	0.2 ± 0.2	2.2 ± 0.5	9.2 ± 1.5	30.4 ± 1.6
^{224}Ra(1)	4.2 ± 9.3	1.9 ± 1.0	23.8 ± 5.0	51.5 ± 5.3
$\star^{224}$Ra(2)	15 ± 11	$12. \pm 7.0$	10.4 ± 7.4	42.5 ± 14.2
$\star^{224}$Ra(3)	0.0 ± 3.2	1.4 ± 1.4	7.9 ± 3.2	32.0 ± 5.3
$\star^{220}$Rn(1)	0.0 ± 0.8	4.2 ± 1.4	14.4 ± 3.6	40.6 ± 4.0
^{220}Rn(2)	$7\pm$?	4.1 ± 1.8	9.1 ± 3.4	58.1 ± 7.9
^{223}Ra(1)	0.5 ± 0.8	0.6 ± 0.5	0.4 ± 2.2	12.5 ± 2.6
^{223}Ra(2)	0.0 ± 1.4	0.0 ± 0.6	2.5 ± 1.8	10.0 ± 2.4
^{219}Rn(2)	0.6 ± 0.6	0.4 ± 0.3	2.6 ± 1.0	11.1 ± 1.3
^{213}Bi	0.0 ± 0.2	0.1 ± 0.2	5.6 ± 10.7	14.3 ± 6.5
^{221}Fr(1)	$14\pm$?	0.0 ± 4.4	8.6 ± 2.7	21.4 ± 6.8
^{221}Fr(2)	$2.8\pm$?	1.7 ± 0.7	3.6 ± 1.3	22.8 ± 3.1

The four sections group together signals from the ^{238}U, ^{232}Th, ^{235}U and ^{237}Np decay chains. "Decay rates" refer to the daily activity of **parent** isotopes indicated by the number of observed decay sequence signals. Starred signals were used to compute contamination levels. The errors are statistical (Gaussian) only. Errors for vanishing rates were computed as though a single accidental event was observed.

Bibliography

[1] This refers to the last term in the Liquid-drop model, semi-empirical formula for nuclear masses; first investigated by W. Heisenberg, Ziets. f. Physik **78**, 156 (1932)

[2] M. Goeppert-Mayer, Phys. Rev. **48**, 512 (1935)

[3] G. Racah, Nuovo Cimento **14**, 322 (1937)

[4] W. Furry, Phys. Rev. **56**,1184 (1939)

[5] R. Davis, Phys. Rev. **97**, 766 (1955)

[6] T. Lee and C. Yang, Phys. Rev. **104**, 254 (1956)

[7] C. Wu, E. Ambler, R. Hayward, D. Hopper and R. Hudson, Phys. Rev. **105**, 1413 (1957)

[8] E. Majorana, Nuovo Cimento **14**, 171 (1937)

[9] T. Yanagida, Proc. Workshop on Unified Theory and Baryon Number in the Universe, eds. Sawada and Sugamoto, KEK (1979)
M. Gell-Mann, P. Ramond and R. Slansky, Supergravity, ed. van Niewenhuizen and Freedman (North-Holland, Amsterdam, 1979)

[10] T. Kirsten et al., Proceedings of the International Symposium on Nuclear Beta Decay and Neutrinos, Osaka, Japan 1986, ed. T. Kotani et al. (World Scientific, Singapore, 1986) p. 81

[11] O. K. Manuel, Proceedings of the International Symposium on Nuclear Beta Decay and Neutrinos, Osaka, Japan 1986, ed. T. Kotani et al. (World Scientific, Singapore, 1986) p. 71

[12] S. Elliot, A. Hahn, and M. Moe, Phys. Rev. C **36**, 2129 (1988)

[13] D. Caldwell, Proceedings of the XXIII International Conference on High Energy Physics, Berkeley, Ca., 1986, ed. S. Loken (World Scientific, Singapore, 1987) Vol.2, p. 951

[14] S. Elliot, A. Hahn, and M. Moe, Phys. Rev. Lett. **59**, 2020 (1987), and UCI preprint 88-11

[15] J. Krivicich, Ph.D. thesis, "A New Limit on the Neutrinoless Double Beta Decay of ^{100}Mo", Univ. Calif. Berkeley, 1988

M. Alston-Garnjost, B. Dougherty, R. Kenney, J. Krivicich, R. Tripp, A. Smith, J. Walton, H. Nicholson, B. Dieterle and C. Leavitt, Nucl. Inst. and Meth. in Physics Research A271, 475 (1988)

M. Alston-Garnjost, B. Dougherty, R. Kenney, J. Krivicich, R. Tripp, H. Nicholson, S. Sutton, B. Dieterle, J. Kang and C. Leavit, Phys. Rev. Lett. 60, 1928 (1988)

[16] W. Haxton and G. Stephensen, Jr., Prog. in Part. and Nucl. Phys. **12**, 409 (1984)

[17] M. Doi, T. Kotani and E. Takasugi, Prog. Theor. Phys. Supp., **83**, (1985)

[18] W. Haxton, G. Stephenson, Jr. and D. Strottman, Phys. Rev. Lett. **47**,153 (1981), Phys. Rev. D **25**, 2360 (1981)

M. Doi, T. Kotani, H. Nishiura and E. Takasugi, Prog. Theor. Phys. **69**, 602 (1983),

M. Doi, T. Kotani and E. Takasugi, Osaka preprint OS-GE 84-09

J. Sinatkas, L. Skouras and J. Vergados, Phys. Rev. C **37**, 1229 (1988)

[19] K. Grotz, H. Klapdor, Nucl. Phys. **A460**, 395 (1986)

K. Muto and H. Klapdor, Phys. Lett. B **201**,420 (1988)

T. Tomoda et.al., Nucl. Phys. **A452**, 591 (1986)

J. Civitarese, A. Faessler and T. Tomoda, Phys. Lett. B **194**, 11 (1987)

T. Tomoda and A. Faessler, Phys. Lett. B **199**, 475 (1987)

P. Vogel and M. Zirnbauer, Phys. Rev. Lett. **57**, 3148 (1986)

J.

[20] G. Stephenson Jr., private communication

[21] W. Haxton and G. Stephenson, Jr., Prog. in Part. and Nucl. Phys. **12**, 409 (1984) section IV.C.

[22] C. Ching and T. Ho, Inst. of Theoretical Physics preprint, Academia Sinica (Beijing) ITP-88-019

[23] B. Kayser Phys. Rev. D **30**, 1023 (1984)

[24] Y. Chikashige, R. Mohapatra and R. Peccei, Phys. Lett. **98B**, 265 (1981)
G. Gelmini and M. Roncadelli, Phys. Lett. **99B**, 411 (1981)
H. Georgi, S. Glashow and S. Nussinow, Nucl. Phys. B **193**, 297 (1981)

[25] B. Kayser, Proceedings of the XXIII International Conference on High Energy Physics, Berkeley, Ca. 1986, ed. S. Loken (World Scientific, Singapore, 1987)

[26] J. Shechter and J. Valle, Phys. Rev. **D25**, 2951 (1982)
L. Wolfenstein, Phys. Rev. **D26**, 2507 (1982)
C. Escobar and V. Pleitez, Phys. Rev. D **28**, 1166 (1983)

[27] J. Vergados, Phys. Lett. **184**, 55 (1987)

[28] R. Winter, Phys. Rev. **83**, 1070 (1951)
B. Pontecorvo, Phys. Lett. B **26**, 630 (1968)

[29] J. Engel, P. Vogel and M. Zirnbauer, Phys. Rev. C **27**, 731 (1988)

[30] T. Tomoda and A. Faessler, Phys. Lett. B **199**, 475 (1987)

[31] V. Lubimov, S. Boris, A. Golutvin, L. Lapin, V. Nagovitsyn, E. Novikov, V. Nozik, V. Solostchenko, I. Tikhomirov and E. Tretyakov, Proc. of the Int. Europhys. Conf. on HEP, Brighton, July 1983, p. 386, eds. J. Guy and C. Costain (Rutherford-Appleton Lab., Chilton, Didcot, UK 1984)

[32] D. Stoker, B. Balke, J. Carr, G. Gidal, A. Jodidio, K. Shinsky, H. Steiner, M. Strovink, R. Tripp, B. Gobbi and C. Oram, Phys. Rev. Lett. **54**, 1887 (1985)

[33] A. Klimenko, A. Pomanski and A. Smolnikow, Nuc. Inst. and Meth. **B17**, 445 (1986)

[34] see the reviews in the procedings of the XXIV Int. Conf. on HEP, Munich, Aug. 1988; It might be noted that a Soviet experiment using enriched ^{76}Ge (Yerevan) has obtained a Majoron-induced double beta decay half-life limit of 4.5×10^{21} years at 68% confidence.

[35] Yu. Zdesenko et. al., Proceedings of the International Conference Neutrino'82, Balatonfüred, Hungary, 1982, ed. A. Frenkel et al. (Budapest, 1982) p. 209

[36] E. Belloti, E. Fiorini, C. Ligouri, A. Pullia, A. Sarracino and L. Zanotti, AIP Conf. Proc. 99 (TELEMARK '82), ed. V. Barger and D. Cline (New York, 1983)

[37] H. Ejiri, N. Kamikubota, Y. Nagai, T. Okada, T. Shibata, T. Shima, N. Takahashi, J. Tanaka, T. Taniguchi and T. Watanabe, Proc. TELEMARK IV, ed. V. Barger et al., World Scientific (1987) p. 281

[38] M. Crouch, Proc. 19th Int. Cosmic Ray Conf., La Jolla, CA (1985) NASA Conf. Pub. 2376

[39] National Wax Co. (Skokie, Ill.), Borated-polyethylene (Reactor Experiments, Inc. San Carlos, California), lead (St. Joseph Mine, Missouri), nitrogen (A.L. Welding Co., Spokane, Washington)

[40] obtained from Micron Semiconductor, Ltd. of Longwood, Fla.

[41] Program Library, CERN DD Division, CH-1211 Geneva 23, Switzerland

[42] Int. Comm. on Rad. Units and Meas., Report #37 (1984)

[43] Kolbig and Schorr, Comp. Phys. Comm. **31**, 97 (1984)

[44] L. Landau, Journal of Physics **8**, 201 (1944)

[45] T. Tabata, R. Ito and S. Okabe, Nucl. Instr. and Meth. **103**, 85 (1972)

[46] T. Tabata, R. Ito and S. Okabe, Nucl. Instr. and Meth. **94**, 509 (1971)

[47] V. Kuzminikh and S. Vorobiev, Nucl. Instr. and Met. **129**, 561 (1975)

[48] J. Hubbell, Nat. Stand. Ref. Data Ser., NBS **29**

[49] Table of Isotopes, 7^{th} Edition, ed. C. Lederer and V. Shirley, (J. Wiley & Sons, Inc., 1978)

[50] Helium Stopping Powers and Ranges in All Elemental Matter, J. Ziegler (Pergamon Press, 1977)
see also L. Northcliffe and R. Schilling, Nuclear Data Tables **A7**, 223 (1970)